

Evaluation of Seismicity Trends in Kansas to Determine Possible
Source Mechanisms Using Focal Mechanism Inversion
and Spectral Analysis

By
© 2019

John Intfen
B.Sc., University of Kansas, 2011

Submitted to the graduate degree program in Geology and the Graduate Faculty of the
University of Kansas in partial fulfillment of the requirements
for the degree of Master of Science.

Chair: Dr. Richard D. Miller

Dr. J. Douglas Walker

Dr. Chi Zhang

Date Defended: Thursday, August 1st, 2019

The thesis committee for John Intfen
certifies that this is the approved version of the following thesis:

**Evaluation of Seismicity Trends in Kansas to Determine Possible
Source Mechanisms Using Focal Mechanism Inversion
and Spectral Analysis**

Chair: Dr. Richard D. Miller

Date Approved: Thursday, August 15, 2019

Abstract

High b-value, proper stress orientation and low stress drop are three factors that support the suggestion that a majority of events in central Kansas are induced as a result of changes in pore pressure. Furthermore, stress orientation and seismic trends align with regional lineations interpreted from magnetic data. These linear trends are likely influencing seismicity in the northern part of the state and the feature that supports the suggestion that injection of wastewater in an area 90km away is influencing seismicity in Smith, Jewell and Republic counties in Kansas.

Kansas seismicity started in 2014 and rapidly increased in frequency, culminating in the largest recorded earthquake in state history on November 12th, 2014. This size event led to a drastic increase in interest and therefore the number of seismic stations distributed in areas previously determined aseismic. This resulted in the discovery of new earthquake clusters located outside historically active seismic areas. The Kansas Geological Survey (KGS) deployed a temporary and permanent station array to significantly improve coverage offered by a temporary network installed by the United States Geological Survey in 2013. This enhanced KGS network along with other stations installed across the state revealed new clusters in Jewell and Saline County, areas that were considered seismically quiescent.

The focus of this research is to explore the characteristics of seismic activity clustering in locations outside the high profile area in south-central Kansas with the most proliferate seismic activity (Harper and Sumner Counties). These focus areas include Reno, Salina, and Jewell Counties where new clusters of seismic activity have developed since 2016. These three areas are host to notable clusters and were chosen base on unique and historically inconsistent seismic activity.

For each of the three study areas (Jewell, Saline, and Reno) four focal mechanism algorithms determined the focal sphere orientation of 95 events using 34 different stations and the maximum horizontal stress for each area was calculated using a Michael 1984 inversion. Stress orientations in

Reno County are consistent with those calculated in Oklahoma but rotates almost 90° further north in Jewell County. Brune stress drop was calculated for 90 events in each of the three study areas to compare with stress drops calculated in the south portion of the state (Harper and Sumner counties) and across the Central United States. Low stress drops throughout the state are consistent with the range of stress drops found for induced events in Oklahoma (Hough, 2014; Sumy et al., 2014) and other parts of the Central United States (Boyd et al., 2017).

Acknowledgements

I would like to thank my advisor, Rick Miller, for introducing me to this project and his in-depth expertise and guidance supporting this work. I was fortunate enough to have some incredible field experiences in Nebraska, Alabama and Hutchinson, KS that expanded my geophysical understanding beyond earthquake seismology. I would also like to thank the rest of my committee, Doug Walker and Chi Zhang, for taking time out of their busy schedules to read, discuss and critique my work throughout the process.

A number of professors had a hand in shaping my geologic career; none more than George Tsoflias, Ross Black, Diane Kamola and Tony Walton. Their teaching, mentoring and expertise throughout my graduate school career was unmatched. A special thanks to Shelby Peterie who provided continual guidance and support throughout my career. Julia Gonzales helped with everything related to SeisAn and data formatting. Additionally, I would like to thank the students and staff at the Kansas Geological Survey for their support: Alex Nolte, Brett Bennett, Brett Wedel, Carl Gonzales, Joe Anderson, Julian Ivanov, Kurt Look, Mary Brohammer and Sarah Morton.

Lastly, I would like to thank my friends and family that supported me throughout my entire academic career and for always giving a different perspective on things.

Table of Contents

Abstract.....	iii
Acknowledgements.....	v
Table of Contents.....	vi
Figures.....	vii
Chapter 1 – Introduction.....	1
Chapter 2 – Geologic Setting	9
Chapter 3 – Kansas Station History and Installation.....	20
Section 3.1 - Seismic Station History.....	20
Section 3.2 - Station Configuration	21
Section 3.3 – Historical Seismicity in Kansas.....	22
Chapter 4 – Cataloging Earthquakes in Kansas (2015-2018)	32
Section 4.1 - Identifying and locating Earthquakes from Seismic Data	32
Section 4.2 - Earthquake Magnitudes.....	34
Section 4.3 – Magnitude vs. Frequency.....	36
Section 4.4 - Earthquake Catalog and Database.....	37
Section 4.5 - Earthscope Transportable Array (TA) Data	38
Chapter 5 – Focal Mechanisms and Inversion	48
Chapter 6 – Stress Drop	53
Chapter 7 – Results and Conclusion.....	57
Section 7.1 – Results	57
Section 7.2 - Discussion.....	58
Section 7.3 - Conclusion.....	63
References	76
Appendix A: Catalog of Earthquakes - Earthscope Transportable Array Data.....	82
Appendix B: Catalog of Earthquakes – Focal Mechanisms Data.....	83
Appendix C: Catalog of Earthquakes – Stress Drop Data.....	86
Appendix D: Earthquake S-files.....	89

Figures

Figure 1-1 - Map of historical earthquakes in Kansas from 1867 to 2018 (www.kgs.ku.edu). Areas of interest outlined in red; from north to south – Jewell County Area, Saline County, Reno County (City of Hutchinson) and the City of Milan, near the M_w 4.9 earthquake in 2014.	5
Figure 1-2 - Diagram from Ellsworth, 2013 depicting the two most likely mechanisms of inducing earthquakes. The first (left side), is from increased pore pressures, and the second (right side), is from changes in the shear and normal stresses from loading acting on a fault.	6
Figure 1-3 - (a) Count of operational seismometer stations in Kansas per quarter. (b) Quarterly earthquake rates for the state of Kansas with overlain cumulative number of >M2 earthquakes. Gray shading outlines Kansas-Nebraska network. Green shading outlines the EarthScope Transportable Array network (TA). Orange shading outlines more recent networks operational (KM, ZA, GS, US, etc.). White space denotes relative state network hiatus (no monitoring).	7
Figure 1-4 - Map showing the 2018 chance of minor damaging earthquakes in the United States (Modified from Peterson et al., 2018).	8
Figure 2-1 - Map of Kansas showing the relationship between the Central Kansas Uplift, the Salina Basin and the Nemaha Ridge (Merriam, 1963). Up to the creation of this map there were 24 earthquakes located in Kansas from 1867. These earthquakes were given their respective Mercalli magnitudes.	12
Figure 2-2 – Map of Kansas showing all Underground Injection Control (UIC) Class I and Class II wells from 2000-2017 (KGS, 2018). Areas of interest vary in proximity to high injection areas.	13
Figure 2-3 - Residual Bouguer gravity anomaly map (Top) from Xia et al., 1995a and Aeromagnetic map (Bottom) from Xia et al., 1995b. Blues represent low residual Bouguer gravity values and magnetic values. The bright pink spot is the strongest expression of this anomaly in the state. Reds represent high residual Bouguer gravity values and magnetic values. Maps modified to include areas of interest in this study (red lines).	14
Figure 2-4 - Magnetic lineations derived from magnetic data in figure 2.3. Area of study for this paper are outlined in red. (Modified from Yarger, 1983).	15
Figure 2-5 - Map of basement faults in Kansas. Counties outline in red from North to South are Smith/Jewell/Republic, Saline, Reno, and Sumner (Modified from Baars, 1995).	16
Figure 2-6 - Arbuckle Group isopach map from well data up to 1965 (Cole, 1975).	17
Figure 2-7 - Map of maximum horizontal compressive stress orientations, modified from Zoback and Zoback, 1989. Alt and Zoback, 2017 would provide one more data point within Kansas, but the stress state is unknown for a large portion of the state.	18
Figure 2-2-8 – Map of stress orientations calculated from both wellbore data and focal mechanism inversion. Red Box outlines Sumner County, an area of interest in this study. (Modified from Alt and Zoback, 2017).	19
Figure 3-1 - (a) Count of operational seismometer stations in Kansas per quarter. (b) Station installation timeline, horizontal blocks represent a stations active period. Color groupings represent network, as indicated. Certain Transportable Array stations were converted into permanent stations making up a new network – Central and Eastern US Network (CEUSN), network code N4. One station in Kansas was converted (R32A, now R32B). Operational efficiency of various stations installed after 2014 and not part of the KGS network may be poor. These data points do not reflect station downtime, only commission to decommission time periods.	24

Figure 3-2 - Map showing the locations of seismometers that operated in Kansas from 1977 to 2013 – Kansas-Nebraska Network (KSNE – not in IRIS) operated from 1977 to 1989, Rocky Mountain Front II (XG) operated in 1992, and the EarthScope Transportable Array (TA) had varying station coverage from 2009 to early 2012.	25
Figure 3-3 - Map showing the locations of seismometer that operated in Kansas from 2014 to present day – Kansas Geological Survey Primary and Temporary networks (KM) deployed in 2014, US Geological Survey networks (GS/US) deployed in early 2014, and the Wellington CO2 Sequestration Monitoring Project (ZA) deployed in mid-2014. The single Transportable Array Station converted to a permanent station can be seen in the middle of the state, this station is now actively apart of the Central and Eastern US Network (CEUSN), network code N4. All networks are still operating in Kansas to some extent. Red Boxes outline counties of interest.....	26
Figure 3-4 – Typical earthquake seismic station (top right), inverted bucket housing seismometer (bottom right) and equipment box attached to the solar panel pole (left).....	27
Figure 3-5- KGS Station schematic depicting all the components needed for a seismic station. (Credit: Mary Brohammer, KGS)	28
Figure 3-6 - Felt earthquakes located in Kansas from 1867 to 1961 (Dubois and Wilson, 1978).....	29
Figure 3-7 - Historical seismicity in Kansas from 1977 to 1989 (Steeple et al., 1990).	30
Figure 3-8 - USGS located earthquakes in Kansas between 1990 and 2013 (NEIC, 2019).	31
Figure 4-1- Example of pump jack noise from a KGS Regional Station. In an effort to place regional network stations in areas with the best signal to noise ratio for optimal monitoring, this station was moved further away from the noise source. The cyclicity of a pump jack degrade the signal continuously and interferes with both the automated and manual process of detecting earthquakes.	41
Figure 4-2– A) Vertical component seismograms from an earthquake (top) and quarry blast (bottom) taken from Frohlich, 2012. The prominent surface wave of the quarry blast is easily identifiable within raw seismic data. B) Example of quarry blast observed in Barber County, Kansas.	42
Figure 4-3 - Example of raw seismic data taken from 10 stations across the state. The event shown is the largest magnitude seismic event recorded from Jewell County to date. The 3.9Mw earthquake occurred on June 13th, 2017 at 4:40AM. On the left are the Station, Component, Network, and Location (SCNL) of each sensor used in the analysis. P-Wave arrivals are denoted by ‘IP’, and S-Wave arrival is marked with an ‘IS’. The end of the backscattered wave, the coda, is marked by ‘coda’	43
Figure 4-4 - Plot of earthquake frequency versus magnitude. Earthquakes were grouped every 1/10th of a magnitude. Gutenberg-Richter Relationship (Green) is used to describe the recursion of higher magnitude events and assess the completeness of the catalog used.....	44
Figure 4-5 - Instrument response correction generates simulated Wood-Anderson seismographs which is used in determining Magnitudes.....	45
Figure 4-6 - Instrument response correction generates simulated Wood-Anderson seismographs which is used in determining Magnitudes.....	46
Figure 4-7 - Map of earthquakes in Kansas detected from the Earthscope Transportable Array data between May 2009 and March 2010. The nine stations shown are a sub-network of a larger array. Earthquakes located using this data can be found in Appendix A.....	47
Figure 5-1 - Focal Sphere depicting the three focal mechanism solutions for the June 12th M3.9 earthquake in Jewell County. First motion plots can be seen on the left and right sides with red	

arrows indicated picked compression (up) and tension (down). On the focal sphere blue circles represent compression (P) and red triangles represent tension (T) used in 3 fault plane solution software packages used. Note that a discrepancy between the picked first motion and the calculated first motions are due to some algorithms allowing for first motion and amplitude errors. Red vertical line represents the picked P-Wave arrival for that station..... 51

Figure 5-2 - Idealized beachball diagrams showing mapview and side view of basic fault mechanisms. (Stein and Wysession, 2003). 52

Figure 6-1 – Log frequency vs. log seismic moment graph of an Idealized source spectra characterized by the flat portion for frequencies smaller than the f_c . The amplitude for each flat portion ($f < f_c$) increases with seismic moment M_0 while the f_c decreases proportional to M_0^{-3} . (Modified from Stein and Wysession, 2003) 55

Figure 6-2 – Sample waveform used to determine source parameters (top) and an example of seismic source spectra (Bottom) of ground displacement (green) overlain by the calculated Brune Displacement Spectra (Blue). 56

Figure 7-1 - Beachball diagram of all earthquakes in Smith, Jewell and Republic counties. 18 events had adequate misfit, station coverage, signal-to-noise and location to invert for stress orientation. Grey dots are the epicenters of earthquakes not used in the focal mechanism analysis. Inset map of Kansas shows stations from across the state. Diagram below the inset map illustrates preferred strike-slip and normal fault planes for a maximum horizontal stress of -48.7° 65

Figure 7-2 - Beachball diagram of all earthquakes in Saline County that were used to determine the stress field. 24 events had adequate station coverage, signal to noise and location. Thick grey lines are magnetic lineations interpreted from Aeromag data; Yarger, 1983. Inset map shows the full magnetic lineation interpretation from Yarger, 1983 and includes an outline of MGA..... 66

Figure 7-3 - Beachball diagram of all earthquakes in Reno County that were used to determine the stress field; 21 events in total. Grey dots are the epicenters of earthquakes not used in the focal mechanism analysis. Inset map of Kansas shows stations from across the state providing excellent azimuthal coverage. Diagram to the right of the inset map illustrates preferred strike-slip and normal fault planes for a maximum horizontal stress of 47.1° 67

Figure 7-4 – Rose diagram depicting the orientation of the P-axis orientations (Right) and the T-axis orientations (Left) for each of the 3 areas. Michael, 1984 focal mechanisms inversion method was used in conjunction with SeisAn. 68

Figure 7-5 - Moment Magnitude vs. Corner Frequency plot of study areas with Brune constant stress drop lines indicated. A more detailed stress analysis of the Milan earthquake sequence can be found in Choy et al., 2016 where similar stress drops were calculated. 70

Figure 7-6 - Log_{10} of stress drop in Jewell County overlain by focal mechanisms calculated in Chapter 8. Size (magnitude) of stress points are M_w and size of beachballs are M_l . Thick grey lines are magnetic lineations interpreted from Aeromag data; Yarger, 1983. Diagram below the inset map illustrates preferred strike-slip and normal fault planes for a maximum horizontal stress of -48.7° . Inset map shows all magnetic lineations interpreted from magnetic data from Yarger, 1983. Green polygon outlines the Central Kansas Uplift, a popular area for wastewater disposal..... 71

Figure 7-7 - Map of Saline County Log_{10} stress drops with surrounding injection wells sized to annual injection volume. Inset map shows all UIA Class I and II injection wells in Kansas between 2000 and 2017. 72

Figure 7-8 - Map of Reno County Log₁₀ stress drops with surrounding injection wells sized to annual injection volume. Inset map shows all UIA Class I and II injection wells in Kansas between 2000 and 2017. 73

Figure 7-9 - Map of Milan area Log₁₀ stress drops with surrounding injection wells sized to annual injection volume. Inset map shows all UIA Class I and II injection wells in Kansas between 2000 and 2017. Stress drop results align well with previous studies from Choy et al., 2016. 74

Figure 7-10 - Regional map of Kansas showing all four areas with stress drop in relation to local injection wells. 75

Chapter 1 – Introduction

Since the late 2000's, seismicity has become a growing concern for politicians, regulators, companies, farmers and families across the Central United States (Ellsworth, 2013). The rise in anthropogenic/induced seismicity has been observed in Ohio (Kim, 2013), Texas (Frohlich, 2012), Oklahoma (Keranen et al., 2013 and 2014), Colorado (Rubenstein, 2014) and Arkansas (Horton, 2012). In 2014, the dozen available stations in Kansas began detecting an increase in seismic activity in several areas, with the most significant increases in the two-county area in south-central Kansas (Harper and Sumner) (Figure 1.1). These two adjacent counties are located on the Kansas-Oklahoma border.

Of the thousands of waste water disposals wells in the United States, only a few can be linked to local anthropogenic seismicity (Frohlich, 2012). The two most commonly referenced cases were at Rocky Mountain Arsenal, Colorado in the 1960's (Evans, 1966; Healey et al., 1968) and Paradox Valley, Colorado, in the 1990's (Ake et al., 2005). In both of these cases, fluid injected into the subsurface was interpreted to trigger seismic activity.

Elevated levels of fluid injection and seismicity have been generating considerable research interest over the last half dozen years. Two mechanisms are thought to explain how injection can induce seismicity. The first is that injection volumes above critically stressed faults change the shear and normal stresses on a fault, bringing it to the point of failure (Ellsworth, 2013) (Figure 1.2). Other studies have shown that locally elevated pore pressures from nearby wastewater disposal wells reduce the effective stress resulting in critical failure along optimally oriented and critically stressed basement faults (Raleigh et al., 1976; Hubbert and Rubey, 1959; Nicholson and Wesson, 1990). In Kansas, the most active injection interval is the Cambrian-Ordovician Arbuckle Group. With excellent porosity, permeability, depth of burial and thickness, from 350 feet thick in the north to almost 1200 feet in the

thick in the south, the Arbuckle is extensively used for waste water disposal. In many places faults hydraulically connect the Arbuckle with seismically active crystalline basement.

Historically, Kansas has experienced a magnitude (M) 3 or larger earthquake every one to two years with a total of 96 +M2 between 1977 and 2013 (National Earthquake Information Center (NEIC), 2019; Steeples et al., 1987, 1990). Starting in 2013 the rate at which Kansas experienced a +M2 earthquake began drastically increasing. Through 2018, over 3600 +M2 earthquakes have been recorded (Figure 1.3). Over 80% of these earthquakes were located in the southern portion of the state and have been well studied (Ellsworth, 2013, Keranen et al., 2014, Walsh and Zoback, 2015, Langenbruch and Zoback, 2016; Rubenstein, 2018; Choy et al., 2016).

The Central Kansas Uplift has been seismically active since the first statewide network was installed in 1977. Other parts of the state have been seismically quiet for the majority of the state's recording history. The ground shaking hazards map published by the United States Geological Survey (USGS) in 2018 shows a majority of the state having a <1% chance of minor-damage (Figure 1.4). The USGS did not have access to the greatly enhanced monitoring network in Kansas and did not locate earthquakes in the central and northern part of the state that began in 2016. The USGS reported only one earthquake in Jewell County (NEIC, 2019) leading up to the emergence of this unique cluster.

Kansas has had minimal station coverage from 1989 to around 2013 with the recent uptick in seismicity. The underutilized EarthScope Transportable Array (TA) project (Figure 1.3) was a temporary, portable station array that operated in Kansas as part of the national program for a period of 24 months per station. The data from this project has seen little utility in cataloging and studying seismicity in Kansas. The timing of this array provides greatly increased network coverage for this study in the time period immediately preceding drastic increases in wastewater disposal in 2013.

Discriminating naturally occurring events from induced events has vast economic, political and scientific implications. In Kansas, it has proven difficult to characterize properties that discriminate natural from induced events because of an erratic monitoring history with predominately light monitoring experience, short lived with a transitory monitoring effort in the early 2000's and is currently being monitored with a dense array in the south.

The wave of new research in seismicity in Kansas is principally exploring various mechanisms potentially responsible for this surge in seismicity. These research focus areas include pore pressure diffusion and far field effects (Peterie et al., 2018), shear wave anisotropy (Nolte, 2017) and Arbuckle structure mapping (Schwab et al., 2017).

Although the goal of this study is to discriminate which earthquakes within the selected areas of study are natural from those that are induced, a rigorous investigation into the geological structures, stress field and pressure regimes require more seismic stations near these previously quiescent areas. As data quality increases in both sensitivity and abundance, other analysis may be appropriate for active areas in Kansas. No single test can be used to determine the mechanism of an earthquake; presented in this paper are a few indicators that can be interpreted to suggest nearly all the earthquakes occurring in the state today are related to injection.

Following the emplacement of the initial networks by the KGS and USGS, three areas of increased seismicity have developed that may provide a unique look into changes in geologic and physical properties (Figure 1.1). These three areas vary in location uncertainty, station coverage, proximity to high injection areas and an understanding of the regional stress field.

The northern most area includes three adjacent counties along the Kansas-Nebraska border: Smith, Jewell, and Republic. We will refer to these three counties as the Jewell County Area since Jewell County has a majority of the located seismic events. Saline County is 100km to the southeast of Jewel

County; since January of 2016, 68 seismic events have been located in this area. The third area of interest is approximately 2 miles by 3 miles section of Reno County that has included over 100 seismic events that have been located from 2016 to 2018.

Within these three areas of dense earthquake epicenters, focal mechanism inversion should extend our understanding of the stress field similar to advancements in previous studies (Alt and Zoback, 2017). Mapping optimally oriented faults in relation to the maximum horizontal stress determines the risk of damaging earthquakes. In addition to this stress drop for each event may be an additional discriminating factor. Low stress drop has been suggested as a discriminating factor in induced seismicity (Boyd et al., 2017). In addition to the above three areas, we will look at the area and events relating to the largest earthquake in Kansas history, the M_w 4.9 earthquake near the City of Milan, Kansas on November 12, 2014. Since this event predates the KGS catalog, we will benchmark the stress drop results against those of Choy et al., 2016.

From a catalog of over 12,000 seismic events from across the state, b-value since 2014 was calculated to be higher than historical and regional values. Stress drop calculations within the areas of interest are an order of magnitude lower than regional stress drops. The low median stress drop of each area may be an indication that many of these seismic events are injection related. In addition to the stress drop calculations the focal mechanisms were calculated for events with adequate station coverage. Inversion of these focal mechanisms indicate the regional stress field rotating from the southern portion of the state to the northern portion of the state. The rotated stress field would suggest that faults not previously thought to be optimally oriented to slip could in fact be optimally oriented.

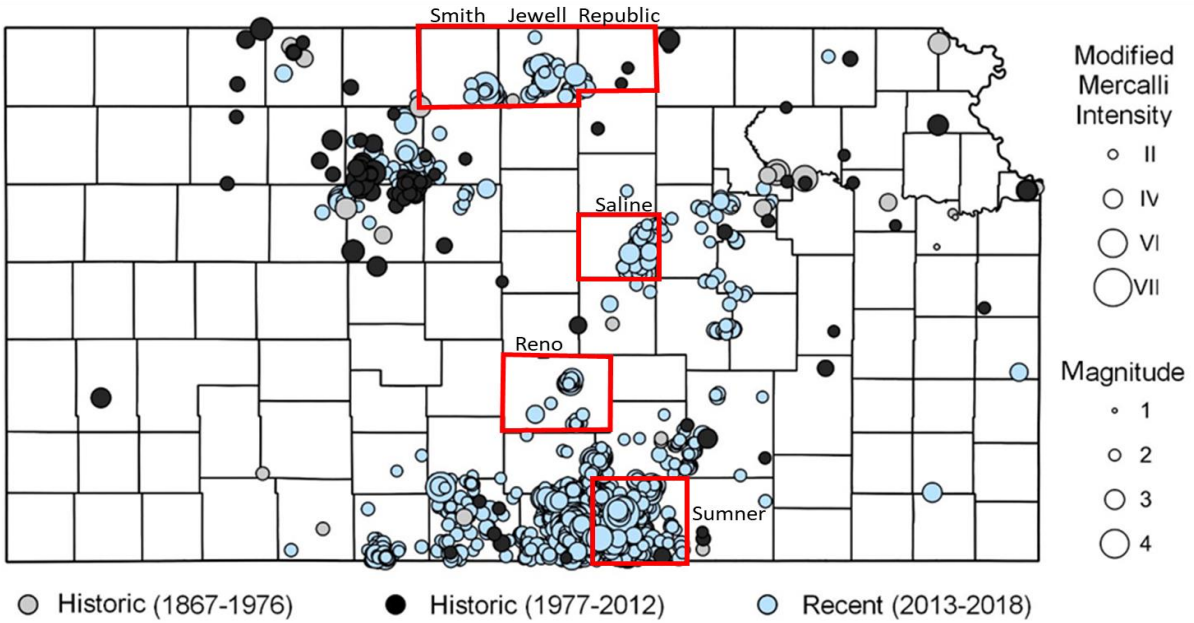


Figure 1-1 - Map of historical earthquakes in Kansas from 1867 to 2018 (www.kgs.ku.edu). Areas of interest outlined in red; from north to south – Jewell County Area, Saline County, Reno County (City of Hutchinson) and the City of Milan, near the M_w 4.9 earthquake in 2014.

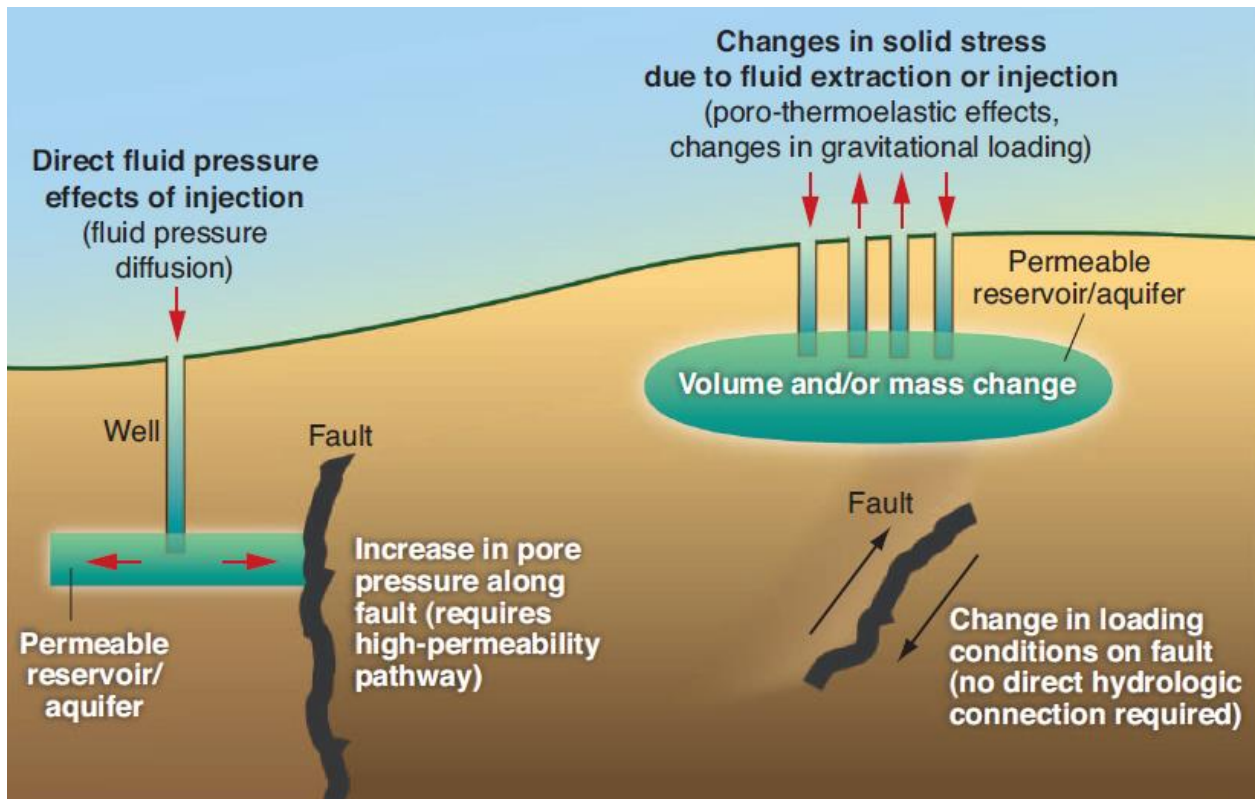


Figure 1-2 - Diagram from Ellsworth, 2013 depicting the two most likely mechanisms of inducing earthquakes. The first (left side), is from increased pore pressures, and the second (right side), is from changes in the shear and normal stresses from loading acting on a fault.

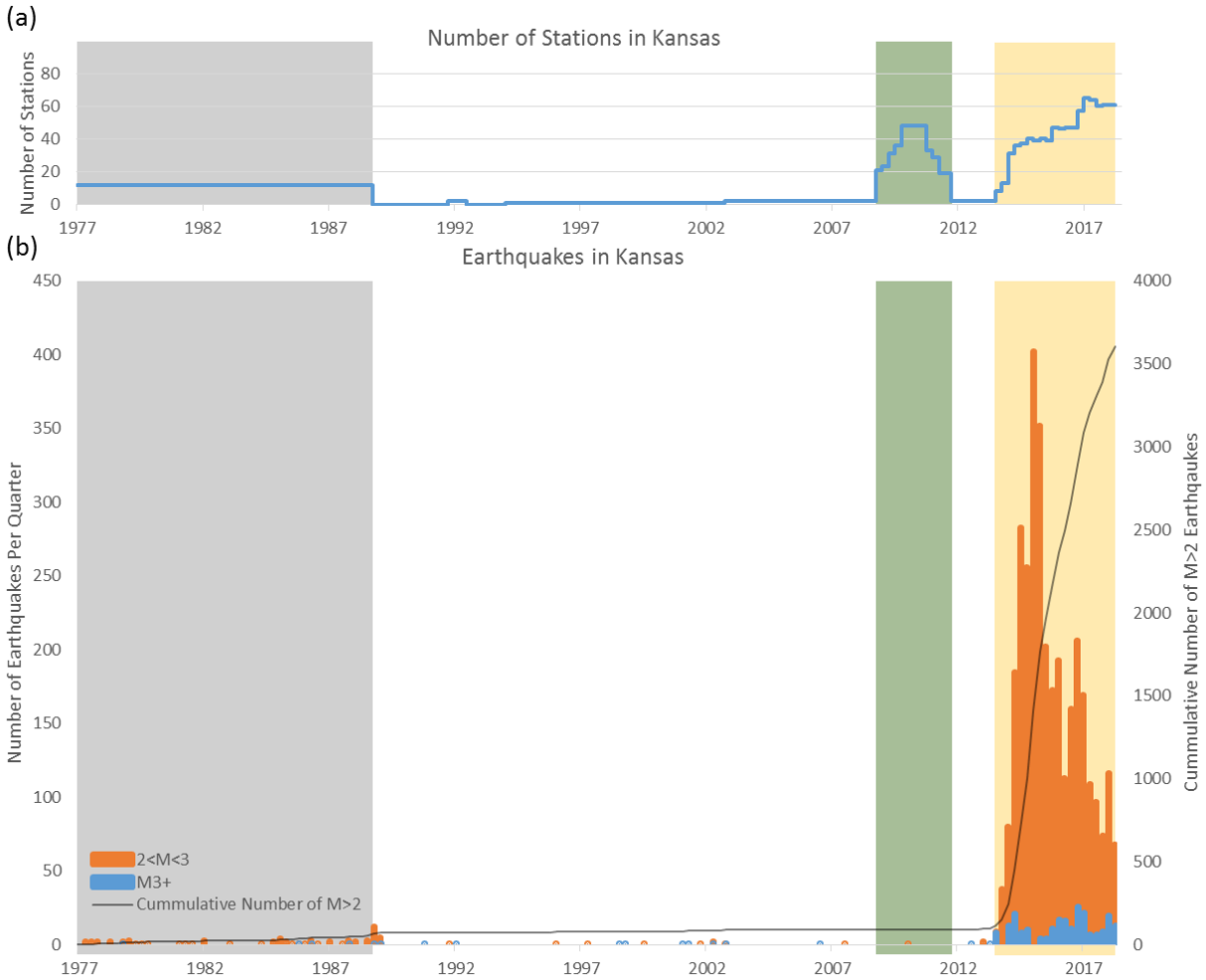
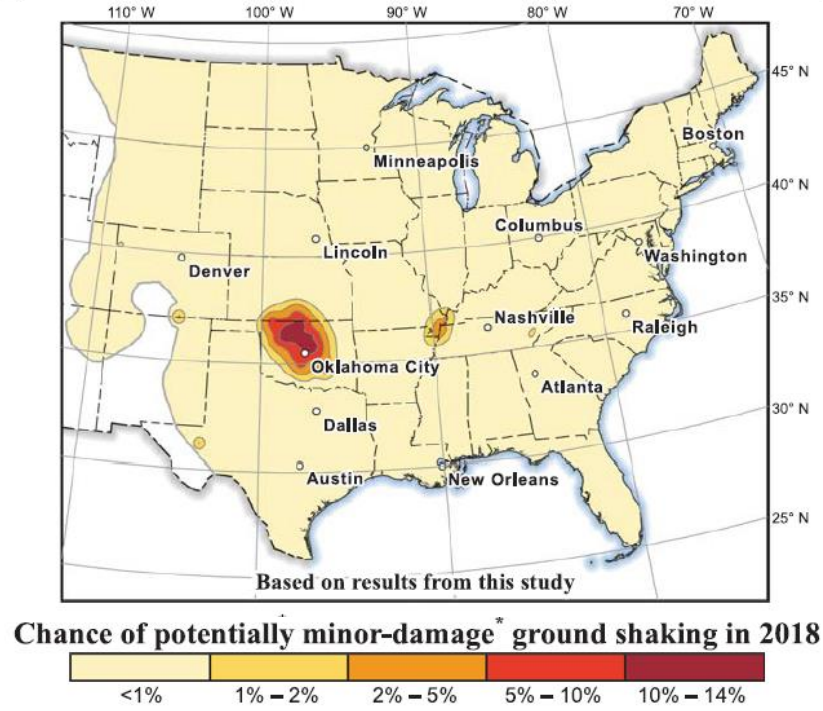


Figure 1-3 - (a) Count of operational seismometer stations in Kansas per quarter. (b) Quarterly earthquake rates for the state of Kansas with overlain cumulative number of >M2 earthquakes. Gray shading outlines Kansas-Nebraska network. Green shading outlines the EarthScope Transportable Array network (TA). Orange shading outlines more recent networks operational (KM, ZA, GS, US, etc.). White space denotes relative state network hiatus (no monitoring).

Based on the average of horizontal spectral response acceleration for 1.0-s period and peak ground acceleration



* equivalent to modified Mercalli intensity VI, which is defined as: "Felt by all, many frightened. Some heavy furniture moved; a few instances of fallen plaster. Damage slight."

Figure 1-4 - Map showing the 2018 chance of minor damaging earthquakes in the United States (Modified from Peterson et al., 2018).

Chapter 2 – Geologic Setting

Kansas is situated on a stable, platform-like extension of the Canadian Shield (Merriam, 1963). Within Kansas, there are four major geologic structures likely influencing the four areas with increased seismicity that are the subject of this study: 1) Salina Basin 2) Central Kansas Uplift 3) Midcontinent Geophysical Anomaly 4) Nemaha Ridge - Humboldt Fault Zone.

The Salina Basin underlies a large portion of north-central Kansas. The west most boundary of the basin is defined by the Cambridge Arch and Central Kansas Uplift and the east most boundary is the Nemaha Uplift (Figure 2.1). The Salina Basin extends to a southern saddle point between it and the Sedgwick Basin formed from the Chautauqua arch and the Barton arch (Barwick, 1928). At its thickest, the Mississippian limestone of the Salina Basin can be up to 350 feet thick but thins or is completely removed on the margins due to pre-Pennsylvanian erosion (Lee, 1956). There has been no oil or gas production nor any deep disposal in Smith, Jewell or Republic County since 2000 (Figure 2.2).

The western extent of the Salina Basin is defined by the Central Kansas Uplift, a Precambrian age northwest-trending arch developed from multiple periods of warping and erosion during the Paleozoic and Mesozoic time (Koester, 1935). A late Cambrian compressional event related to the midcontinent rift resulted in northwest trending normal faults that would later form the Ancestral Central Kansas Uplift (Gerhard, 2004). Reactivation of these faults in late Mississippian and Early Pennsylvanian due to the Auachita Orogeny reactivated uplift in portions of the Central Kansas Uplift (Ramaker, 2009). This structural feature is the largest in Kansas and underlies ~7,500 mi² of the state. At the crest of the uplift, Precambrian rocks are overlain by Pennsylvanian sediments, and on the flanks pre-Pennsylvanian strata are upturned, truncated, and overstepped by Pennsylvanian beds (Merriam, 1963).

The Midcontinent Geophysical Anomaly (MGA) is the largest gravity anomaly in North America (Figure 2.3) and extends from Lake Superior area southwestward into the midcontinent with no surface

topographic expression (Ocola and Meyer, 1973). More recent gravity and magnetic data shows that the MGA extends down into Oklahoma (Yarger, 1983). During late Precambrian rifting, basalts and gabbros developed forming a thick layer of mafic igneous rocks over most of the rifted section. These igneous rocks manifest as the bright pink gravity high (Figure 2.3); surrounding the gravity high is a large gravity low of the Rice Formation which is composed of arkosic sandstones to siltstones (Yarger, 1983). Striking similar to this geologic feature are various magnetic lineations. Several different spectral filters were used to eliminate unwanted characteristics of the original magnetic data. As a result of these filters various magnetic lineations were interpreted. From the aeromagnetic data in Yarger (1983) magnetic lineations are revealed in the northeast direction and the northwest direction (Figure 2.4). These drastic changes in magnetic susceptibility may be caused by offset due to faulting in the basement.

To the east and striking similar to the MGA lies the Nemaha Ridge (Figure 2.5). The Nemaha Ridge is a granitic uplift formed during a post-Mississippian uplift of granite. The ridge is bounded to the east by the Humboldt fault system and dominated by right-lateral, strike-slips crosscut by northwest, left-lateral shears (Jewett, 1951; Hildebrandt, 1988; McBee, 2003). The northwest trending extensional faults are pre-Phanerozoic and associated with midcontinent rifting (Gerhard, 2004). This structure extends from northeast Kansas down into central Oklahoma.

The Cambrian-Ordovician Arbuckle Group is mostly composed of a cherty dolomite and extends across much of the state. However, portions of the Group thin or are absent on parts of the Central Kansas Uplift and Nemaha Ridge (Merriam, 1963). The Arbuckle Group is approximately 400 ft thick in the northern most area of Jewell County (Figure 2.6) and thickens, southward to almost 1200 ft thick in the Sumner County area (Merriam, 1963; Franseen et al., 2004). The thickness of the Arbuckle Group was primarily determined from well data and interpolated across the state. Due to weathering and erosion, the upper most section of the Arbuckle has increased porosity and permeability making it a good candidate for waste water disposal. The weathering and erosion are limited to the upper portion

(30-50 feet) of the Arbuckle Group and the continuity and intensity of weathering is relatively unstudied but is present in various parts of the state (Steinhauff et al., 1998). The Arbuckle Group is thought to have slightly sub-hydrostatic pore pressures associated with adjacent under-pressure crystalline basement (Nelson et al., 2015).

Various studies have shown portions of the Arbuckle Group are hydraulically connected to the crystalline basement with multiple faults extending from the basement into the Arbuckle in Sumner, Kansas (Schwab et al., 2017). Induced seismicity in crystalline basement has been linked to injection in the Arbuckle in Oklahoma (Keranen et al., 2014). The crystalline basement is composed primarily of igneous and metamorphic rock (Merriam, 1963).

Kansas is situated in the middle of a relatively stable midplate region (Merriam, 1963). It is unlikely that any shear forces associated with remote faults outside the midcontinent would influence the stress field in the central United States (Zoback and Zoback, 1989), Figure 2.7. Although Kansas has been relatively quiet seismically, a small number of faults related to the four major structures are optimally oriented to slip under the existing in situ stress state thereby accounting for the natural seismicity rates in the state. The stress state within Kansas is not well understood, the most recent study finds the maximum horizontal stress orientation within Harper and Sumner Counties to be $71 \pm 6^\circ$ (Alt and Zoback, 2017). Alt and Zoback (2017) utilize both focal mechanism inversion and wellbore data to determine the stress orientation in north-central Oklahoma (Figure 2.8).

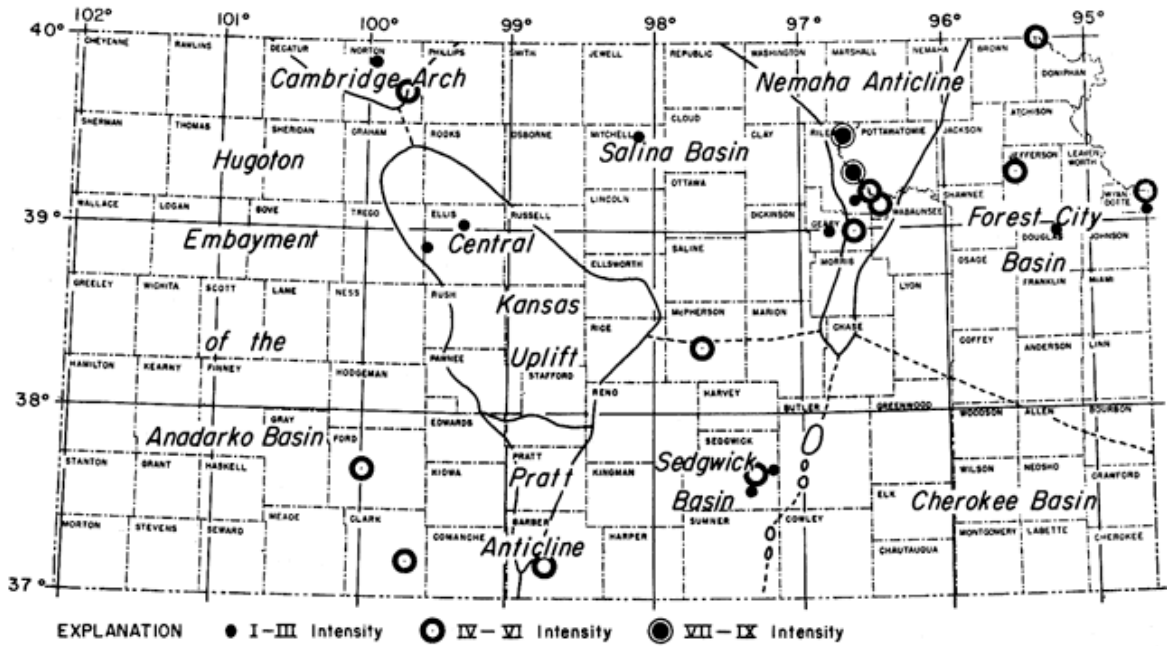


Figure 2-1 - Map of Kansas showing the relationship between the Central Kansas Uplift, the Salina Basin and the Nemaha Ridge (Merriam, 1963). Up to the creation of this map there were 24 earthquakes located in Kansas from 1867. These earthquakes were given their respective Mercalli magnitudes.

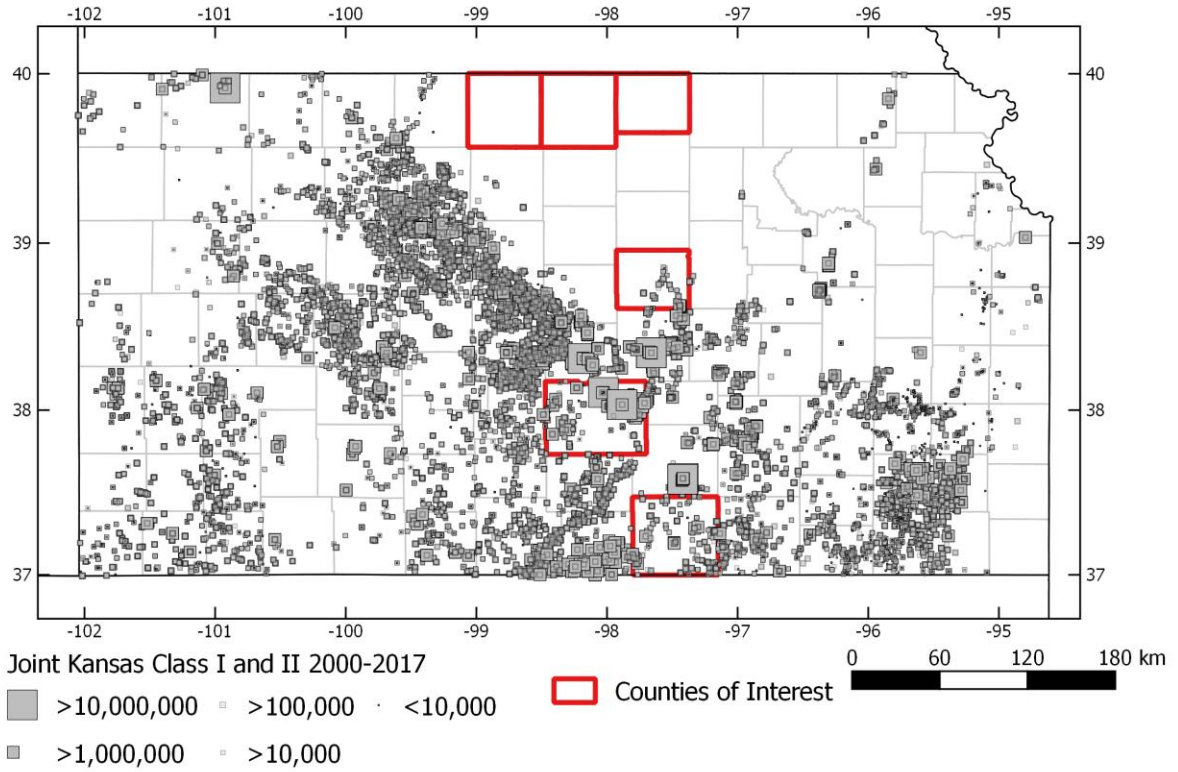


Figure 2-2 – Map of Kansas showing all Underground Injection Control (UIC) Class I and Class II wells from 2000-2017 (KGS, 2018). Areas of interest vary in proximity to high injection areas.

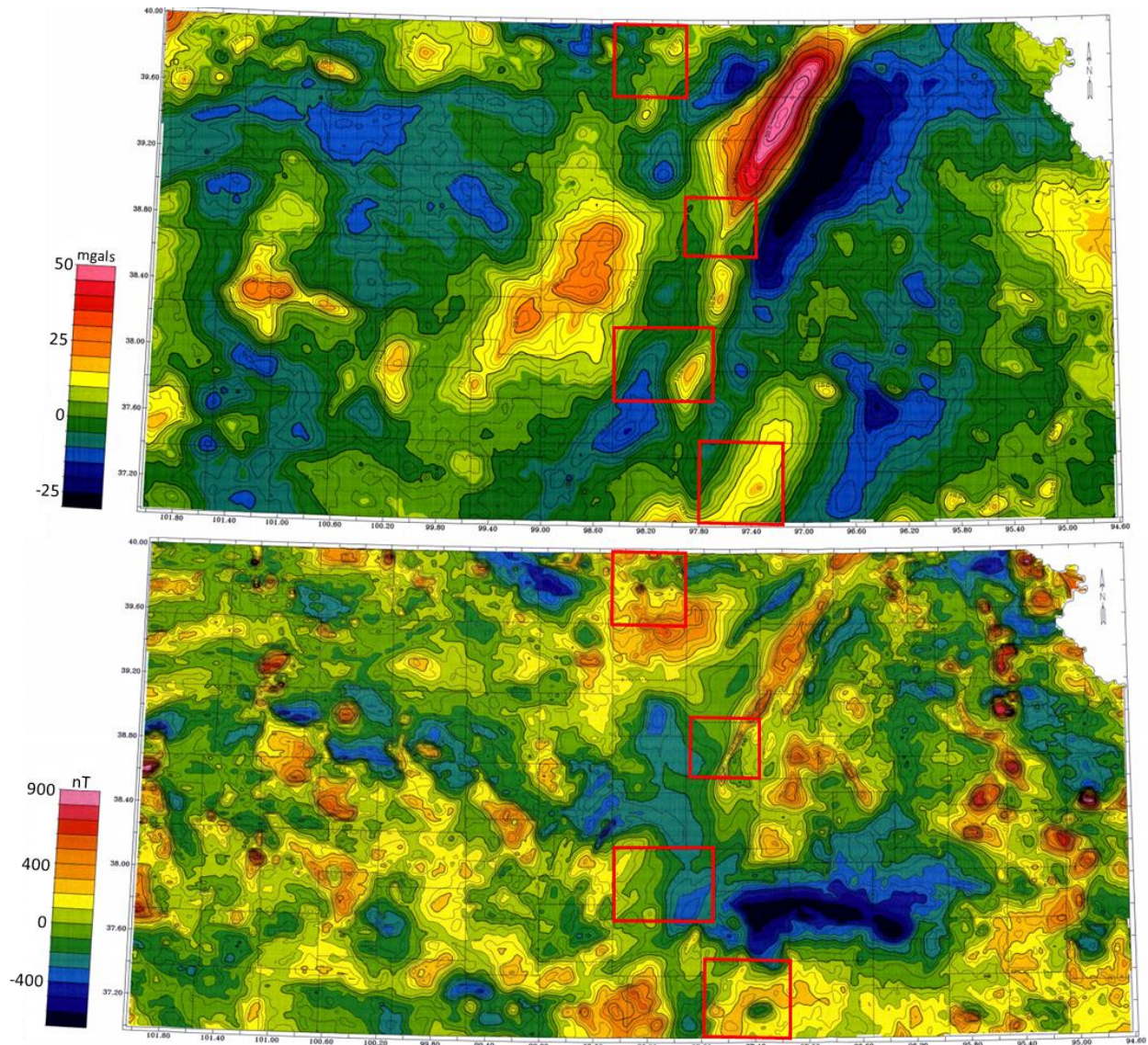


Figure 2-3 - Residual Bouguer gravity anomaly map (Top) from Xia et al., 1995a and Aeromagnetic map (Bottom) from Xia et al., 1995b. Blues represent low residual Bouguer gravity values and magnetic values. The bright pink spot is the strongest expression of this anomaly in the state. Reds represent high residual Bouguer gravity values and magnetic values. Maps modified to include areas of interest in this study (red lines).

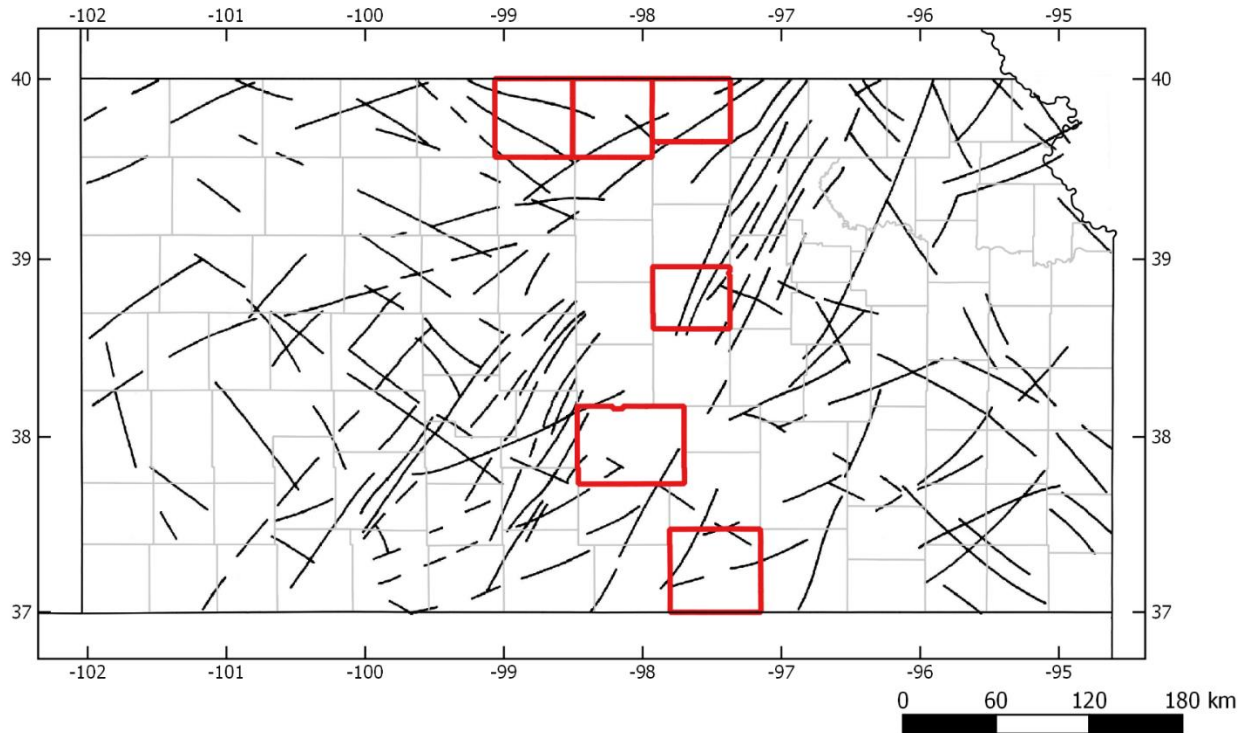


Figure 2-4 - Magnetic lineations derived from magnetic data in figure 2.3. Area of study for this paper are outlined in red. (Modified from Yarger, 1983).

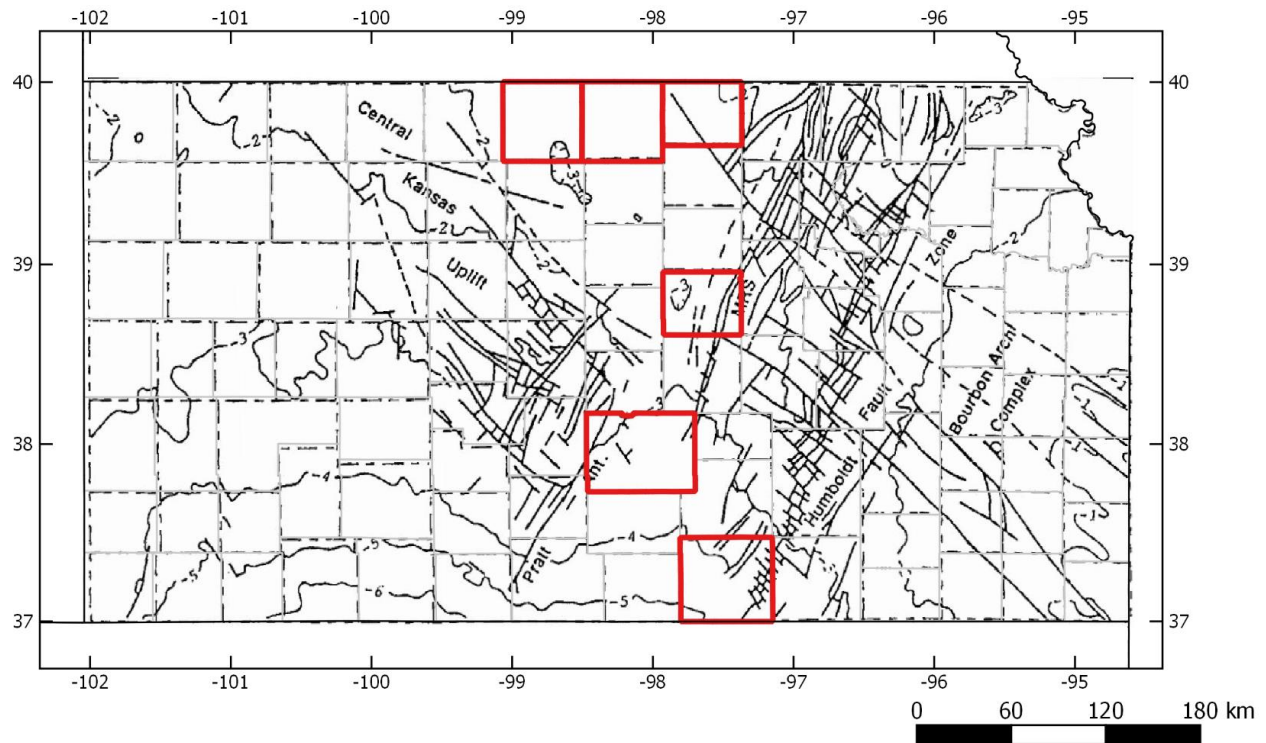


Figure 2-5 - Map of basement faults in Kansas. Counties outline in red from North to South are Smith/Jewell/Republic, Saline, Reno, and Sumner (Modified from Baars, 1995).

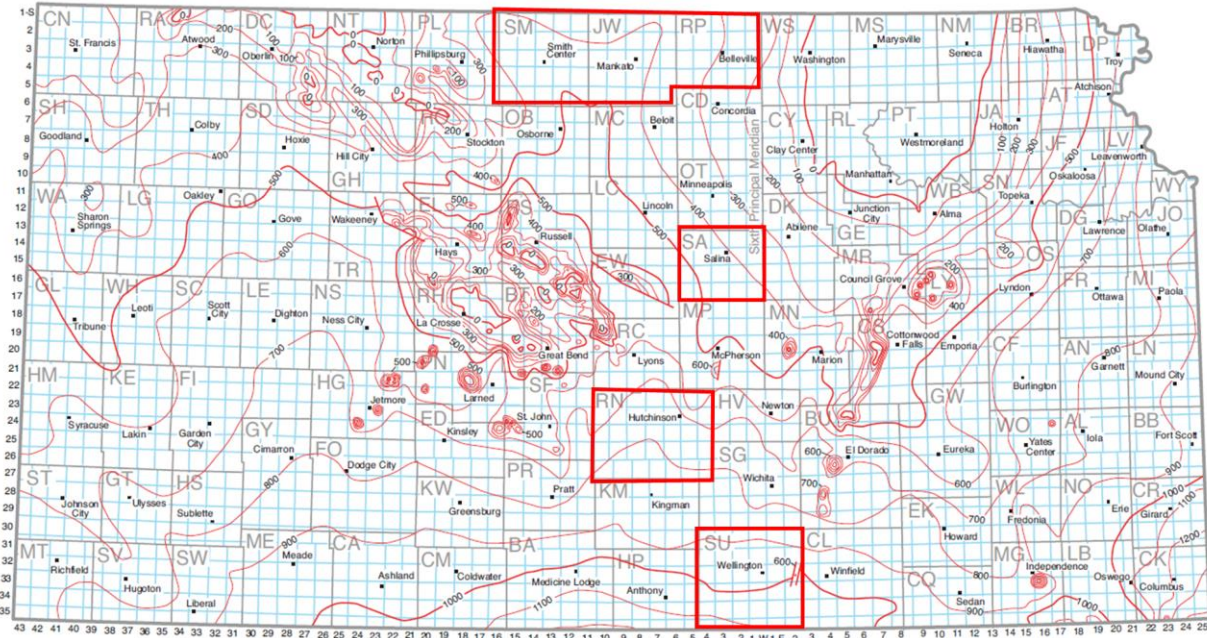


Figure 2-6 - Arbuckle Group isopach map from well data up to 1965 (Cole, 1975).

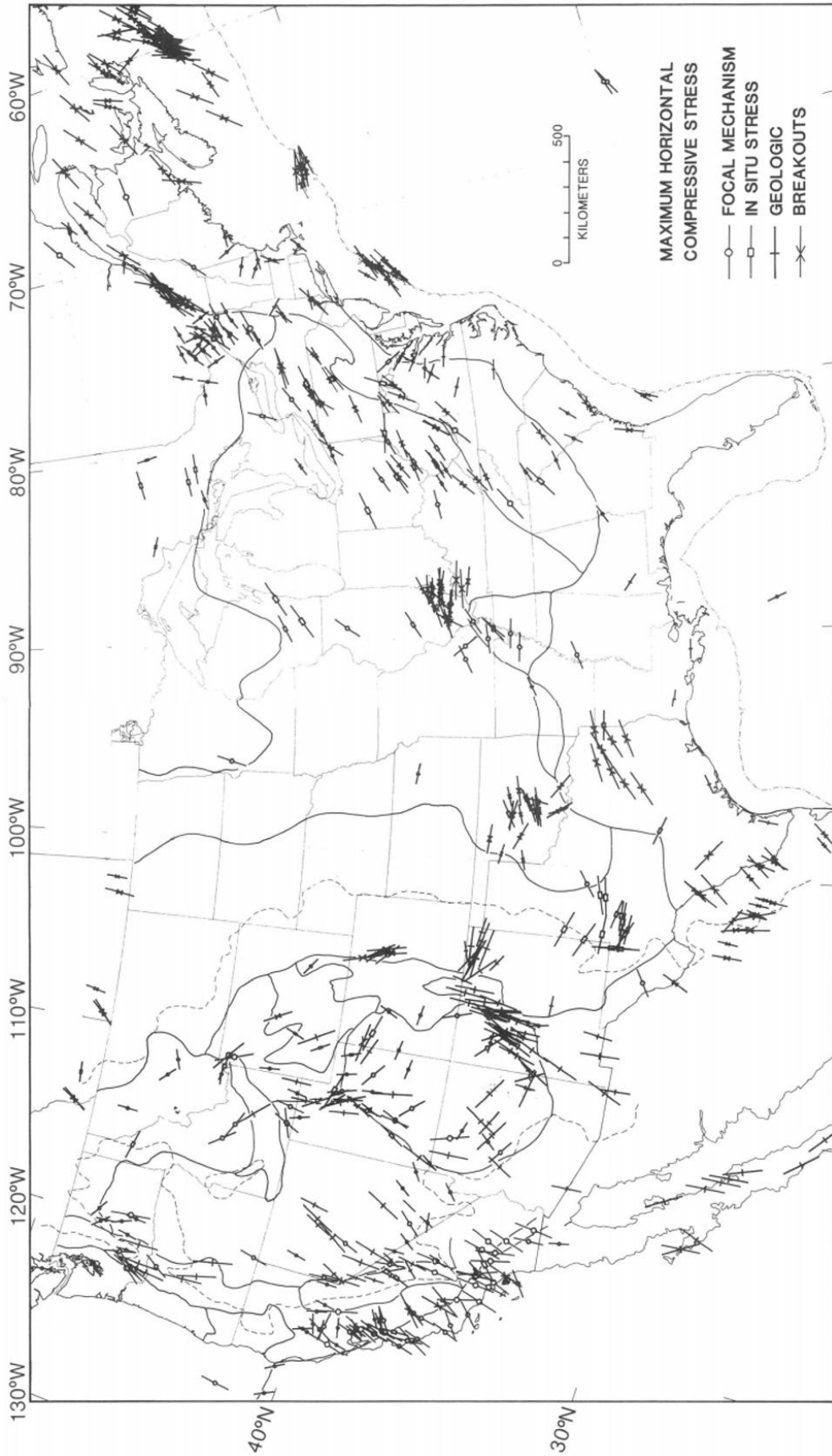


Figure 2-7 - Map of maximum horizontal compressive stress orientations, modified from Zoback and Zoback, 1989. Alt and Zoback, 2017 would provide one more data point within Kansas, but the stress state is unknown for a large portion of the state.

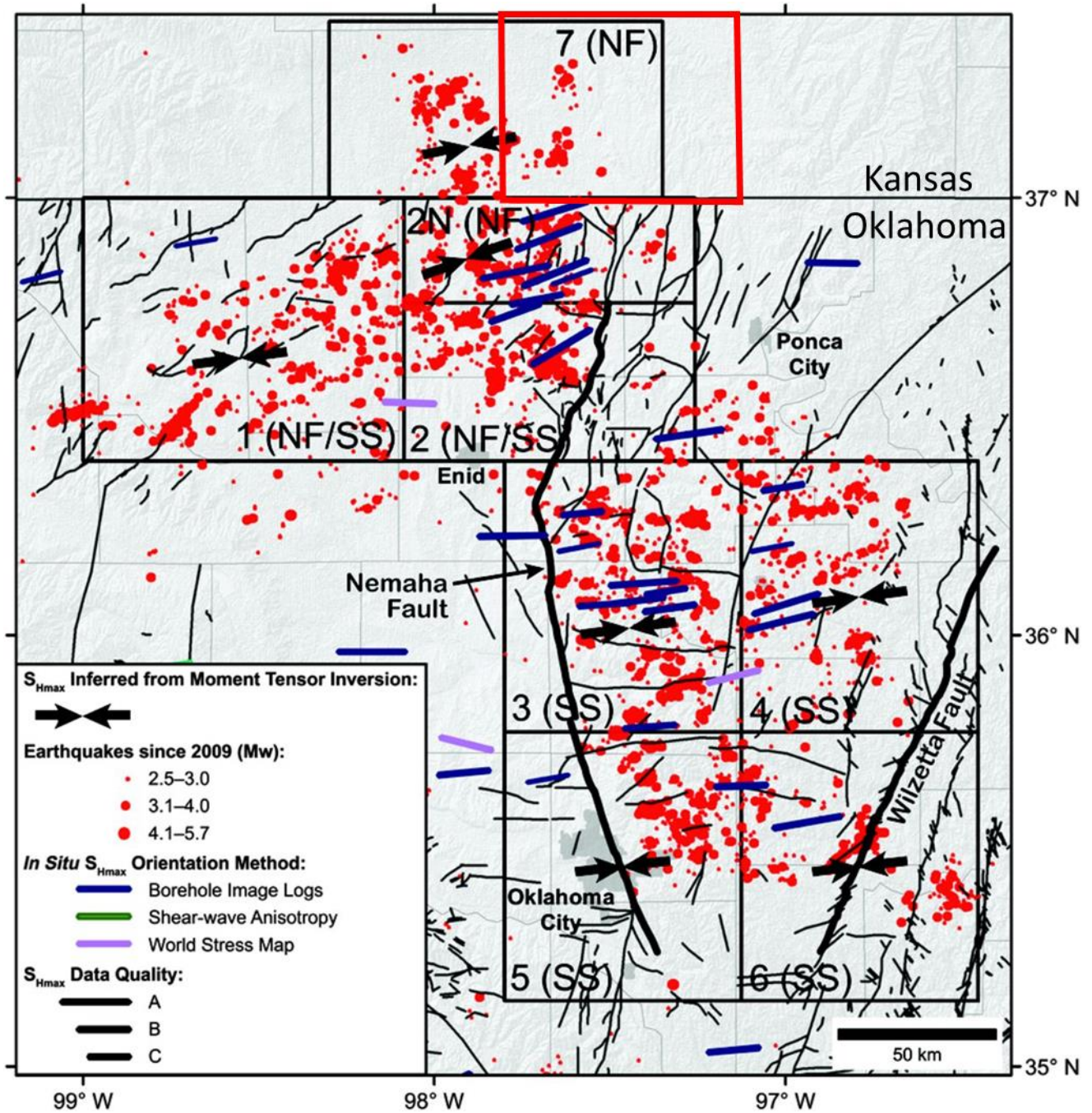


Figure 2-2-8 – Map of stress orientations calculated from both wellbore data and focal mechanism inversion. Red Box outlines Sumner County, an area of interest in this study. (Modified from Alt and Zoback, 2017).

Chapter 3 – Kansas Station History and Installation

Frequency of felt seismicity in the CUS has recently increased well above historical levels in the region. There have been few earthquake studies conducted specifically in Kansas since 1867. The number of stations within the state peaked in late 2017 at 65 stations but has had long periods of none to two active monitoring stations at scientific quality within the state (Figure 3.1).

Section 3.1 - Seismic Station History

The first government funded regional seismic network in Kansas was deployed in 1977 original designed to focus on US Army Corps of Engineers and Nuclear Regulatory Commission assets. The network would later expand into Nebraska and included 15 stations (Figure 3.2); nine stations in northeastern Kansas and six stations southeastern Nebraska. A 1987 study was the culmination of 13 years of earthquake records and attempted to relate seismic activity to tectonic features to establish a better understanding of seismicity in Kansas; namely active faults, recursion relationships and max ground shaking potential in a 100 year time frame. The study specifically focused on the nuclear power plant site and proposed flood control reservoir safety plans (Steeple et al., 1987).

After the decommissioning of this KGS operated 15 station network in 1989 no more than two seismic stations were located in Kansas and providing regional monitoring until 2009. These two stations are the longest continuously operating stations within the state and are located at Cedar Bluff and Manhattan.

In 2009, the EarthScope Transportable Array was temporarily deployed along a grid through the central portion of the United States (ANF, 2019). This project featured a temporary station array designed for investigations into local, regional and teleseismic events as well as 3D resolution of crustal and upper mantle structures (Busby, et al., 2018, Astiz et al., 2014). Overall, 45 stations were installed

across the state between April 2009 and May 2010. Stations recorded for approximately 24 months and then were decommissioned and moved to the next planned location elsewhere in the country (Figure 3.2).

The next regional network that operated in Kansas was deployed by the USGS. The USGS installed a dense network of 13 seismic stations in Harper and Sumner counties in reaction to the area experiencing a drastic increase in felt seismic activity. In late 2014, the Kansas Geological Survey (KGS) deployed six additional stations designed to surround the dense USGS network in hopes of extending the coverage and sensitivity to a ten county area. As seismicity continued with the development of new swarms outside the original ten county area, the KGS installed eight additional regional stations. These regional stations were installed and designed for long term monitoring of the entire state. At its peak, Kansas was home to 65 seismic stations (22 USGS (IRIS-DMC), 15 Wellington CO2 Sequestration Project (Nolte, 2018), 16 KGS (above) and 12 proprietary), and has had an average of 58 stations from 2017-2018 (Figure 3.3).

Section 3.2 - Station Configuration

Each KGS seismic station contains a three-component seismometer placed on a buried concrete pad within a vault approximately 1m beneath the ground surface. A solar panel, antenna, digitizer, cellular modem, battery and charge controller were installed on a pole approximately three meters from the sensor (Figure 3.4). A major difference between the regional/permanent and temporary stations is the sensor container. Temporary stations are covered with an inverted bucket and the regional stations are installed in a standard water meter vault with a fourth recording channel collecting data from a downhole vertical seismometer. Figure 3.5 shows a schematic rendition of a typical temporary seismic station installed by the KGS.

Seismometers are Guralp CMG-6T Broadband sensors which are capable of sensing ground motion over a wide range of frequencies with the flat-to-velocity portion of the bandwidth from 1sec to 100Hz. Data was recorded at 100Hz (100 samples per second) using a Reftek RT130S Digitizer and then transmitted, via cellular telemetry, to the KGS. The KGS stores, analyzes, maintains and archives all seismic data acquired from this network. Stations outside of the KGS (network code KM) have varying configurations that can be found using IRIS gmap tool (IRIS-DMC, cite).

Section 3.3 – Historical Seismicity in Kansas

Historical seismicity in Kansas dates back to 1867 and was originally compiled by Merriam (1956). Between 1867 and 1961 Merriam (1956), with later additions from Dubois and Wilson (1978) as well as Steeples (1990), compiled a catalog of 29 felt earthquakes located in Kansas (Figure 3-6). The first felt earthquake located in Kansas was later determined to have a magnitude of 5.1 (Stover and Coffman, 1993). Many of these earthquakes are located on or associated with the Nemaha ridge (Steeple et al., 1979).

From 1977 to 1989 the Kansas-Nebraska seismic network located 171 events within the state (Steeple 1989 and 1990). The network located numerous events in the western portion of the state despite only have stations for this network deployed in the eastern and central portion of the state (Figure 3-7). A majority of the events are likely from faults associated with the two prominent structures in the state – the Central Kansas Uplift and the Nemaha Ridge. Steeples (1990) notes the drastic increase in seismicity on the Central Kansas Uplift, this area has continued to be seismically active to today. In addition to this new cluster, a small trend of earthquakes in the north-central portion of the state run roughly parallel to MGA.

From 1990 to 2014 the USGS located 23 earthquakes in Kansas (Figure 3-8). From the decommissioning of the Kansas-Nebraska network to 2013 the network configuration of seismographs

monitoring Kansas reliably detected all earthquakes M3.4 and above (Rubinstein et al., 2018). Over half these events are located on the Central Kansas Uplift.

From 1867 to 2014 various networks have cataloged two earthquakes in Jewell County, the most recent event being a M3.3 in January 2013. During the same time there were no earthquakes located in Saline or Reno County. One of the most seismically active counties in Kansas today, Sumner County, had two small (>M2.0) earthquakes in 1979, more recently a M2.7 in 2008 and a M3.8 in 2013 (NEIC, 2019).

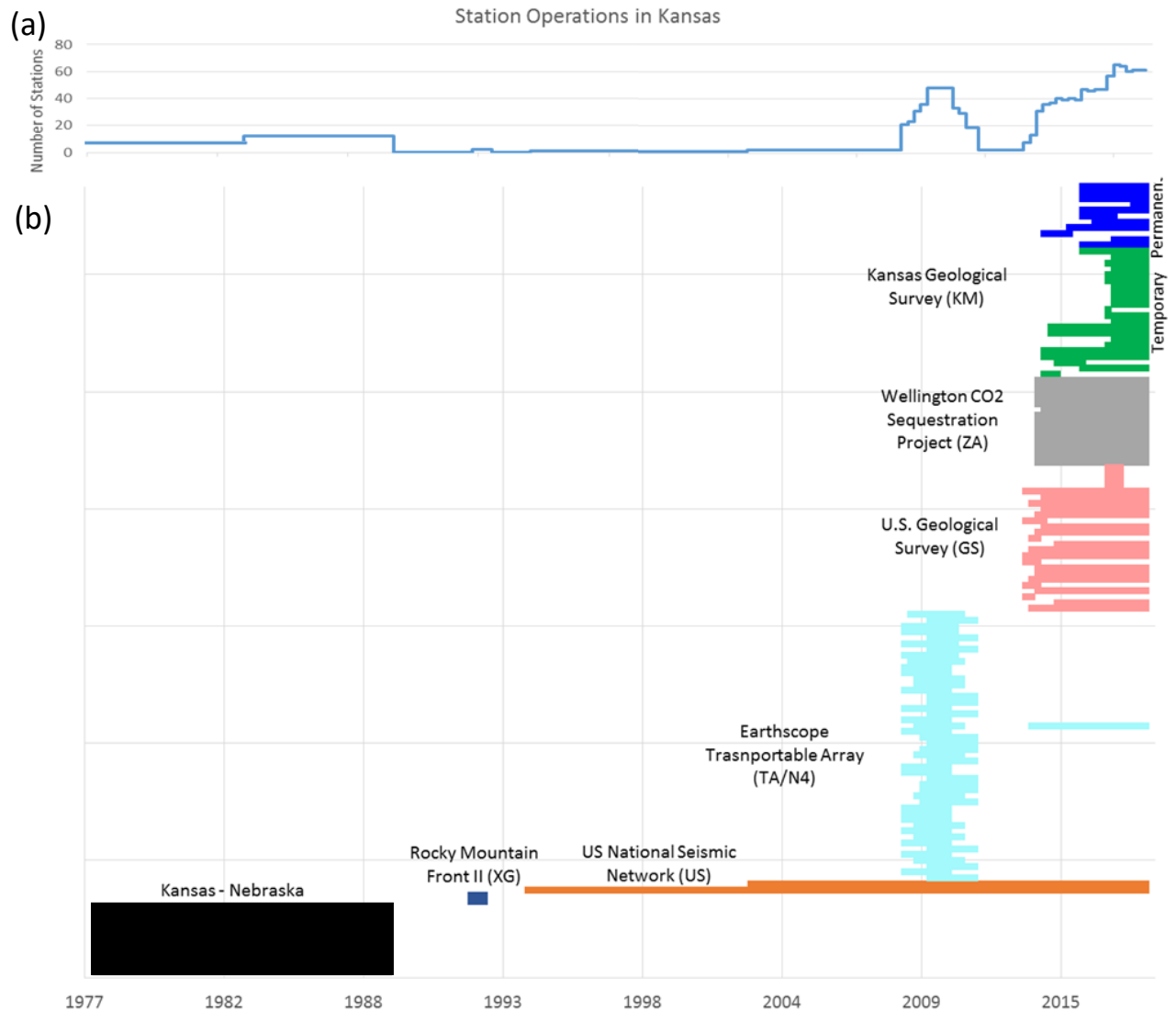


Figure 3-1 - (a) Count of operational seismometer stations in Kansas per quarter. (b) Station installation timeline, horizontal blocks represent a stations active period. Color groupings represent network, as indicated. Certain Transportable Array stations were converted into permanent stations making up a new network – Central and Eastern US Network (CEUSN), network code N4. One station in Kansas was converted (R32A, now R32B). Operational efficiency of various stations installed after 2014 and not part of the KGS network may be poor. These data points do not reflect station downtime, only commission to decommission time periods.

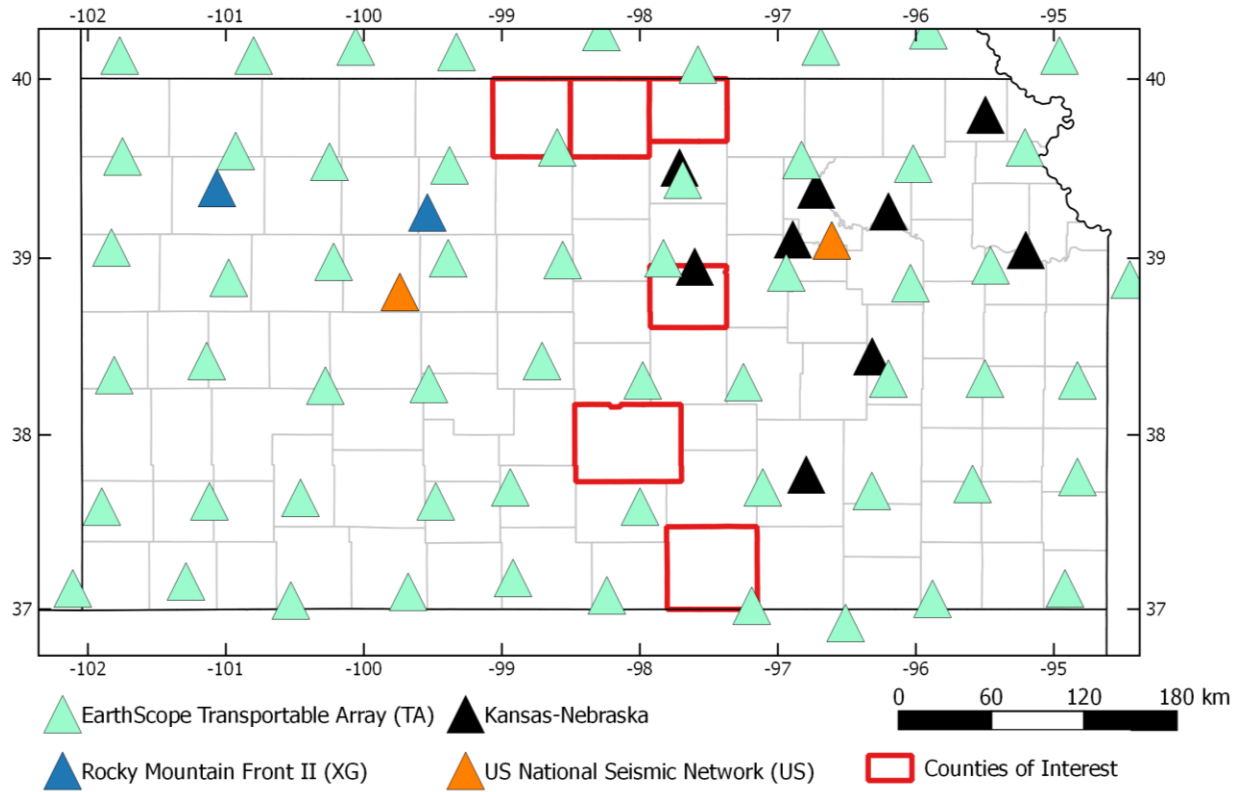


Figure 3-2 - Map showing the locations of seismometers that operated in Kansas from 1977 to 2013 – Kansas-Nebraska Network (KSNE – not in IRIS) operated from 1977 to 1989, Rocky Mountain Front II (XG) operated in 1992, and the EarthScope Transportable Array (TA) had varying station coverage from 2009 to early 2012.

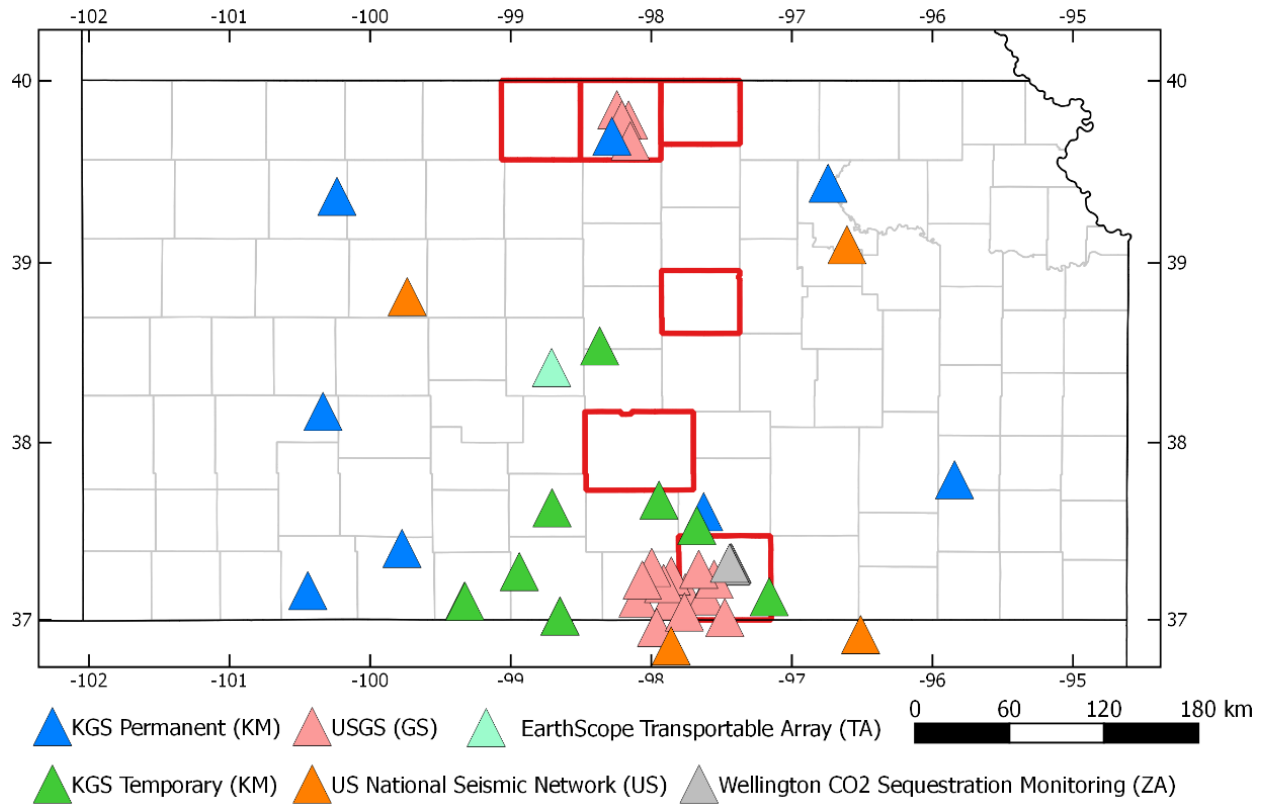


Figure 3-3 - Map showing the locations of seismometer that operated in Kansas from 2014 to present day – Kansas Geological Survey Primary and Temporary networks (KM) deployed in 2014, US Geological Survey networks (GS/US) deployed in early 2014, and the Wellington CO2 Sequestration Monitoring Project (ZA) deployed in mid-2014. The single Transportable Array Station converted to a permanent station can be seen in the middle of the state, this station is now actively apart of the Central and Eastern US Network (CEUSN), network code N4. All networks are still operating in Kansas to some extent. Red Boxes outline counties of interest.



Figure 3-4 – Typical earthquake seismic station (top right), inverted bucket housing seismometer (bottom right) and equipment box attached to the solar panel pole (left).

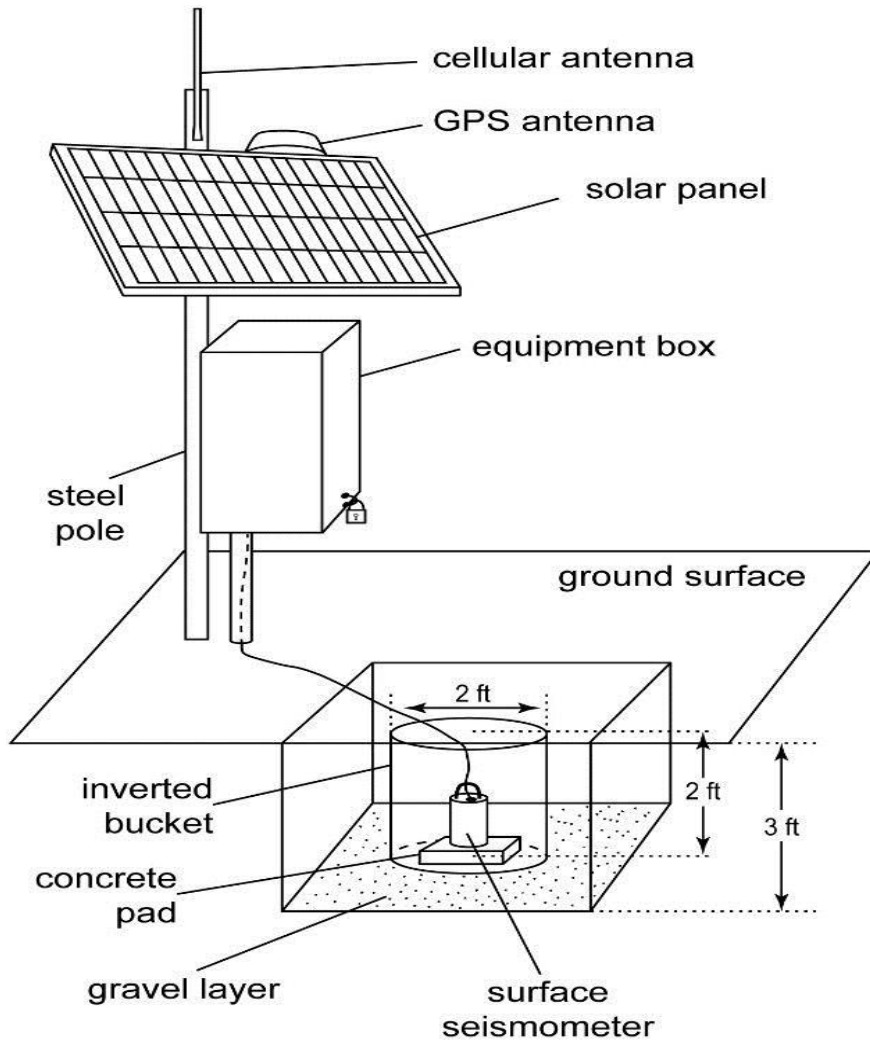


Figure 3-5- KGS Station schematic depicting all the components needed for a seismic station. (Credit: Mary Brohammer, KGS)

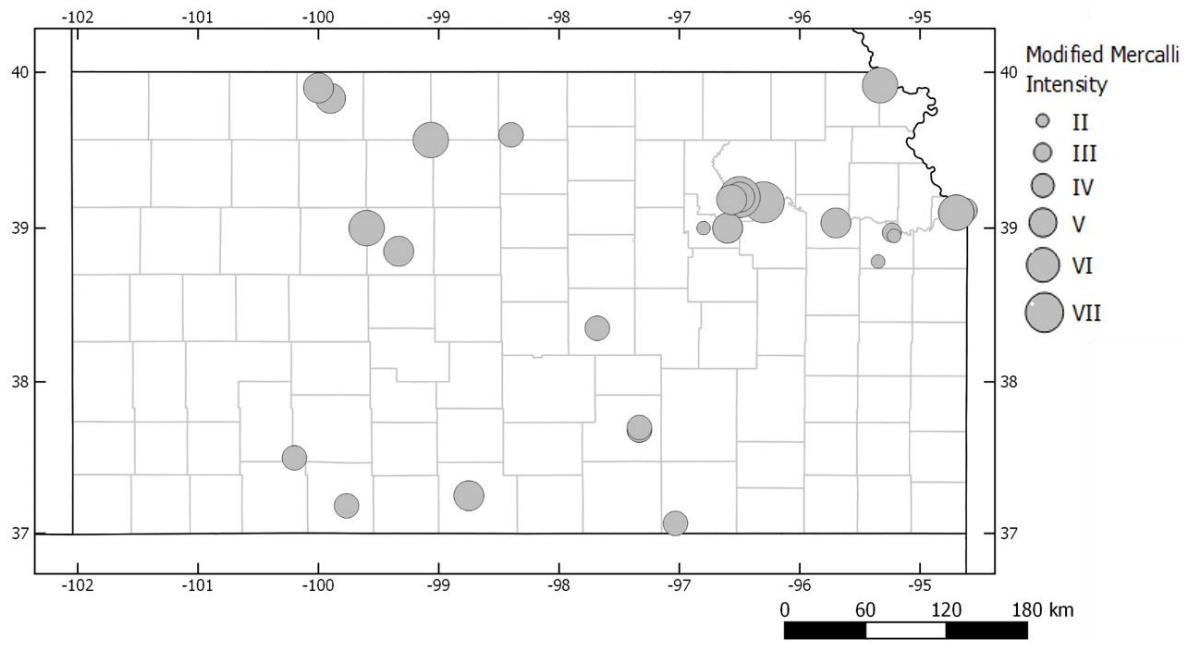


Figure 3-6 - Felt earthquakes located in Kansas from 1867 to 1961 (Dubois and Wilson, 1978).

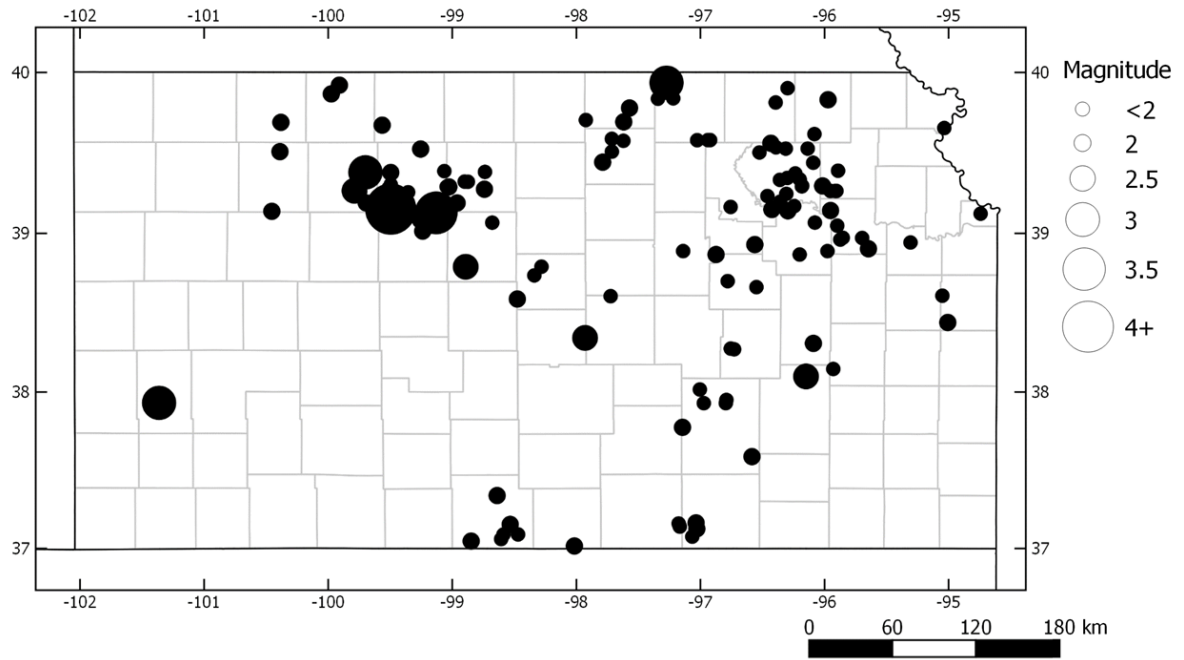


Figure 3-7 - Historical seismicity in Kansas from 1977 to 1989 (Steeple et al., 1990).

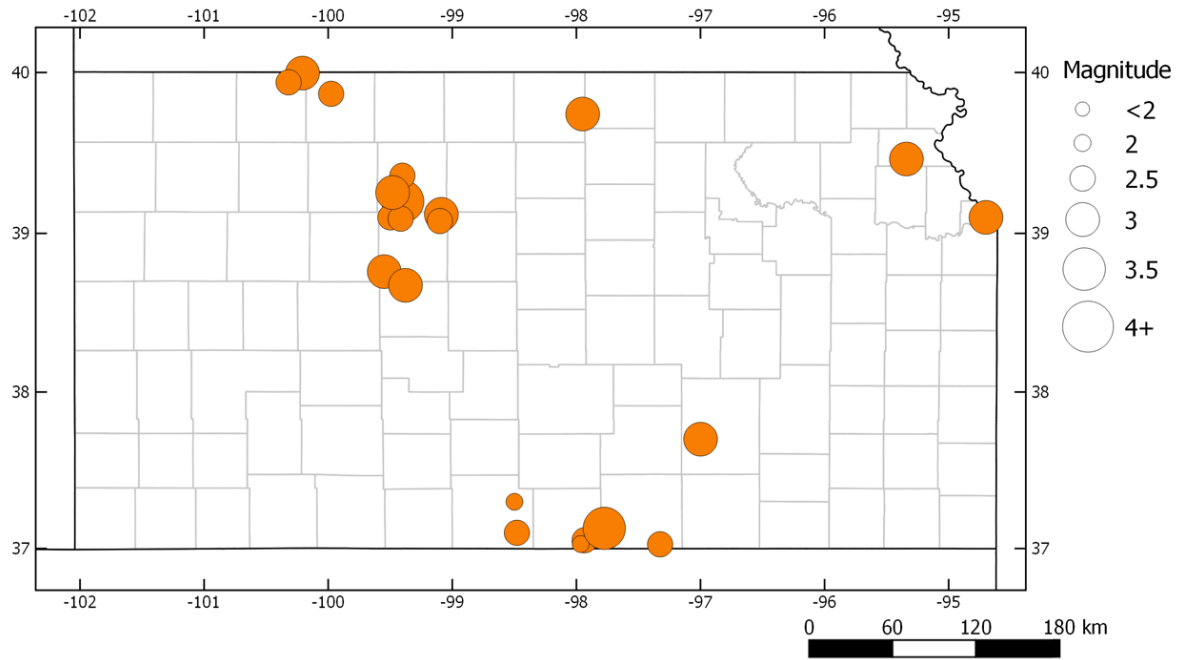


Figure 3-8 - USGS located earthquakes in Kansas between 1990 and 2013 (NEIC, 2019).

Chapter 4 – Cataloging Earthquakes in Kansas (2015-2018)

Earthquakes across the state have been cataloged by the KGS since January of 2015. Continuous data is recorded across the state, transmitted via cellular telemetry to the KGS where it is processed, analyzed and archived. Data used in this study from 2015 to current include the KGS waveforms combined with data from the three other networks operating within the state.

The KGS utilizes an automated analysis procedure followed by a manual process requiring human interaction. Resulting waveforms and epicenters provide scientists and government officials with the necessary information to make up-to-date and informed decisions.

Section 4.1 - Identifying and locating Earthquakes from Seismic Data

Continuous data for all stations are processed using Earthworm, which is an open source software package commonly used in seismology for data processing and archiving seismic events (www.ISTI.com). This processing routine provides automated detection and location of events in Kansas including an initial calculation of basic earthquake attributes. Simultaneously, raw data are converted into hour long MiniSEED files which are then analyzed using SeisAN, an industry standard software package used in earthquake analysis (Ottmoller et al., 2016).

Earthworm uses a ratio of sliding averages of the long term amplitude (LTA), 8 seconds long, to short term amplitude (STA), 1 second long, to determine anomalous spikes in the seismic data. When the LTA/STA ratio reaches a certain threshold there is a “trigger”. One benefit of this method over other more sophisticated methods is there is no requirement for an example event waveform or specific source mechanisms; as is the case with cross-correlation or any template matching method. This method is especially effective at detecting new clusters outside a known seismic area.

When multiple stations trigger coincidentally, Earthworm generates a file of raw seismic data from all the stations used to locate the event. An automated email is sent to the analyst with location, attributes, and waveform data. Each data file is manually inspected to establish if the detected event is an earthquake or a false trigger. False triggers are thrown out. Analysts process the raw data sometime after the event triggers while Earthworm produces an earthquake parameter list in real time. This results in a lag between the catalog of events Earthworm produces (higher magnitude of completeness) and the final generated events from the KGS analyst.

Each hour of raw seismic data is inspected by a human analyst. This process is necessary to identify any events the Earthworm software did not detect. There are various reasons an automated system would not identify (or trigger on) an event. These include low signal-to-noise ratio, delayed telemetry of data, false triggers overlapping actual triggers or the event was just too small for the algorithm to detect but they could be confidently identified with a human eye. False triggers could include: pump jack noise (Figure 4.1), which are easily identified by cadenced impulses and quarry blasts (Figure 4.2) that are similar to earthquakes. Quarry blasts typically have much more prominent surface waves, lack clear p- and s- wave arrival and sometimes can contain an airwave.

Manual processing and analysis requires the analyst to first inspect the hour long MiniSEED files of raw seismic data generated as data stream in from the stations. Then any events of interest are cut from the hour long files into smaller segments containing the entire earthquake waveform as well as adequate background signal before and after to help identify different parts of the wavetrain.

To locate an earthquake from seismic data the first step is to identify the compressional wave and shear wave arrival at each station. The compressional P-Wave is the first body wave to reach the sensor. A P-Wave's particle motion is in the direction of propagation making it the fastest wave and is typically smaller in amplitude than the shear wave amplitude. The shear, or S-Wave, arrives after the P-

Wave, but is easily identifiable by its larger amplitude compared to the background signal (Figure 4.3). The larger amplitude can often be mistaken for the surface arrival which is similar in velocity to the S-Wave velocity, $V_{\text{surface}} \approx 0.9V_s$. This misidentification contributes to the error in origin time and location of the event but is negligible. The P-Wave is picked on the vertical (or Z) channel and the S-Wave is picked on the horizontal channels (E and N, or 1 and 2).

After identifying all possible p- and S-Wave arrivals from each station the distance to the epicenter for each station can be calculated using a generalized velocity model of Kansas (Figure 4.4) from Steeples et al., 1987. The distance from each station to the epicenter is then used to triangulate the location of the event. The S-Wave velocity is calculated from the P-Wave velocity and V_p/V_s ratio. This model differs from models used in other studies (Rubenstein, 2018; Nolte, 2017; Choy, 2016) and calculated from a reverse seismic refraction study done by the USGS (Warren, 1975; Steeples, 1976; Steeples et al., 1988). Having an accurate velocity model is vital to accurately locate earthquakes and calculating magnitudes (Haskov, and Alguacil, 2016).

Section 4.2 - Earthquake Magnitudes

There are various calculations that quantify the strength, or magnitude, of an earthquake. The goal of these calculations are to quantify the energy release to estimate the potential damage of an earthquake, express the physical size of the earthquake and predict seismic hazards (Havskov and Ottemoller, 2010). Some of these methods for calculating magnitude are derived from the duration of shaking, that is the coda, and other are more complex and are derived from spectral characteristics.

Coda Magnitude - M_c

The simplest magnitude to calculate for an earthquake is the coda magnitude, or duration magnitude (Havskov and Ottemoller, 2010). After the primary waves from a local earthquake have passed the seismometer, a complex series of small vibrations that originated with the earthquake arrive

from diverse travel paths with decreasing amplitudes over time. This portion of the wave field is called the coda. These smaller vibrations are the backscattered primary waves due to lateral inhomogeneities in the crust (Aki and Chouet, 1975), the coda can be used to estimate magnitude. The coda magnitude can be expressed as a function of the duration of the coda and the spatial distance from the earthquake epicenter:

$$M_c = a * \log(coda) + b * distance + c \quad (\text{Equation 4.1})$$

Here, coda is the duration of the backscattered waves in seconds and a , b and c are constants. Smaller events that are only detected on noisy stations have smaller primary wave amplitudes and spectral characteristics that are unreliable. These factors make it difficult to estimate any other magnitude than duration magnitude.

Local Magnitude - M_l

The Local Magnitude (M_l), or Richter Magnitude, scale is defined such that a M3 earthquake recorded using a Wood-Anderson seismometer at 100km from the event would record a peak of 1mm (Richter, 1935). Data acquired on modern systems must be corrected for this standard to calculate M_l . A displacement trace can be produced by using the seismograph's poles and zeros response curves (Figure 4.5). Multiplying the new displacement trace calculated with the seismographs response curve with the Wood-Anderson instrument response generates a simulated Wood-Anderson Seismogram (Figure 4.6). The Wood-Anderson instrument poles and zeroes instrument response is similar to a 2 pole Butterworth high-pass filter at 3Hz and approximates the response such that M_l is within 0.1 magnitude units (Ottemoller, 2016). The maximum amplitude from the simulated seismogram is used in calculating the M_l according the equation below.

$$M_l = \log(amp) + a * \log(distance) - b * distance - c \quad (\text{Equation 4.2})$$

Here, *amp* is the maximum ground amplitude from zero to peak in nanometers and *distance* is in km.

Moment Magnitude - M_w

The moment magnitude (M_w) is the seismological standard for seismic events and can be calculated for any size event using both p- or S-Waves (Havskov and Ottemoller, 2010). This quantification of earthquake magnitude is related to the seismic moment (MO) and is a direct measurement of the radiating energy from the area of the fault that ruptured. This value is derived from spectral characteristics and used to calculate the moment magnitude (Kanamori 1977; Hanks and Kanamori, 1979; Ottemoller, 2016)

$$M_w = \frac{2}{3} \log_{10} MO - 6.06 \quad (\text{Equation 4.3})$$

MO is calculated from the cornering frequency (f_0) of the energy spectra and fundamental in calculating stress drop (Chapter 6). M_w is derived from source characteristics, MO, whereas other magnitude calculations are empirically defined as a distance corrected measurement of ground motion strength (Aki and Richards, 2009).

Section 4.3 – Magnitude vs. Frequency

All of these methods of quantifying earthquake strength generally follow the Gutenberg-Richter power law distribution of the magnitude and total number of earthquakes in an area (Gutenberg and Richter, 1956):

$$\log N = a - bM \quad (\text{Equation 4.4})$$

Here, N is the number of events with magnitude M, and *a* and *b* are coefficients. In natural cases *b* is expected to be at or near 1. This law states that for a *b*-value of 1 every M2 earthquake that occurs there should be 10 M1 events; likewise, for every M3 event that occurs there should be 10 M2 events

and 100 M1 events. The b-value can be calculated for any catalog using a plot of frequency vs. magnitude (Figure 4.4). Where the trend is flattest, the slope will be the b-value. B-values that exceed the standard Gutenberg-Richter value (1) for regions with natural earthquakes is one indication that seismicity may be related to increase pore pressures and as a result induced (Bachmann et al., 2012).

One of the most important quantities in assessing the quality of a catalog is the magnitude of completeness. This value quantifies the sensitivity of the network used to build the catalog and is the lowest magnitude at which the network confidently detects 100% of the events (Wiemer and Wyss, 2000; Woessner and Wiemer, 2005). The point of greatest curvature at which the frequency vs. magnitude trend diverges from the Gutenberg-Richter relationship (Equation 4.1) is the magnitude of completeness. Below the magnitude of completeness, the network still detects earthquakes but only a fraction of the events. These events are missed because of various reasons; the event is too small to record on enough stations, the event was not locatable within a reasonable error threshold, or the event is too small to be discriminated from other larger seismic events happening concurrently.

Section 4.4 - Earthquake Catalog and Database

A catalog of earthquakes that have occurred in the state is important for determining future seismic hazards. The primary components of the earthquake catalog are origin time, longitude, latitude and depth of the epicenter as well as magnitude. M_w was the primary magnitude reported for events that MO was able to be confidently calculated, M_l was reported after that and if all other variations of magnitude were unreliable the duration magnitude was reported.

The earliest published earthquake within Kansas was cataloged by Dubois and Wilson (1976) and dated back to 1867. From 1867 to 1972, 28 felt earthquakes were reported. These events were excluded from the catalog used in this study due to a lack of analog data and uncertainty in epicenters and magnitudes.

For events from 2015-2018 located using KGS stations the average longitude error was 1.54km and the average latitude error was 1.48km. The Jewell County area had the highest longitude and latitude errors, 1.88km and 1.87km respectively. The Reno County area had the smallest longitude and latitude errors, 0.88km and 0.86km respectively. It is important to note that a portion of this discrepancy is likely due to variations in velocity models, different station coverage, and depth of events. Clusters near the KGS temporary stations will have less spatial errors than clusters further away. Events located by the KGS have a fixed depth of 5km. The catalog of earthquakes used in the subsequent chapters can be seen in the Appendices with a complete catalog of all events located by the KGS since 2015 on the KGS web site (www.kgs.ku.edu).

To aid in managing and utilizing the large volume of data generated by the various networks located in Kansas, the KGS developed its own relational database that merges the historical data sets (i.e. Steeples et al., 1987), NEIC, and KGS data sets into a single database. As new data are being continuously recorded, raw data files are processed and integrated into the database in real time, parsing out the requested usable information, and the results displayed in real time on KGS supported online GIS (mapping) systems. Simple SQL statements can be used to analyze the data, generate statistics, or other activities useful to scientists and policy makers. For example, Table 4-1 shows the number of earthquakes located in each Kansas county (earthquake events ≥ 100).

Section 4.5 - Earthscope Transportable Array (TA) Data

From 1989 to 2014, there were only two stations operated by the USGS in Kansas (Figure 3.1). However, a relatively unknown network did operate in Kansas during this time period, the Earthscope TA network. 19 stations were installed in the western half of the state by mid-2009, by the end of 2009 a large portion of the central part of the state had seismic coverage; it wasn't until May of 2010 that the eastern portion of Kansas began installation (ANF, 2019). To date, there are no USGS publications on

seismicity within the northern part of Kansas utilizing the TA data. In fact, aside from the initial analysis of the data (Asitz et al., 2014), no published catalog of earthquakes includes this data.

The Frohlich criteria for discriminating earthquakes hinges on the accuracy and understanding of historical seismicity in an area (Davis and Frohlich, 1993; Davis et al., 1995). Our understanding of historical seismicity was outlined In Chapter 1 and concluded that based on the catalogs published to date much of the state is seismically quiescent up to the development of new clusters in the south-central Kansas in 2014. The TA provides a short period of time where large portions of the state were monitored using a network with 60-80km station spacing, a drastic improvement on the two stations operated by the USGS during the same time period. The emplacement of this network in late 2010 and early 2011 predates the proliferation of saltwater disposal in Kansas around 2012 (Peterie et al., 2018). The incorporation of the TA data thus significantly improves our understanding of background seismicity in the state.

One of the most seismically inactive counties in the state historically is Jewell County. However, this area has recently experienced new clusters of earthquakes developing since 2016. Prior to the increase in seismic activity Jewell County has recorded one earthquake in 2013 (NEIC, 2019). We looked at the TA data to better understand the background seismicity of the area. The Jewell County Area has the best TA station coverage from May 2009 to March 2011. Raw seismic data was pulled for the nine TA stations surrounding Jewell County (Figure 4.7) from the IRIS website from May 2010 to March 2011. This approximately 10 month time period was selected despite each station being emplace for nearly two years because all nine stations were installed and collecting data giving the best azimuthal coverage of the study area. The same automatic detection method used today (Chapter 4 Section 1) to identify earthquakes in real time was used to process and identify the 10 months of data.

The analysis from this data set provides a link between historical seismicity and provides a better understanding of pre-injection seismic activity in the area. Although no earthquakes were recorded as located within Jewell County (Figure 4.8) between May 2009 and March 2010, nine additional earthquakes in the area were identified and located that were not detected in the past. This leads us to believe that the network would have detected any earthquake in Jewell County over the time period. The fact it did not supports our historical understand of seismicity in the county.

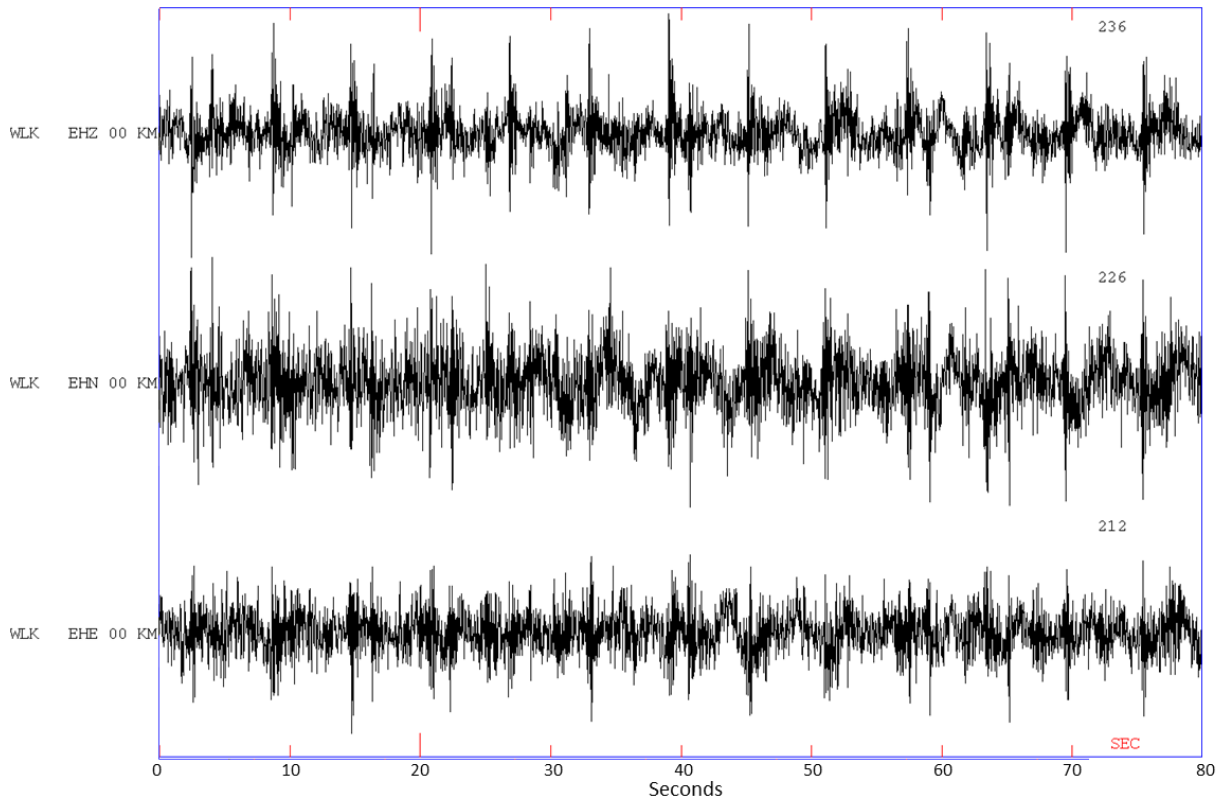


Figure 4-1- Example of pump jack noise from a KGS Regional Station. In an effort to place regional network stations in areas with the best signal to noise ratio for optimal monitoring, this station was moved further away from the noise source. The cyclicity of a pump jack degrade the signal continuously and interferes with both the automated and manual process of detecting earthquakes.

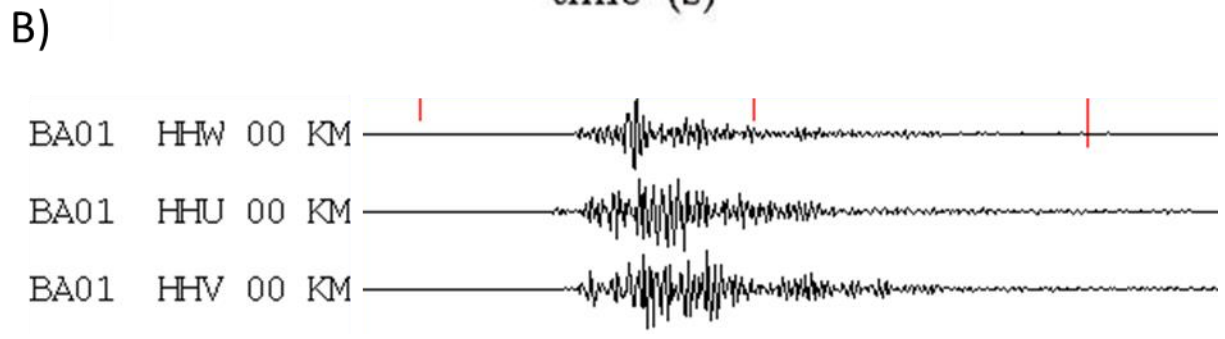
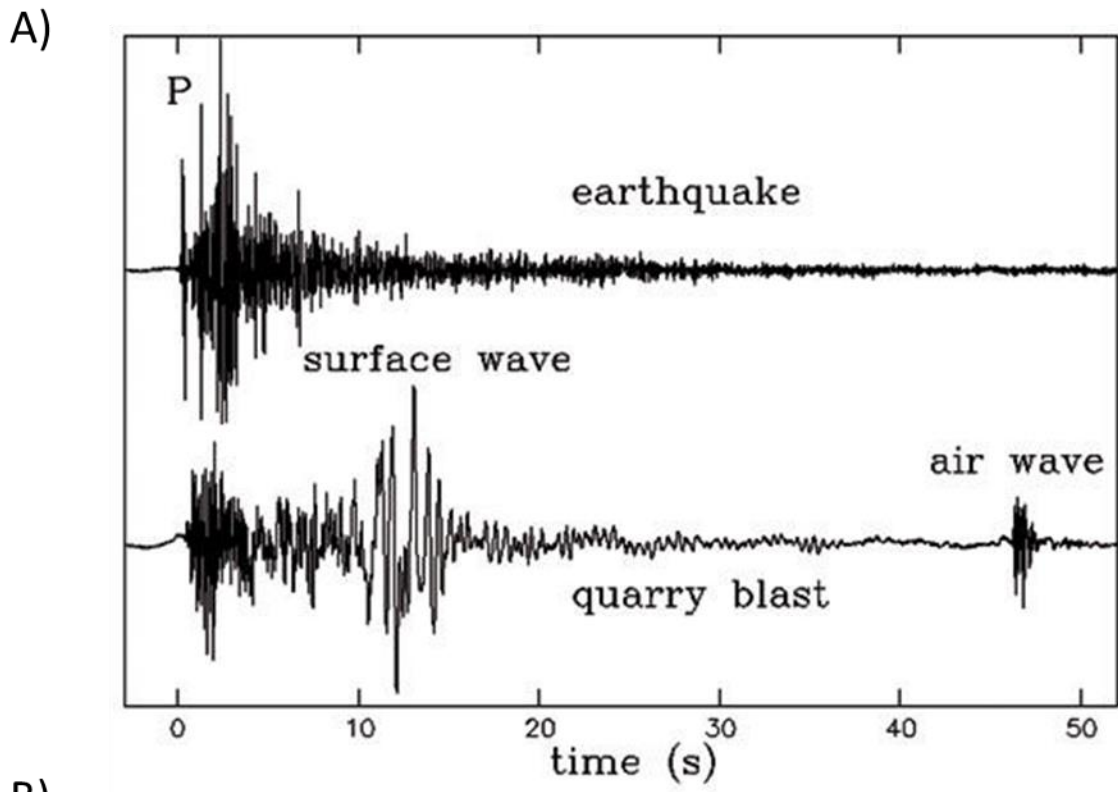


Figure 4-2– A) Vertical component seismograms from an earthquake (top) and quarry blast (bottom) taken from Frohlich, 2012. The prominent surface wave of the quarry blast is easily identifiable within raw seismic data. B) Example of quarry blast observed in Barber County, Kansas.

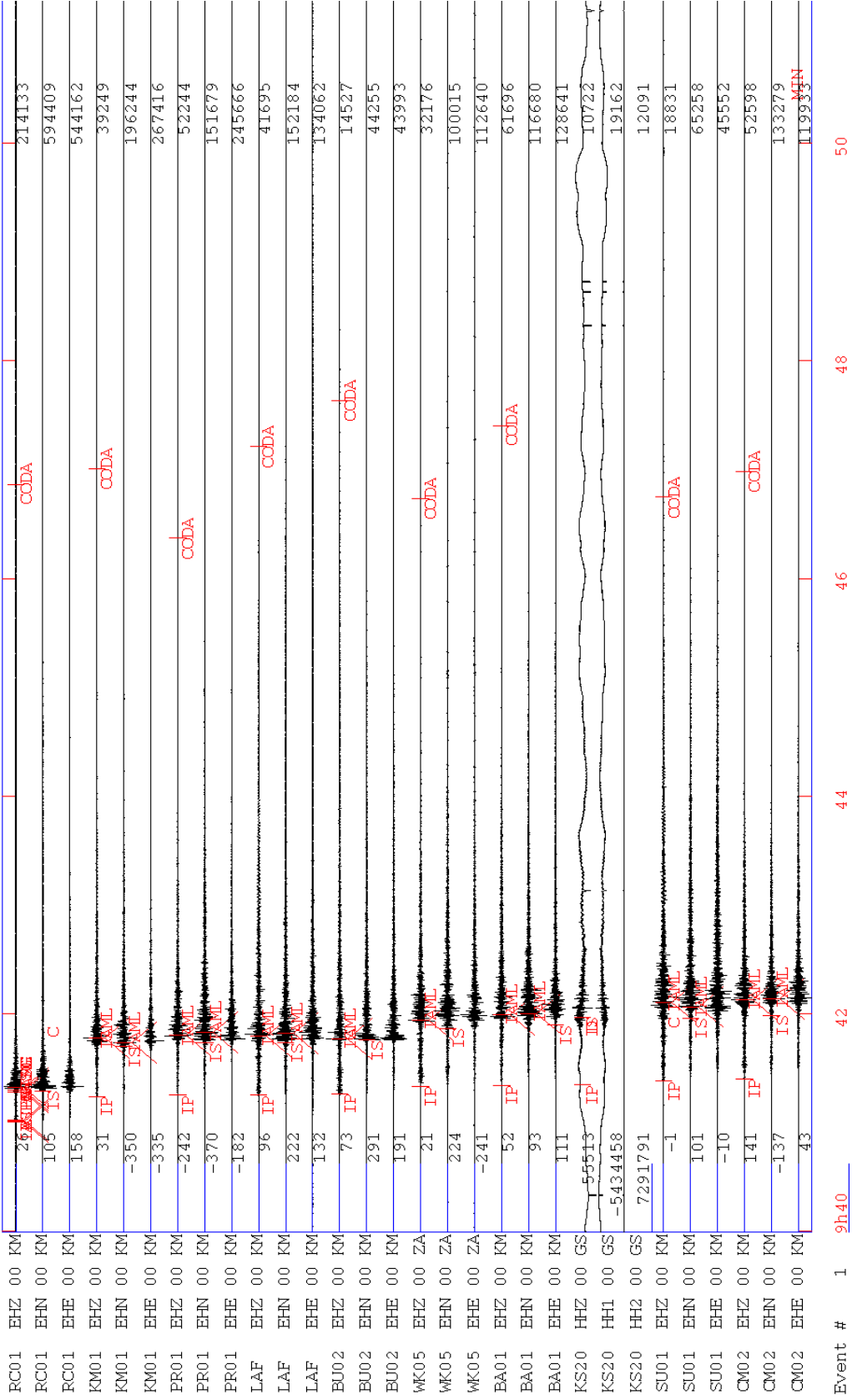


Figure 4-3 - Example of raw seismic data taken from 10 stations across the state. The event shown is the largest magnitude seismic event recorded from Jewell County to date. The 3.9Mw earthquake occurred on June 13th, 2017 at 4:40AM. On the left are the Station, Component, Network, and Location (SCNL) of each sensor used in the analysis. P-Wave arrivals are denoted by 'IP', and S-Wave arrival is marked with an 'IS'. The end of the backscattered wave, the coda, is marked by 'CODA'.

Table 1
Crustal Model

Velocity	Depth
2.40	0.000
4.50	0.526
6.00	1.300
6.10	8.113
8.25	42.000

Frequency vs. Magnitude

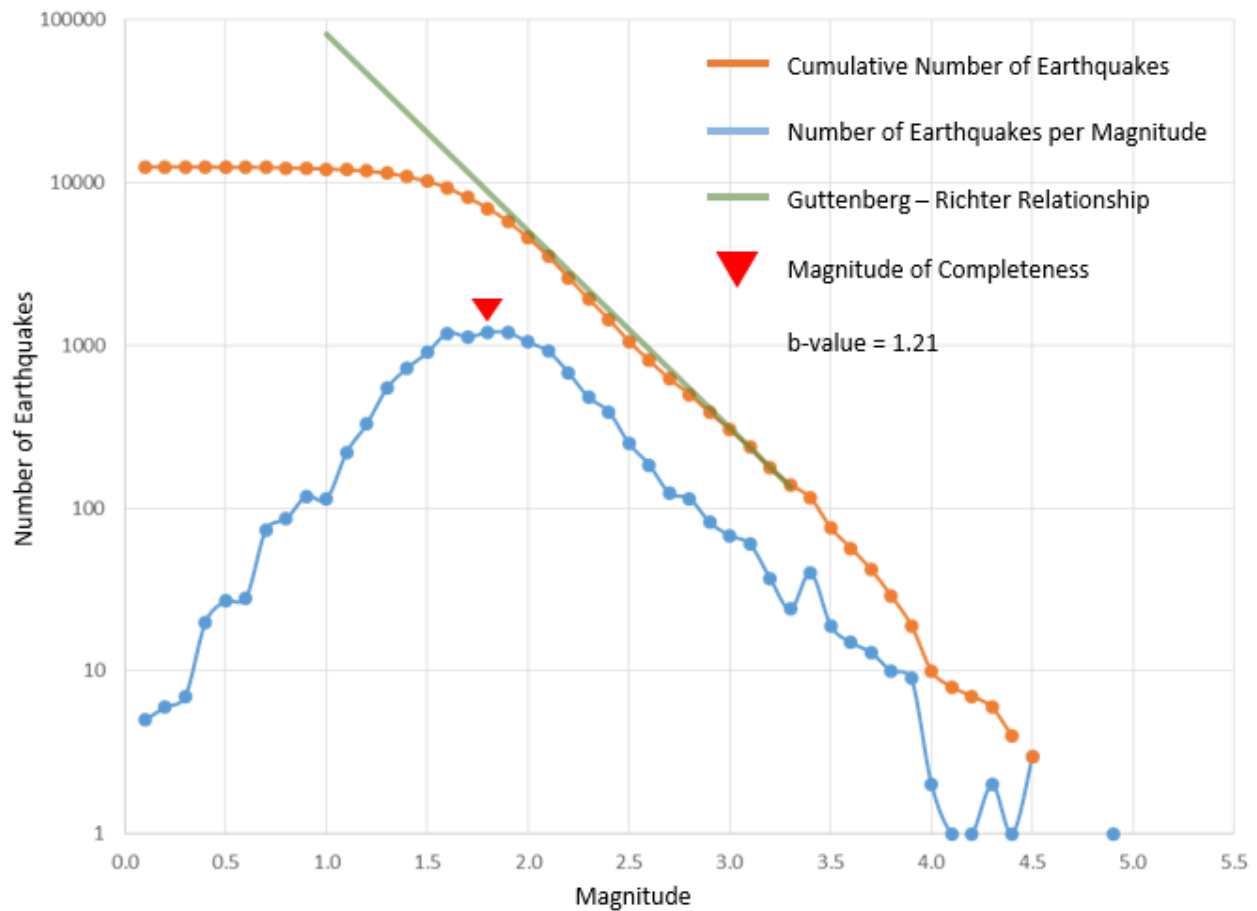


Figure 4-4 - Plot of earthquake frequency versus magnitude. Earthquakes were grouped every 1/10th of a magnitude. Gutenberg-Richter Relationship (Green) is used to describe the recursion of higher magnitude events and assess the completeness of the catalog used.

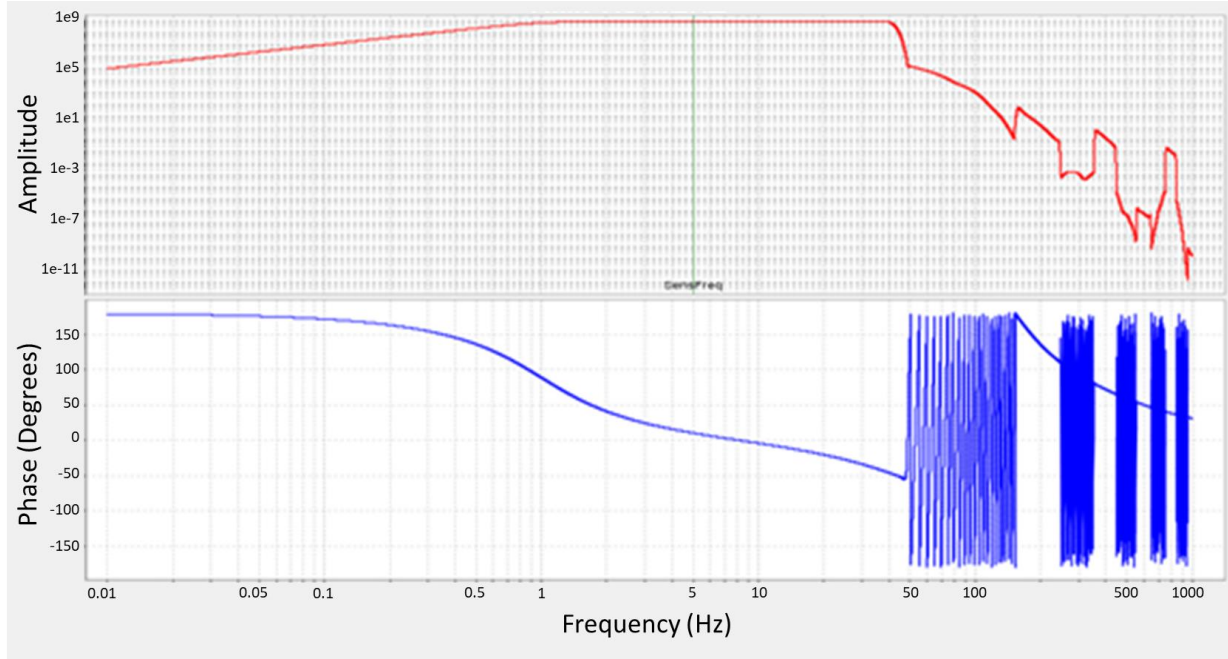


Figure 4-5 - Instrument response correction generates simulated Wood-Anderson seismographs which is used in determining Magnitudes.

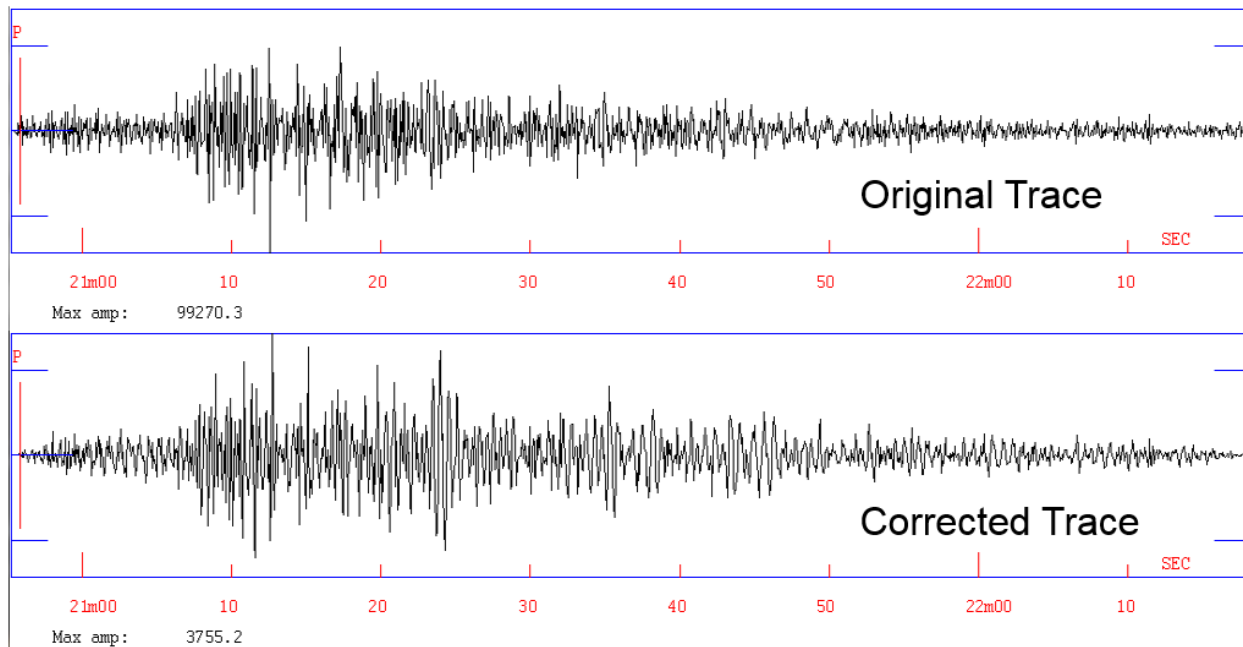


Figure 4-6 - Instrument response correction generates simulated Wood-Anderson seismographs which is used in determining Magnitudes.

Table 2
Counties with +100 events

County	Number of Events
Harper	4365
Sumner	4246
Barber	841
Sedgwick	585
Kingman	553
Reno	408
Comanche	331
Trego	269
Saline	207
Butler	185
Rooks	135
Jewell	129
Dickinson	100

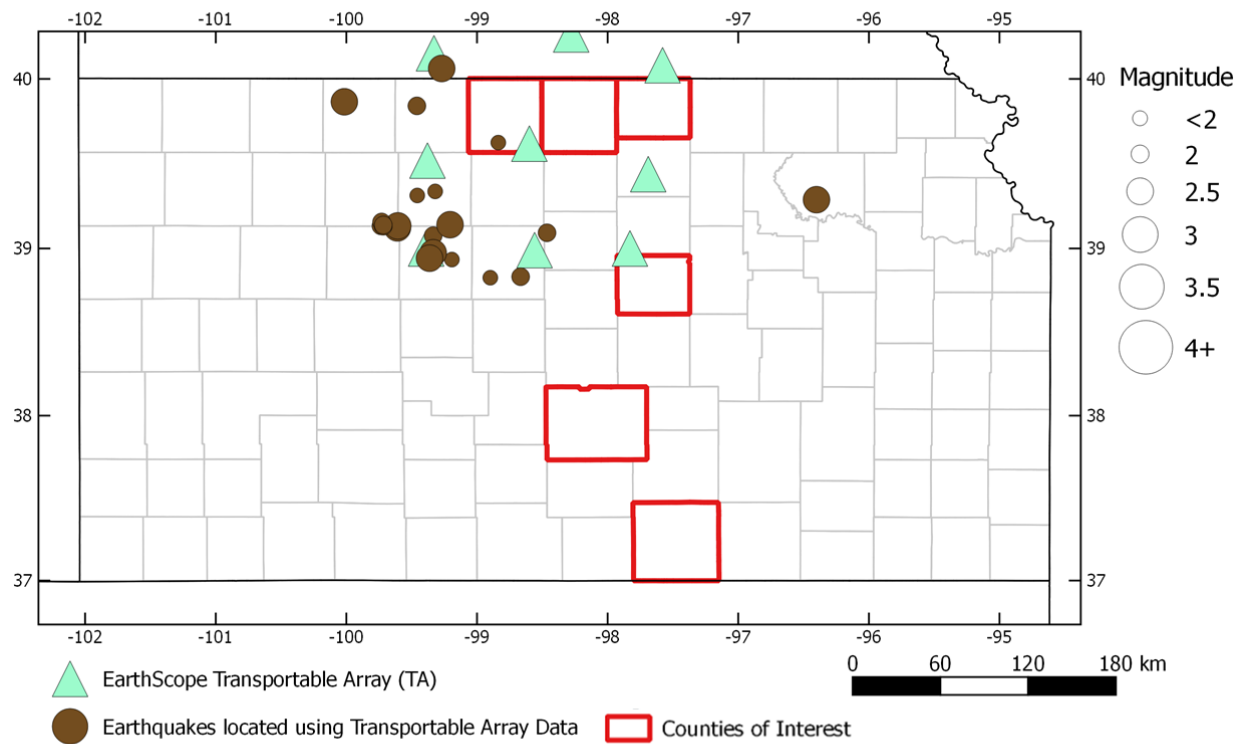


Figure 4-7 - Map of earthquakes in Kansas detected from the Earthscope Transportable Array data between May 2009 and March 2010. The nine stations shown are a sub-network of a larger array. Earthquakes located using this data can be found in Appendix A.

Chapter 5 – Focal Mechanisms and Inversion

Fault motion can be described by the orientation of the fault plane (strike and dip) and the direction of slip (rake). This is known as the focal mechanism. This motion, in our case, is considered to be double coupled motion resulting in two possible solutions of fault planes, or focal planes (Aki and Richards, 2009). Standard plots of double coupled sources and focal mechanisms are commonly referred to as beachball plots (Figure 5.1). There are three fault mechanisms: strike-slip, thrust and normal (Figure 5.2). These diagrams are an equal-area projection of the lower hemisphere of the focal sphere (Aki and Richards, 2009).

Focal mechanisms are calculated from waveform analysis of the P-Wave first motion polarity (or displacement) and amplitude ratios of the P-Wave and S-Wave (Snoke, 2003). The first motion polarity of the P-Wave retains the seismic character of the section of the focal sphere the raypath originating at the epicenter. These first motion displacements can then be mapped back to create the dilatational and compressional quadrants of the focal sphere. Amplitude ratios are more reliable than body wave amplitudes since the effects of geometric spreading, wave directivity and instrument cancel out (Havskov and Ottemoller, 2010). The focal mechanism depends on the source strength and fault orientation to characterize the source (Aki and Richards, 2009). The principal axes of the focal mechanism are the pressure-axis (P) located at the center of the dilatational quadrant and the tension-axis (T) located at the center of the compressional quadrant (Figure 5.1). The dilatational and compressional quadrants are separated by the nodal planes.

All P-Wave polarities were picked on the Z-component trace from each seismograph. P-Wave and S-Wave amplitude were automatically picked for each station within 200km of the epicenter using SeisAn's AUTORATIO (Ottemoller et al., 2016). The maximum amplitude was determined using a 1-10hz band-pass filter, 1.5 sec window around each p- and s-arrival pick and only on the horizontal

components for the S-Wave. The resulting horizontal component S-Wave to P-Wave amplitude ratio (SH/P) is used in two of the algorithms (HASH and FOCMEC) and adds constraints to the range of potential fault plane solutions (Hardebeck and Shearer, 2003). The highest P-Wave amplitudes occur near the P- and T-axis and the lowest near the nodal planes. This makes identifying P-Wave polarities for stations that resolve near the nodal planes difficult. At the nodal plane the P-Wave amplitude is zero making the SH/P ratio very large; and near the P- and T-axes very high, making the SH/P ratio very small (Kisslinger, 1980).

For the earthquakes analyzed in the Jewell County Area, Reno County and Salina County we used multiple fault plane solution algorithms to compute the focal mechanisms. This included PINV, FPFIT, HASH and FOCMEC (Ottemoller et al., 2016). PINV calculates the focal mechanisms by using only the P-Wave polarities (Suetsugu, 1998). This is the least rigorous calculation and only serves to corroborate other solutions. FPFIT is similar to PINV in that it only uses P-Wave polarities, but this algorithm assesses the fit of the solution based on a weighted sum error of the polarities and a station distribution ratio that describes how well the stations are spaced on the focal sphere (Raesenberg and Oppenheimer, 1985). HASH uses both P-Wave polarities and amplitude ratios and uses a grid search to find the solution with less than a given polarity error and amplitude error (Hardebeck and Shearer, 2002 and 2003). FOCMEC is the most user intensive algorithm. Similar to HASH, a user defined grid search is used to find solutions under a given polarity and amplitude error. All solutions are then displayed and the analyst selects the solution that best fits (Snoke et al., 1984 and 2003). PINV and FPFIT were used to corroborate solutions from HASH and FOCMEC that utilized wave field amplitude information. FOCMEC solutions were preferred over all other solutions.

Potential earthquake hazards can be determined from the optimal orientation of faults within a particular stress field. Faults optimally oriented with respect to the stress field are more likely to fail. The orientation of the stress field can be determined from the calculated focal mechanisms through various

inversion methods; the method used in this study was developed by Michael, 1984. This method assumes each earthquake is independent but representative of a constant stress field in the region (Angelier, 1979; Michael, 1984 and 1987). A best fit direction of slip is calculated using the vector normal to the fault plane; this is the slip vector (Gephart and Forsyth, 1984). In a double couple system with two fault planes, this method uses non-parametric bootstrap statistics to select one of the orientations (Michael, 1984). The solution is then calculated for the second fault plane and compared with the first. If the solution from the second calculation is congruent with the first, the first solution is kept. If the second solution improves the solution using a least squares criteria, then the second solution is kept. It is suggested at least 10 events be used for this inversion method (Ottemoller et al., 2016). The SLICK software is implemented within SeisAn (Michael, 1984). A catalog of fault planes are provided and the program generates the orientation and shape of the stress ellipsoid using the method above.

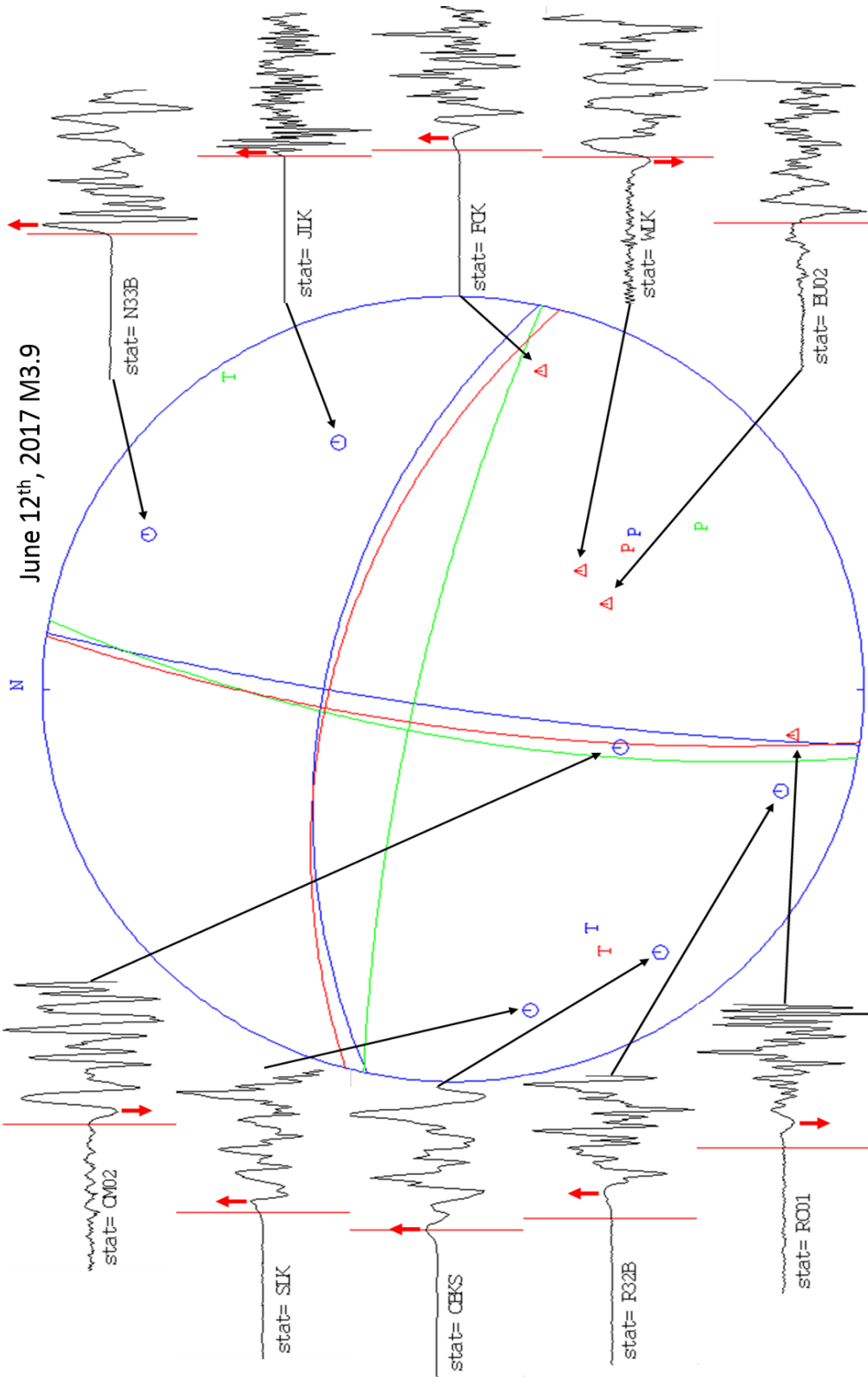


Figure 5-1 - Focal Sphere depicting the three focal mechanism solutions for the June 12th M3.9 earthquake in Jewell County. First motion plots can be seen on the left and right sides with red arrows indicated picked compression (up) and tension (down). On the focal sphere blue circles represent compression (P) and red triangles represent tension (T) used in 3 fault plane solution software packages used. Note that a discrepancy between the picked first motion and the calculated first motions are due to some algorithms allowing for first motion and amplitude errors. Red vertical line represents the picked P-Wave arrival for that station.

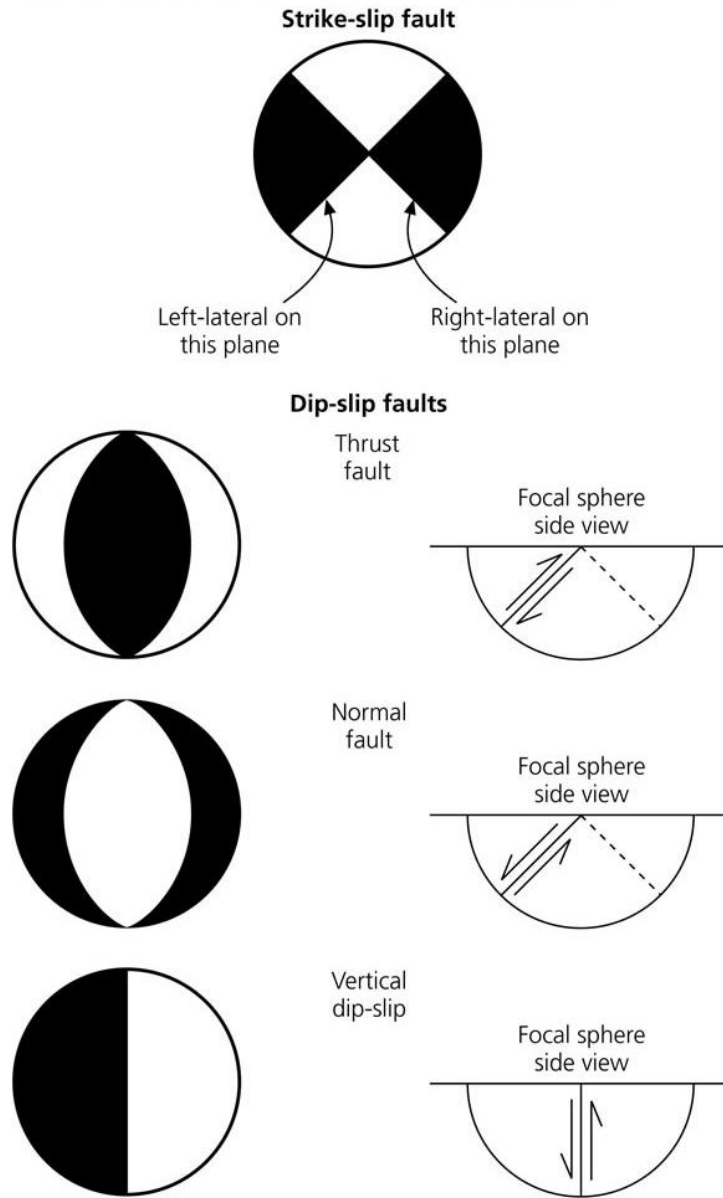


Figure 5-2 - Idealized beachball diagrams showing mapview and side view of basic fault mechanisms. (Stein and Wysession, 2003).

Chapter 6 – Stress Drop

Stress drop can be defined as the difference between the shear stress acting on a fault before and after rupture (Wu et al., 2018). Stress drop is not invariant across all geologic settings. It has been shown that stress drops of intraplate earthquakes are larger than interplate earthquakes (Kanamori and Anderson, 1975; Scholz et al., 1986). Induced seismicity near geothermal fields have been shown to have lower stress drop near the injection site and increase with distance (Goertz-Allman et al., 2011). Other studies have shown the possible decrease in stress drop can be a distinguishing characteristic in induced earthquakes – Reiter et al., 2012; Hough, 2014; Sun and Hartzell, 2014; Sumy et al., 2017. Boyd et al., 2017 reported that earthquakes in the eastern part of North America with $M_w 3$ have mainshock stress drops that range from 2.6 to 26MPa. These studies further show that mainshocks potentially related to wastewater disposal had stress drops that ranged from 0.6-5.6 MPa for the central US. Other studies have shown no discriminating qualities between induced and natural seismicity from stress drop (Clerc et al., 2016; Zhang et al., 2016).

According to the Theory of Self Similarity, stress drops are predicted to be constant for earthquakes of various sizes in the same tectonic environment (Figure 6.1). There are a few ways to calculate the stress drop from seismic waveforms (i.e. conventional method of corner frequency from seismic spectra or empirical Green's function (Hough, 1997)) and various source models that can be used (i.e. Brune, 1970 or Madariaga, 1976). In this paper we used the conventional method using a Brune, 1970 source model.

Brune stress drop ($\Delta\sigma$) can be measured from an earthquake's source properties. In modeling earthquake rupture, if the area of slip is circular the radius would be $r = \frac{2.34\beta}{2\pi f_c}$, where the corner frequency (f_c) is inversely proportional to the faulting duration (T_d) and β is the shear wave velocity. Equation 8.1 describes stress drop (Eshelby, 1957; Brune, 1970):

$$\Delta\sigma = \frac{7}{16} \frac{MO}{r^3} = \frac{7MO}{16} \left(\frac{2\pi f_c}{2.34\beta} \right)^3 \quad \text{Equation 8.1}$$

According to this model, MO is proportional to f_c^3 for a constant stress drop. To calculate these values SeisAn uses various assumptions about the geometrical spreading and anelastic attenuation in a multistep process to generate a theoretical displacement spectrum (Figure 6.2) as defined in Brune, 1970 (Ottemoller et al., 2016). These assumptions correct for small overestimates in the seismic moment calculated and are within reason given the low resolution of the shear wave velocity model. SeisAn will fit a Brune curve to the observed displacement spectra. The software uses an acceptable signal-to-noise range to find an acceptable frequency range and then fits by grid search; measured fits of 0.2 or better were kept. MO is calculated using these various properties and assumptions, such that

$$MO = 4\pi\rho V^3 \frac{10^{OM}}{G(r,h)*KK} \quad \text{Equation 8.2}$$

where ρ is density, V is the seismic wave velocity at the course, OM is the spectral flat level (blue line) on the attenuation corrected displacement spectrum (Figure 6.2), and $G(r,h)$ and KK are the geometric spreading and free surface effect and radiation pattern corrections (Ottemoller et al., 2016). From the spectral parameters source radius and stress drop can also be calculated using the following equations:

$$\text{Source Radius, } r = 0.37 \frac{V}{f_c} \quad \text{Equation 8.3}$$

$$\text{Stress Drop, } \Delta\sigma = 0.44 \frac{M_0}{r^3} \quad \text{Equation 8.4}$$

where V is the P- or S-velocity at the source for their respective spectra. Due to the highly variable source model and attenuation model, stress drop can have upwards of 30% uncertainty (Sonley and Abercrombie, 2006). Since all epicenter depths have been fixed to 5.0km many of the attenuation and velocity parameters are kept constant in the software parameter files.

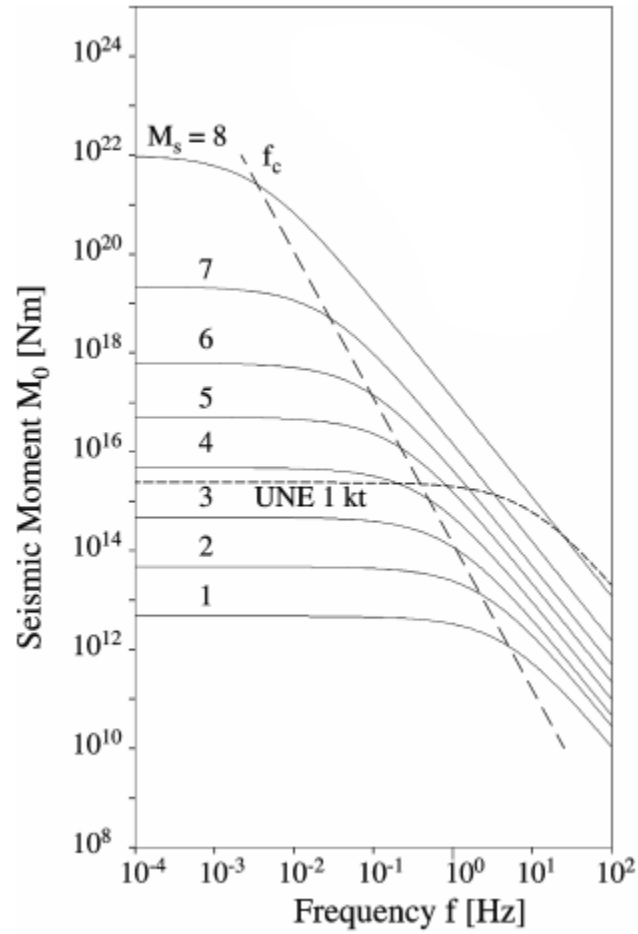


Figure 6-1 – Log frequency vs. log seismic moment graph of an Idealized source spectra characterized by the flat portion for frequencies smaller than the f_c . The amplitude for each flat portion ($f < f_c$) increases with seismic moment M_0 while the f_c decreases proportional to M_0^{-3} . (Modified from Stein and Wyssession, 2003)

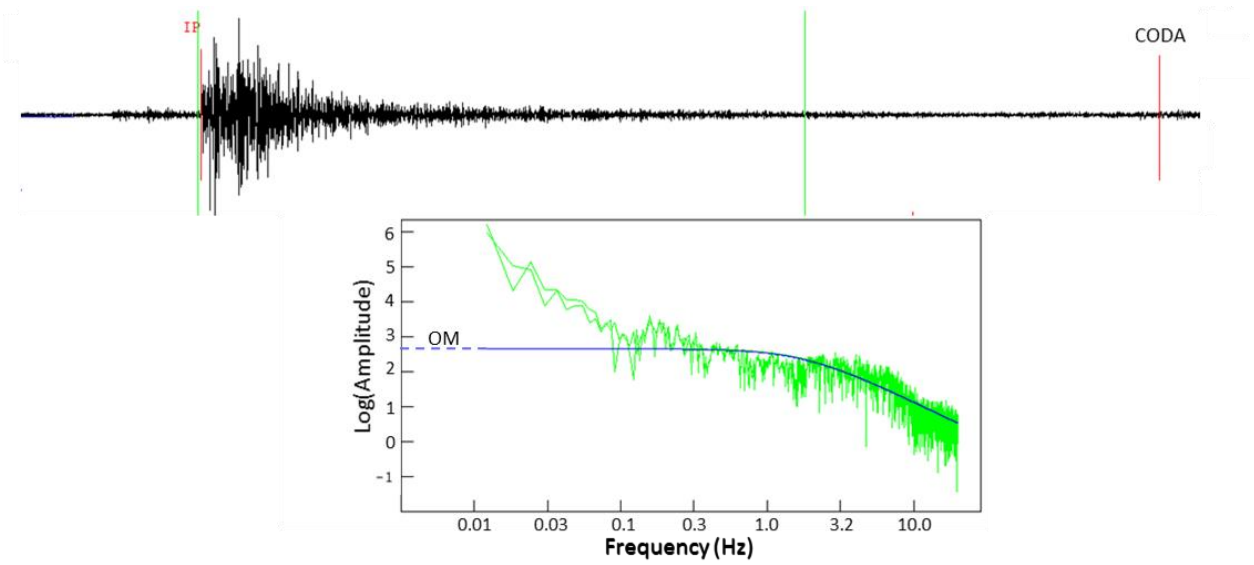


Figure 6-2 – Sample waveform used to determine source parameters (top) and an example of seismic source spectra (Bottom) of ground displacement (green) overlain by the calculated Brune Displacement Spectra (Blue).

Chapter 7 – Results and Conclusion

Section 7.1 – Results

A total of 95 focal mechanisms were calculated from seismic data using 34 different stations between September 2016 and November 2018 (Figures 7.1, 7.2, 7.3 and Appendix B). The regional geology suggests that both strike-slip and normal faulting are highly likely in this region (Jewett, 1951; Merriam, 1963; Hildebrandt, 1988; Barr, 1995; McBee, 2003; Gerhard, 2004). A majority of the focal mechanisms calculated support this claim. Despite having over 60 seismic stations concurrently recording in the state, azimuthal coverage is a concern when assessing the focal mechanism solutions. Some solutions have stations in only three of the focal sphere quadrants, making it difficult to constrain the solution.

The misfit, β , is the average difference between the slip vector calculated from the fault plane solution and the slip vector calculated from the new stress tensor (Michael, 1984). Large β values suggest poorly constrained stress tensor. The results of running the inversion on the Jewell County Area, Saline County, and Reno County area clusters (Figure 7.4) have a wide range of solutions. Initially running the inversion with all 50 focal mechanisms in the Jewell County Area resulted very high misfit and standard deviation ($>50^\circ$ and $>55^\circ$, respectively), very similar to Saline County results (Table 5.1). Removing all events within the Jewell County Area with less than M3.0 and two events with unusually high misfit the resulting stress orientation misfit was 21.9° , comparable to Reno County. Jewell County's results drastically improved after lower magnitude and poorly confined events were removed.

Reno County has the best misfit with 16.8° and a standard deviation of 12.9° with a maximum horizontal stress of 47.1° . The maximum horizontal stress of the Jewell County Area was -48.7° . The results of the Saline County area show a large misfit suggest that better and closer station coverage may

help in constraining the stress tensor. Applying the same magnitude threshold for the Jewell County Area to the Saline County area inversion did not yield better misfit.

81 earthquakes from the three main study areas (Appendix C) had sufficient data quality to calculate stress drop (Figure 7.5). We find that the stress drops for the Jewell County Area have highest range of values, 0.2-4.0MPa (Figure 7.6), of the three study areas. The range of stress drop values for Reno County and Saline County areas are 0.1-1.6MPa (Figure 7.7) and 0.4-2.3MPa (Figure 7.8), respectively. Stress drop values this low when compared to values reported by Boyd et al. (2017) may be one indication that these events are induced. Nine additional seismic events were analyzed in the Milan Event (Figure 7.9) and compared with stress drop reported by Choy et al., 2016. Many of these clusters are in close proximity to UIC Class I and Class II wells (Figure 7.10).

Although stress drop values in the Jewell County Area are consistent with the other areas of investigation, there is only one seismic station within 100km of the central cluster. The high variability in stress drop depends on the source model, using different source models could better constrain the calculated stress drop. With such low station coverage for many of these events the likely greatest source of uncertainty is the source geometry. Source geometry, rupture directivity, and rupture speeds have all been found to influence the stress drop up to a factor of eight (Kaneko and Shearer, 2015).

Section 7.2 - Discussion

From 1967 to 2000, the Central United States (CUS) experienced on average 21 magnitude (M) 3 or larger earthquakes per year (Ellsworth, 2013); since then we've seen an unusual and dramatic increase in anthropogenic/induced seismicity (Kim, 2013; Keranen et al., 2013 and 2014; Rubenstein 2014 and 2018). A new catalog of earthquakes in areas of Kansas not expected to be influenced by induced seismicity resulting from high volume injection wells shows new seismic clusters developing away from areas historically producing earthquakes.

Previous studies in Kansas focusing on the abnormal seismic activity have included pore pressure diffusion and far-field effects (Peterie et al., 2017), rupture process and geometry of particular clusters (Choy et al., 2016), stress state (Alt and Zoback, 2017; Schwab et al., 2017) and shear wave anisotropy (Nolte, 2018). These studies all target the south-central portion of the state nearest the most seismically active areas. Station locations shows a predominant focus on monitoring the southern portion of the state, with new clusters developing to the north in areas with minimal historical earthquakes and some with no historical earthquakes. Discriminating natural from induced earthquakes is very difficult when the historical average for Kansas is one M3 or greater every one to two years. This rate contrasted with the current rate makes it hard to identify natural events occurring in today's environment. Processing the Earthscope TA data has shown that in the current areas of developing seismicity there is little to no historic activity. Although this claim is made from less than two years worth of data, the alternative historical interpretation utilizes data acquired from a network of 2 stations within the state. The TA dataset utilizes over 45 stations to monitor seismicity and provides a better estimate of historical seismicity rates. This is an important distinction to make when the state lacks sufficient seismic monitoring network for 22 years to claim a historical rate of seismicity.

The b-value for the catalog used in this study was 1.21 with a magnitude of completeness of 1.8 for the network of stations, but is likely variable across the state with higher network sensitivity in the south than in the north. This is an increase from the historical b-value of 1.09 calculated from the KSNE network from 1977 to 1989. The current monitoring of earthquakes across the state has revealed this is an increase in b-values compared to the regional b-value of 1.06 (Rubenstein et al., 2018). Rubenstein (2018) has shown an increase in b-value across the two-county area of Harper and Sumner counties; in 2016 the area had a b-value of 1.26. B-value is inversely proportion to differential stress and could be a side-effect of increased pore pressures resulting in more smaller events relative to larger ones (Bachmann et al., 2012, Scholz, 1968 and 1972). Increases in pore pressure decreases the shear stress

needed to result in failure, this occurs when the shear stress exceeds the critical stress (Wyss, 1973). This has been observed both in a laboratory setting and from earthquake databases (Amitrano, 2003 and Schorlemmer et al., 2005). Scholz (1968) also showed that where b-values were highest failure was likely due to sliding along pre-existing fractures. The observed increase in b-value from normal tectonic regimes is one indicator that earthquakes in Kansas are occurring along existing fractures and in larger numbers of smaller magnitudes mainly due to increased pore pressures. Continued monitoring variations in b-value for different parts of the state can help to indicate areas of changing seismicity.

Predominately strike-slip and normal faulting are common in this area. Thrust faulting is rare, possibly nonexistent. Almost all of the focal mechanisms from the three study areas are either strike-slip or normal faulting. The maximum stress calculated for Reno County was 47.1° which is consistent with other stress studies further south (Zoback and Zoback 1980; Dart, 1990; Alt and Zoback, 2016; Schwab et al., 2017). The Jewell County Area maximum horizontal stress calculation was moderately constrained at -48.7° with a misfit of 21.9° despite poor azimuthal coverage and no data for an entire quadrant of the focal sphere. Limiting the magnitude of events used in the inversion drastically improved the solution. Saline County had a principle stress orientation of -166.7° , but due to high misfit, 60.2° , results lacked sufficient certainty to be reliable. A magnitude threshold similar to the Jewell County data set was used, but misfit was still outside the bounds for a reliable solution. It may be feasible with better station coverage or inversion method to calculate a better stress orientation solution. 1-3 seismic stations on the northeast side of the trend would provide better azimuthal coverage of the focal sphere. A more complete azimuthal coverage of the focal sphere for the Jewell County Area and Saline County would lead to better constrained focal mechanisms and inversion.

From Alt and Zoback (2017) the stress orientation from wellbore and seismic data was calculated to be approximately N85E in south-central Kansas. This orientation matches well with the stress orientation calculated for Reno County and likely implies that the same basement structure that

influences the stress field in Oklahoma is the same as far north as Reno County. Although, Reno County is just south of the confluence of two large structures, the Central Kansas Uplift and the NE-SW trending MGA (Figure 2.5), the stress orientation north of Reno County may rotate.

The stress field in Jewell County is rotated over 90° from the stress field measured in Reno County. This orientation is also inline with many of the NW-SE trending magnetic lineations proposed by Yarger (1983). These lineations are thought to be associated with pre-rift structural anomalies (Yarger, 1983). Basement structure associated with pre-rift structures along with the influence of the Central Kansas Uplift could result in the rotated stress orientation we observe between Reno and Jewell counties. The observed rotation in the stress field would indicate faults of various orientations not historically predicted to be optimally oriented may in fact be preferentially oriented and more likely to slip. Focal mechanisms in Saline County would allow for more insight into how the stress field changes from south to north. Seismic events on the CKU and in Saline County near the MGA may provide a contrast of stress orientations that could explain and confirm the rotation of the stress field between Reno and Jewell County.

Yarger, 1983 interpreted various magnetic lineations (Figure 2.4), generally trending NW-SE and NE-SW, that line up well with seismic trends (Figure 6.4). Faults associated with these lineations would trend similarly. For the Jewell County Area, the principle horizontal stress is in the same direction at the NW-SE magnetic lineation. From lack of earthquakes along these NE-SW trends it is reasonable to interpret that faults associated with the NE-SW trending lineations must not be optimally oriented for slip with respect to the calculated stress field. Pressure increases on the Central Kansas Uplift from disposal wells (Figure 2.2) could preferentially diffuse NE via these sub-critical faults. Once the increased pressure field intersected the critically stressed NW trend faults associated with the lineations and optimally oriented to the larger stress field, slip would occur. Far-field pressure diffusion as far as 90km

away, if possible, would explain drastic increases in seismicity in a seismically quiescent county that has zero oil or gas production and no disposal wells since 2000.

Saline County has similarly NE-SW trending magnetic lineations (Figure 5.4). These lineations trend similar to the NE-SW trending MGA and likely associated with faulting in Keweenaw time (Yarger, 1983). The lack of earthquake seismic data, well data, and poorly constrained stress orientation make interpreting the cause of the recent dramatic increase in earthquakes along this trend difficult. A majority of the focal mechanisms in this area suggest normal faulting striking parallel to the lineations. If these are correct then it would suggest a stress field similar to Reno County and not the Jewell County Area. A better understand of the stress field in other parts of the state as more data becomes available could lead to a better interpretation of why the stress field changes across the state.

Although stress drop has been suggested as a discriminating factor between induced and natural events, the stress drop analysis calculated for these three areas does not reveal a separation in stress drop between the two mechanisms. Induced and natural earthquakes should have separate trends when plotting the seismic moment versus corner frequency (Figure 7.5). There is no indication of two separate trends within this data set and suggests that nearly all these events are induced or natural. The stress drops found in Kansas are of similar magnitude as found by Boyd (2018) and are much smaller, up to an order of magnitude, than the stress drop range for tectonic earthquakes in Central and Eastern North America found by Atkinson and Boor (2006). This would suggest that, although we don't have two trends to separate natural from induced, the trend we do observe suggests that nearly all these events are induced.

It still stands that the complex geology of the crystalline basement and its hydraulic interaction with the injection target Arbuckle Group, make it difficult to determine precisely the far-field effects of

wastewater disposal. Lack of well data in certain areas make it difficult to model pressure changes between the areas of high injection and high seismicity.

Section 7.3 - Conclusion

High b-value, proper stress orientation and low stress drop are three factors that support the suggestions that a majority of events since 2014 are induced as a result of changes in pore pressure. On November 14th, 2014 Kansas experienced its largest recorded earthquake to date (M_w 4.9) near Milan, KS. Since then, a comprehensive network of seismic stations has been installed across the states to investigate mechanisms responsible for the dramatic increase in seismicity. The three areas presented in this paper vary in location uncertainty, station coverage, proximity to high injection areas and an understanding of the regional stress field. As a result of our analysis increased b-value, spatial and temporal changes in seismicity and low stress drop discriminate induced events from natural events.

More recent data, predominately from the KGS with some additional stations from the USGS and other projects in the state now make up a catalog of earthquakes with over 12,000 events since 2014. This catalog has a M_c of 1.3 and a b-value of 1.21. An analysis of seismic data by the EarthScope Transportable Array acquired prior to the 2012 increase in injection activity suggests that the northernmost study area was seismically quiescent over the 1-2 year recording period but now has experienced two of Kansas' largest earthquakes to date. Using this catalog developed from the KGS network and supporting stations, 95 events were used to determine the focal mechanisms and stress orientations throughout the central part of the state. From this inversion, the maximum horizontal stress for Reno County was 47.1° ; this orientation is within reason when compared to other studies from northern Oklahoma and south-central Kansas. The stress orientation of the Jewell County Area is -48.7° , nearly a 90° rotation. This change in orientation may be related to the MGA and Central Kansas Uplift

and indicate the optimal orientation for faults is different than previously determined in the southern portion of the state.

From the same catalog 90 events were used to calculate Brune stress drop from the three study areas and Milan event. Stress drop calculations in this study near Milan, KS matched well with those calculated in other studies. The median stress drop for Milan, Reno County, Saline County, and Jewell County Area were 1.7MPa, 0.8MPa, 1.7MPa and 1.2 MPa respectively. These values match well with other studies within the Central United States (CUS) and suggest these clusters of earthquakes are related to injection activities despite the lack of local high-volume injection. In particular, the nearest wastewater disposal wells in proximity to the seismicity increases in the Jewell County Area are 90km away on the Central Kansas Uplift. Stress orientation, focal mechanisms and stress drop just a few of the methods and indicators that may help discriminate natural from induced earthquakes in the future.

The methods presented in this study show that discriminating earthquakes as natural or induced is very challenging and that no single method can solve this. High b-value and low stress drop compared to regional studies have indicated that nearly all the new seismicity in Kansas is induced. In addition to these findings, focal mechanism inversion indicates that the stress field changes drastically from south to north within the state. With better station coverage near the norther developing clusters of seismicity better methods using spectral characteristics could be used to better explore the problem of discriminating earthquakes.

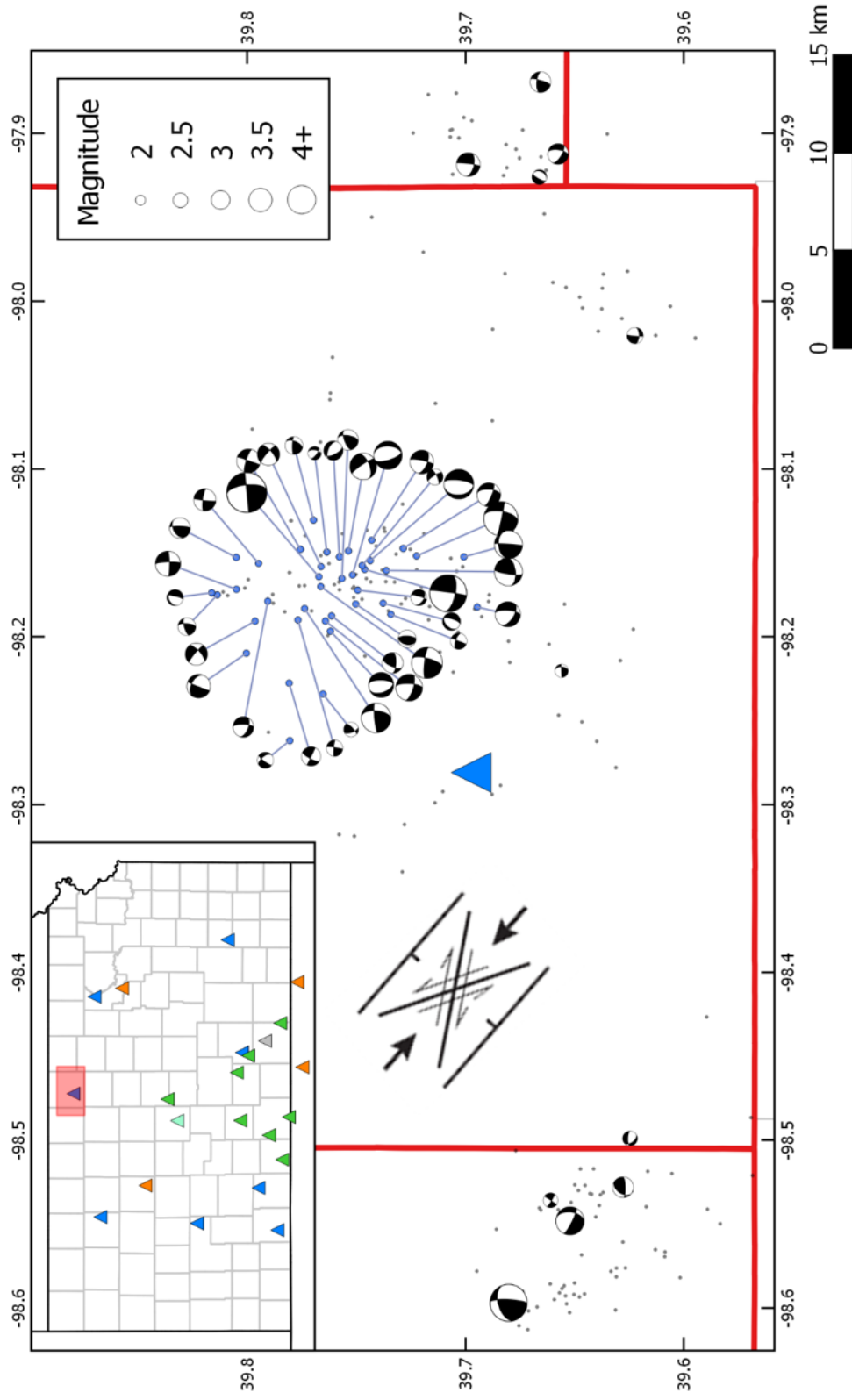


Figure 7-1 - Beachball diagram of all earthquakes in Smith, Jewell and Republic counties. 18 events had adequate misfit, station coverage, signal-to-noise and location to invert for stress orientation. Grey dots are the epicenters of earthquakes not used in the focal mechanism analysis. Inset map of Kansas shows stations from across the state. Diagram below the inset map illustrates preferred strike-slip and normal fault planes for a maximum horizontal stress of -48.7° .

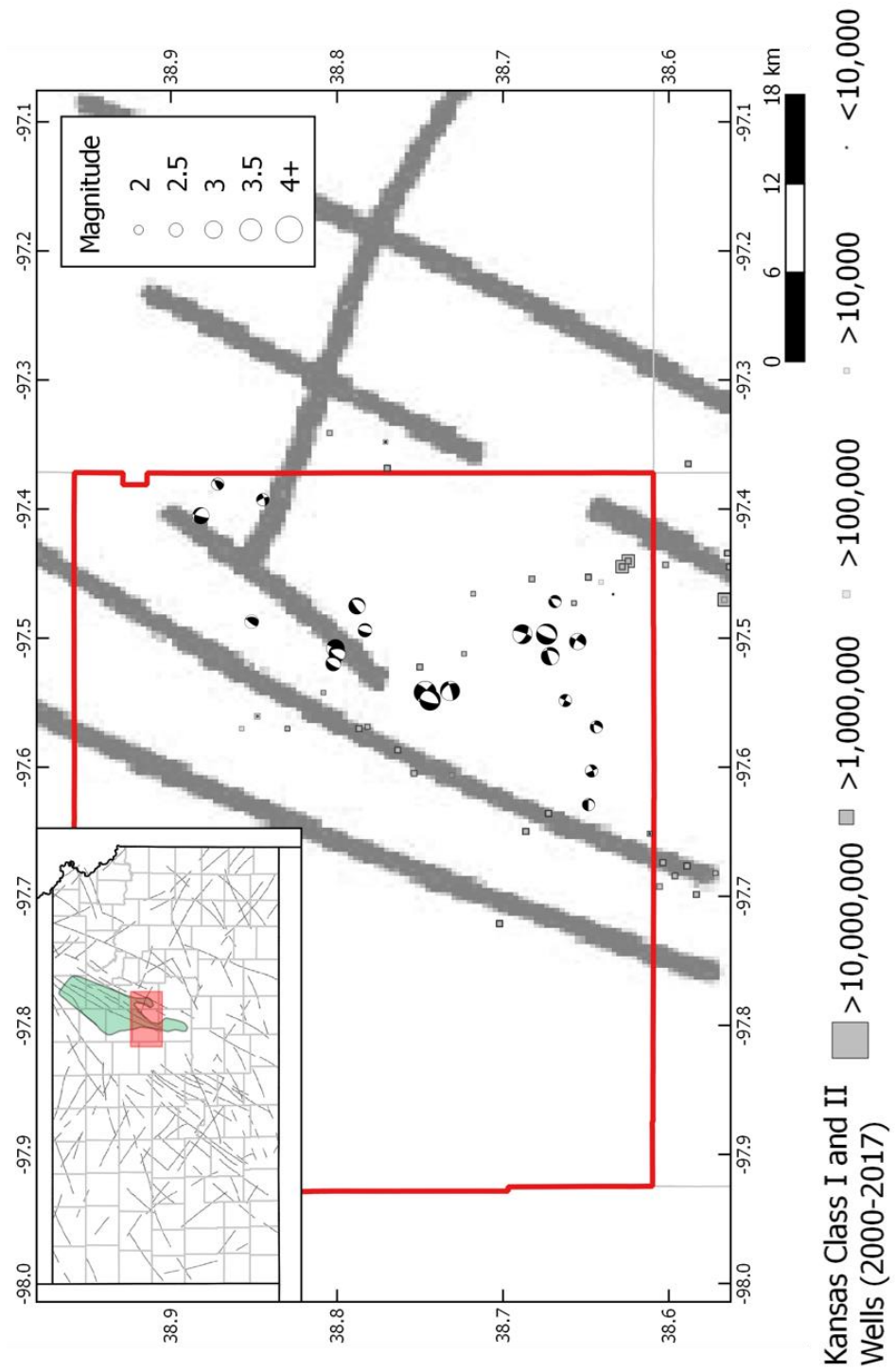


Figure 7-2 - Beachball diagram of all earthquakes in Saline County that were used to determine the stress field. 24 events had adequate station coverage, signal to noise and location. Thick grey lines are magnetic lineations interpreted from Aeromag data; Yarger, 1983. Inset map shows the full magnetic lineation interpretation from Yarger, 1983 and includes an outline of MGA.

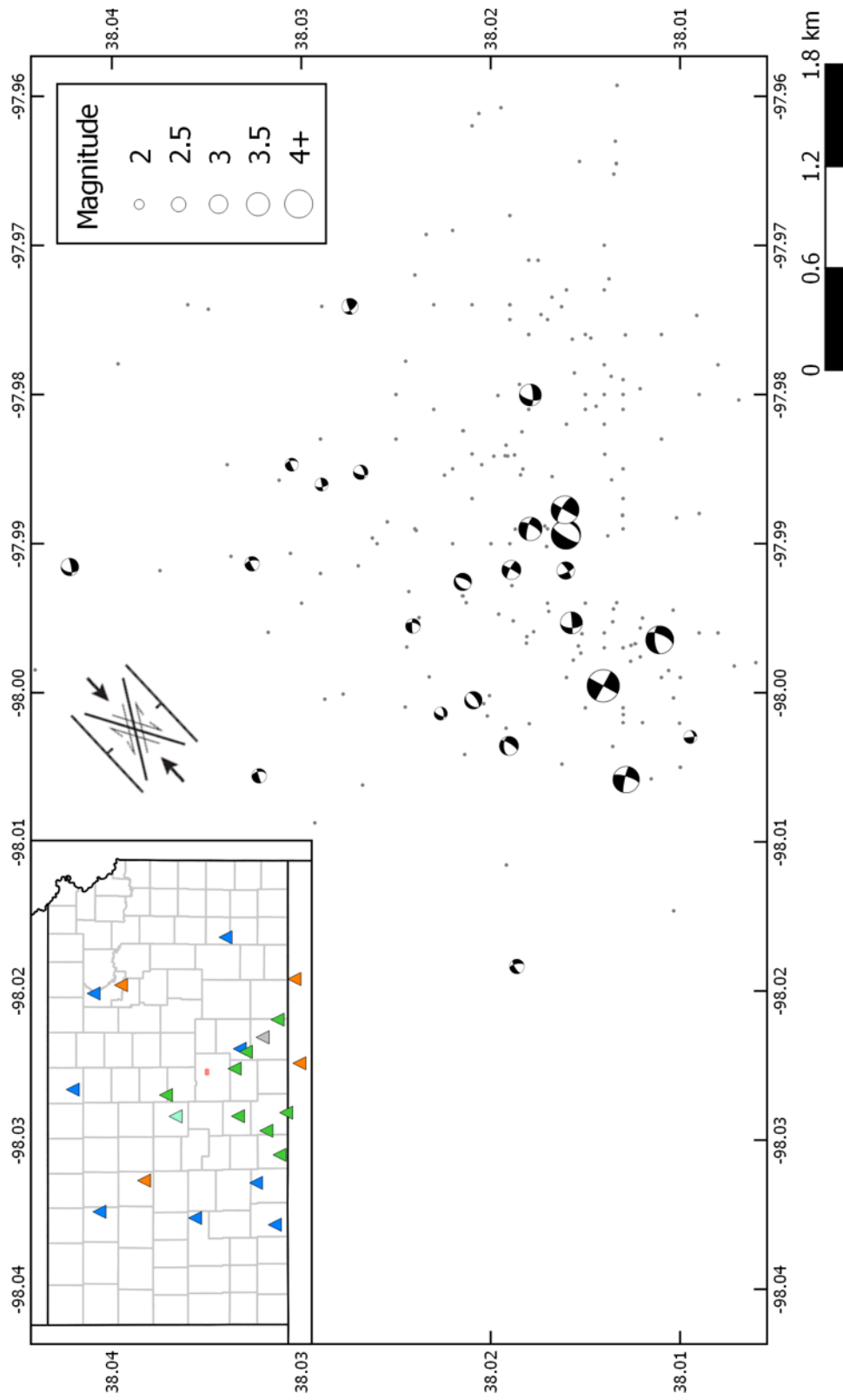


Figure 7-3 - Beachball diagram of all earthquakes in Reno County that were used to determine the stress field; 21 events in total. Grey dots are the epicenters of earthquakes not used in the focal mechanism analysis. Inset map of Kansas shows stations from across the state providing excellent azimuthal coverage. Diagram to the right of the inset map illustrates preferred strike-slip and normal fault planes for a maximum horizontal stress of 47.1° .

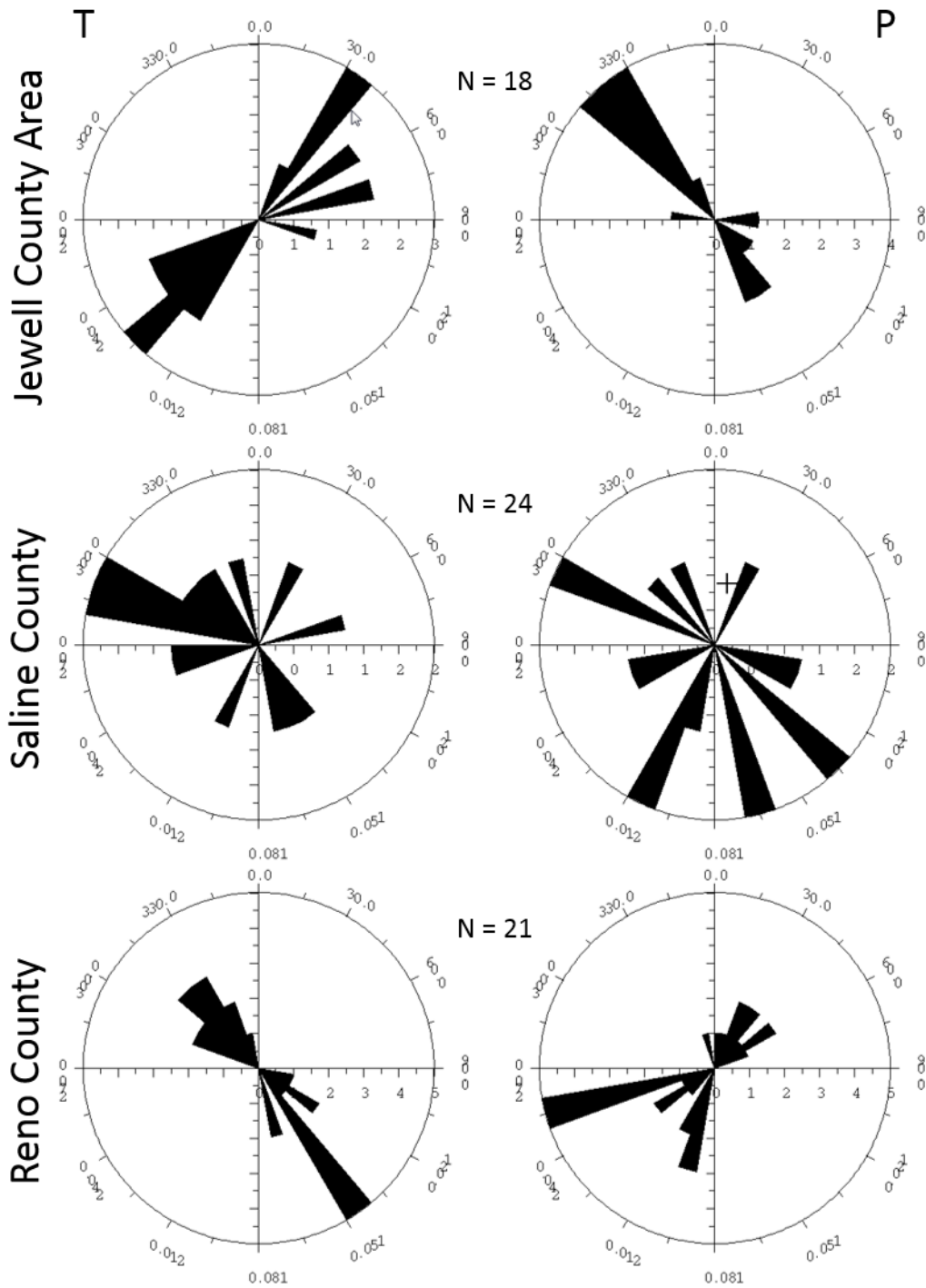


Figure 7-4 – Rose diagram depicting the orientation of the P-axis orientations (Right) and the T-axis orientations (Left) for each of the 3 areas. Michael, 1984 focal mechanisms inversion method was used in conjunction with SeisAn.

Area	n	Principle Horizontal Stress (°)	Average Misfit, β (°)	Misfit Standard Deviation (°)
Jewell	18	-48.7	21.9	21.6
Saline	24	-166.7	60.2	52.3
Reno	21	47.1	16.8	12.9

Table 7.1 - Results of the focal mechanism inversion showing the principle horizontal stress orientation and the statistical misfit from the data.

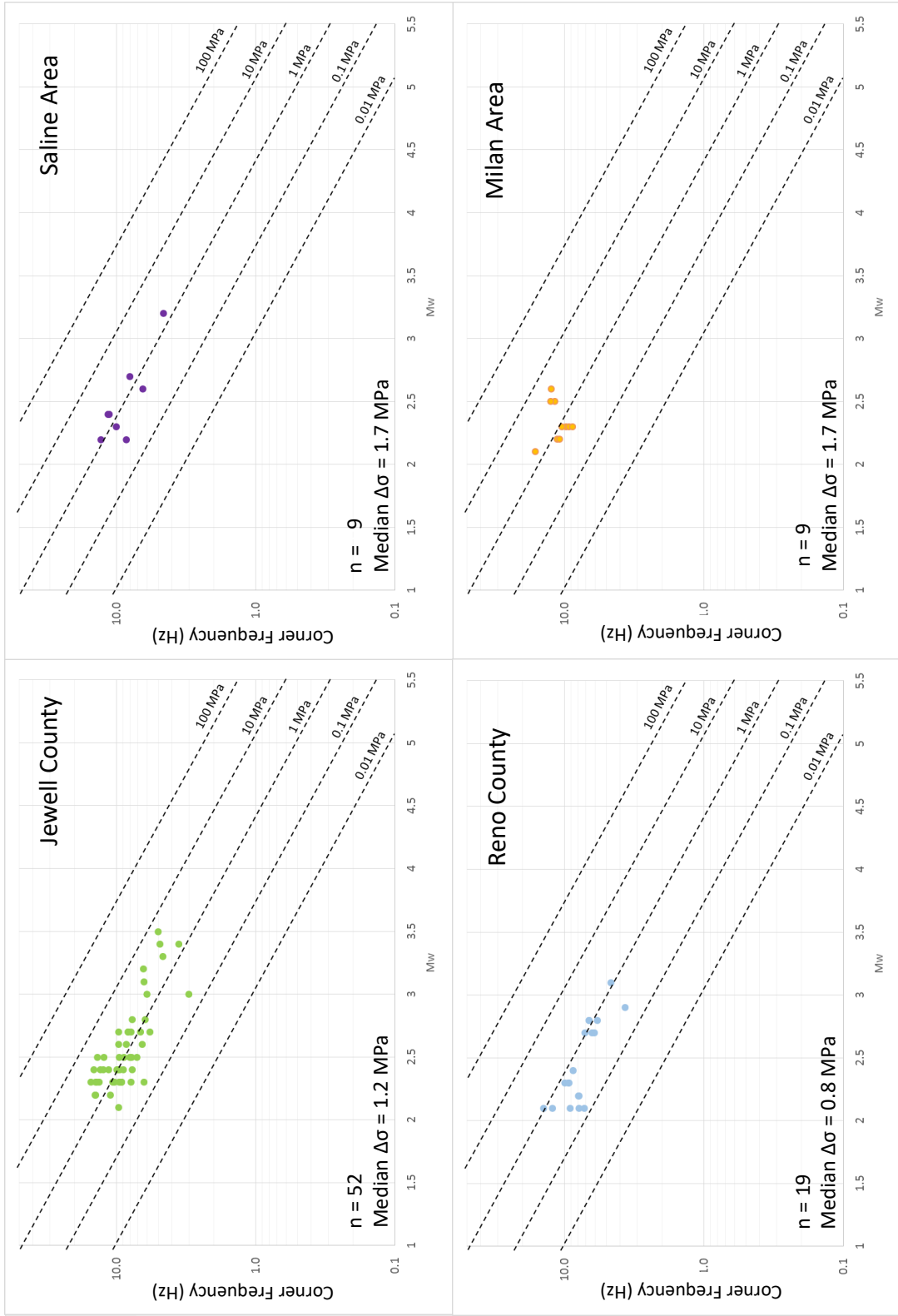


Figure 7-5 - Moment Magnitude vs. Corner Frequency plot of study areas with Brune constant stress drop lines indicated. A more detailed stress analysis of the Milan earthquake sequence can be found in Choy et al., 2016 where similar stress drops were calculated.

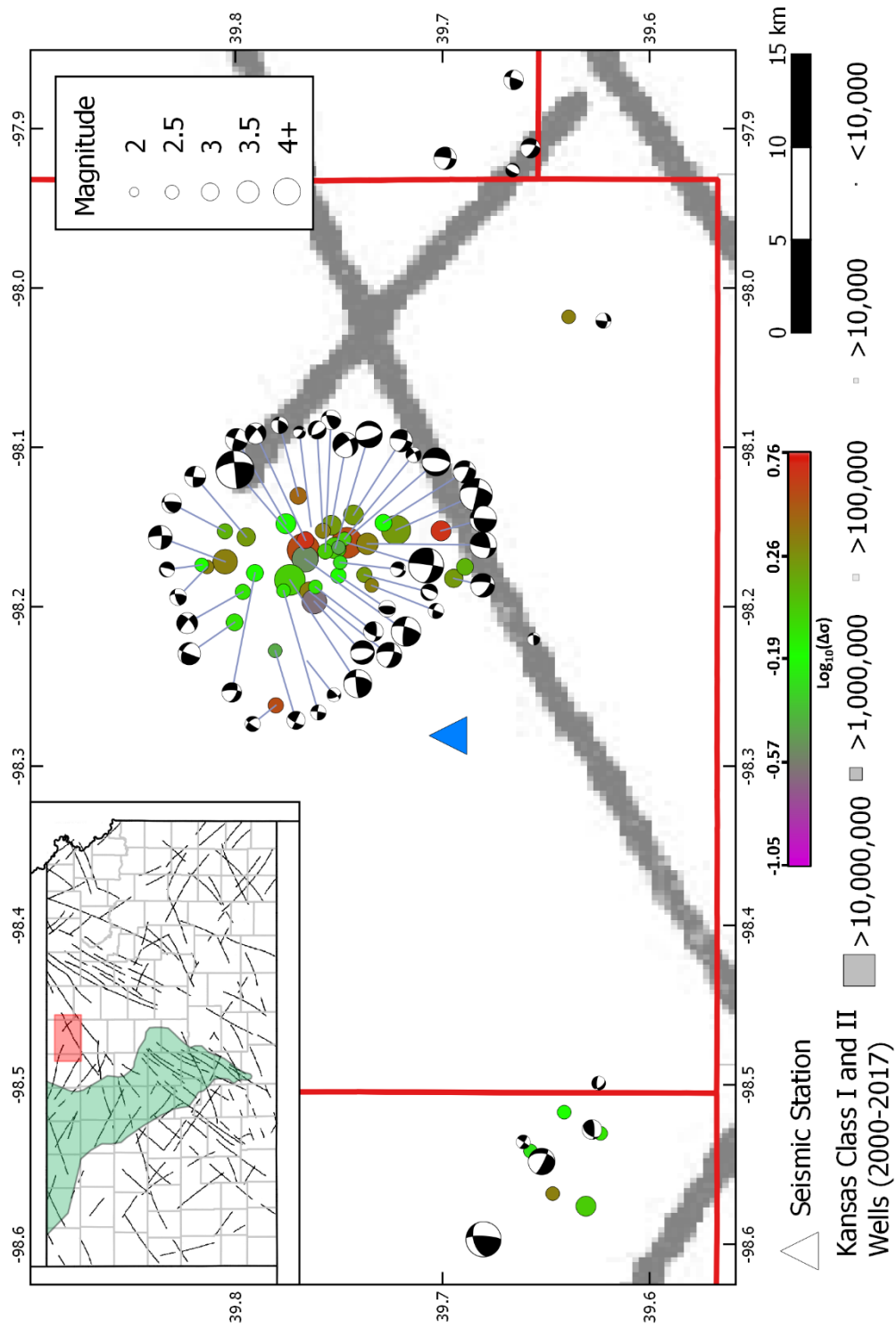


Figure 7-6 - Log_{10} of stress drop in Jewell County overlain by focal mechanisms calculated in Chapter 8. Size (magnitude) of stress points are M_w and size of beachballs are M_i . Thick grey lines are magnetic lineations interpreted from Aeromag data; Yarger, 1983. Diagram below the inset map illustrates preferred strike-slip and normal fault planes for a maximum horizontal stress of -48.7° . Inset map shows all magnetic lineations interpreted from magnetic data from Yarger, 1983. Green polygon outlines the Central Kansas Uplift, a popular area for wastewater disposal.

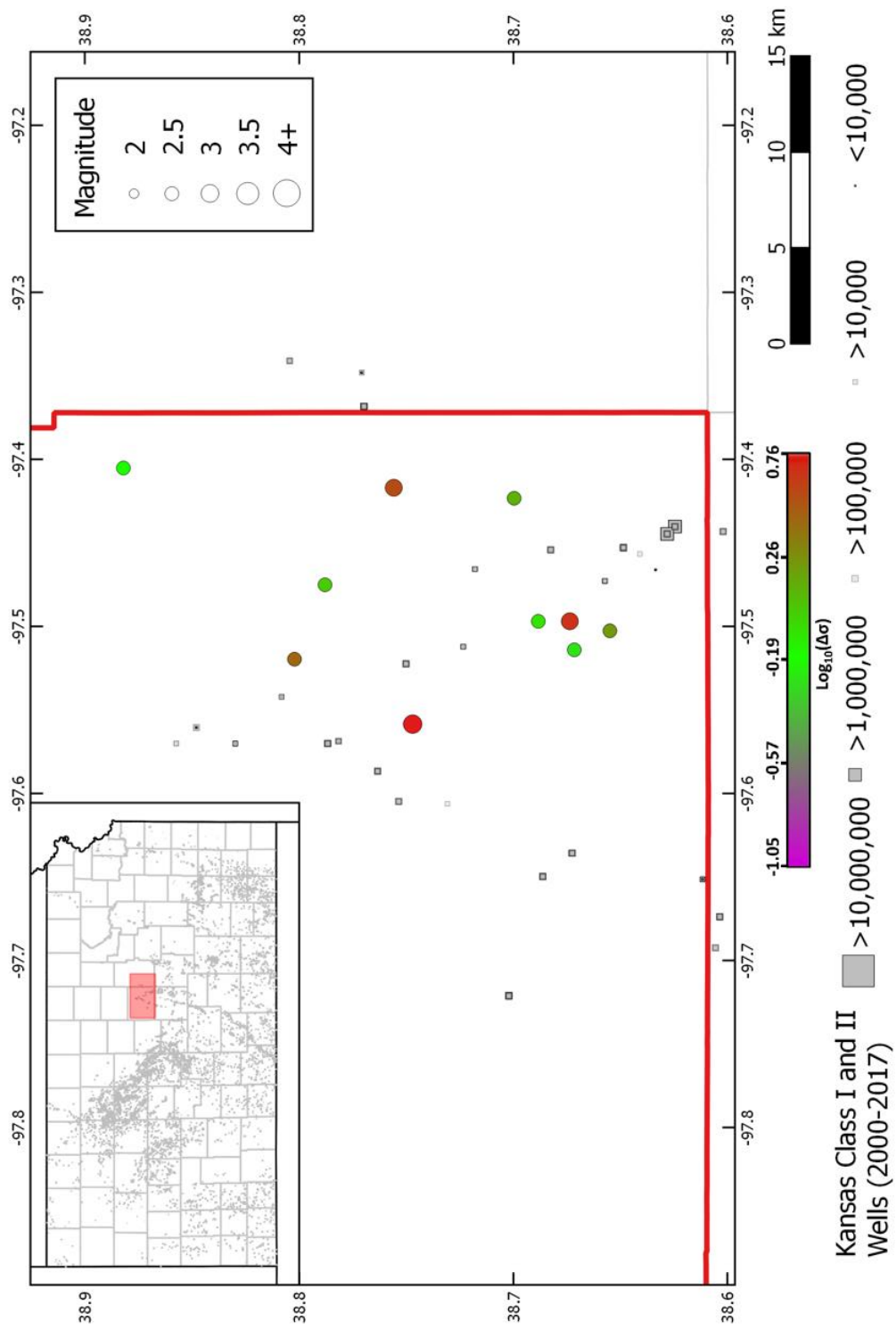


Figure 7-7 - Map of Saline County stress drops with surrounding injection wells sized to annual injection volume. Inset map shows all UJA Class I and II injection wells in Kansas between 2000 and 2017.

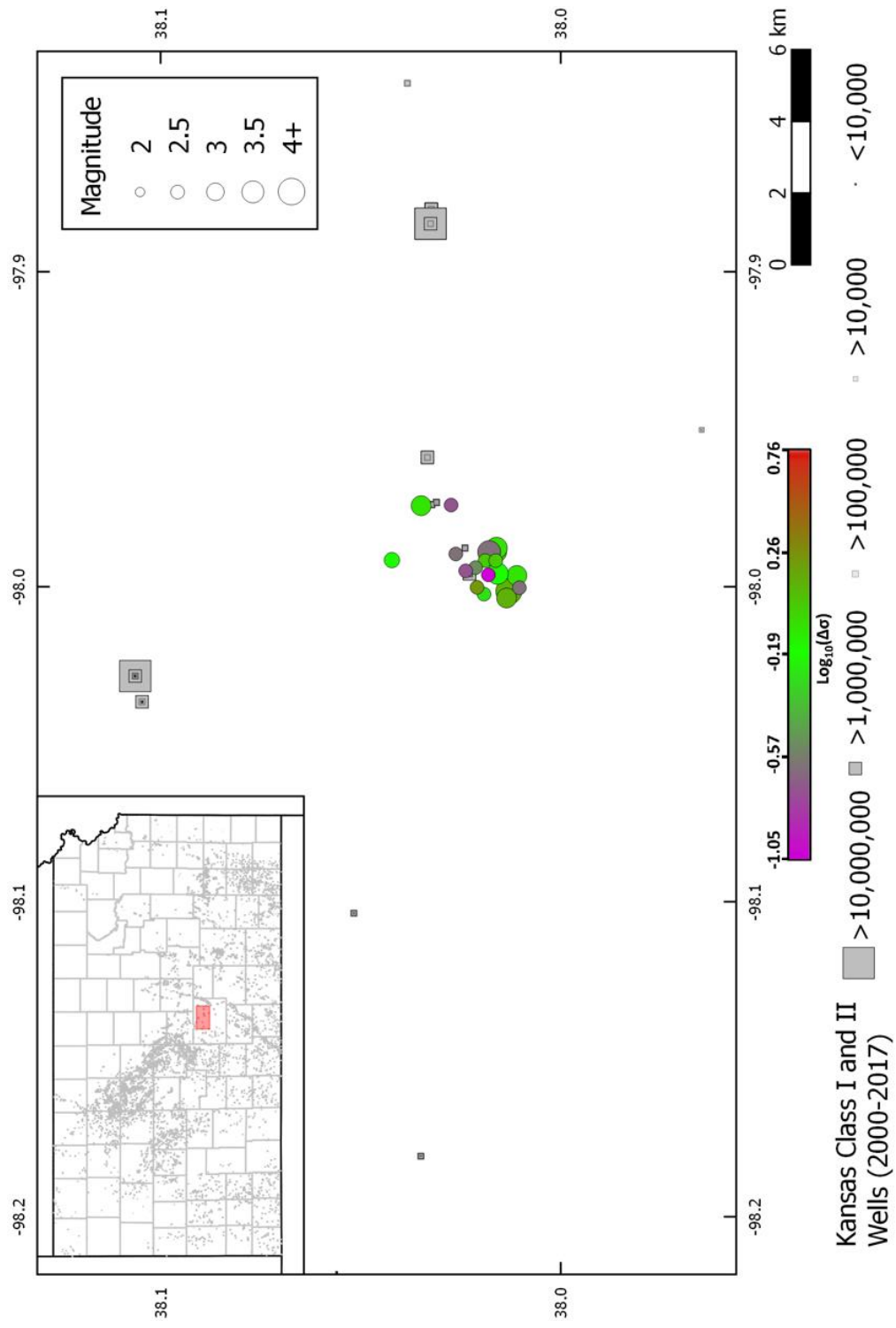


Figure 7-8 - Map of Reno County Log_{10} stress drops with surrounding injection wells sized to annual injection volume. Inset map shows all UJA Class I and II injection wells in Kansas between 2000 and 2017.

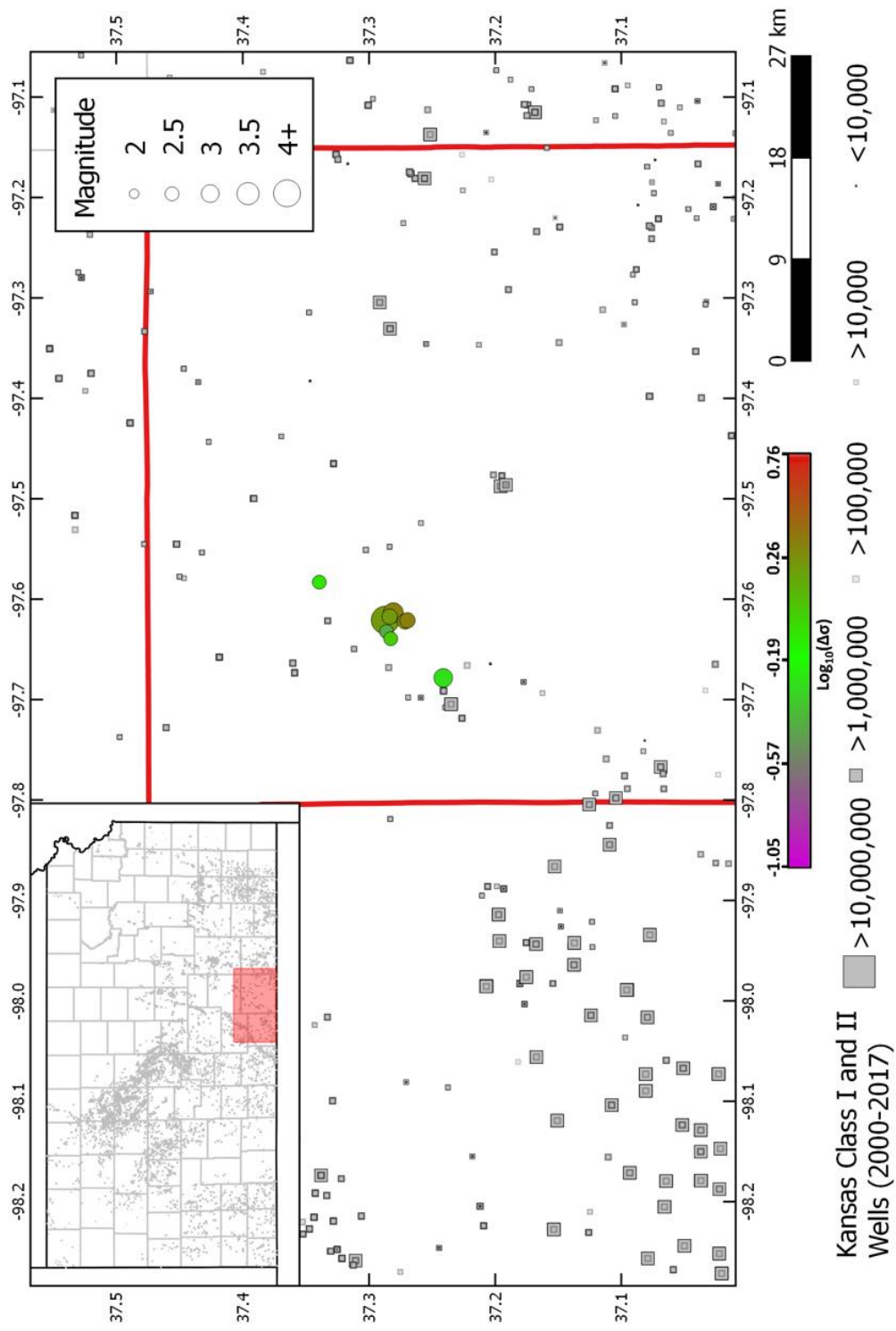


Figure 7-9 - Map of Milan area Log₁₀ stress drops with surrounding injection wells sized to annual injection volume. Inset map shows all UJA Class I and II injection wells in Kansas between 2000 and 2017. Stress drop results align well with previous studies from Choy et al., 2016.

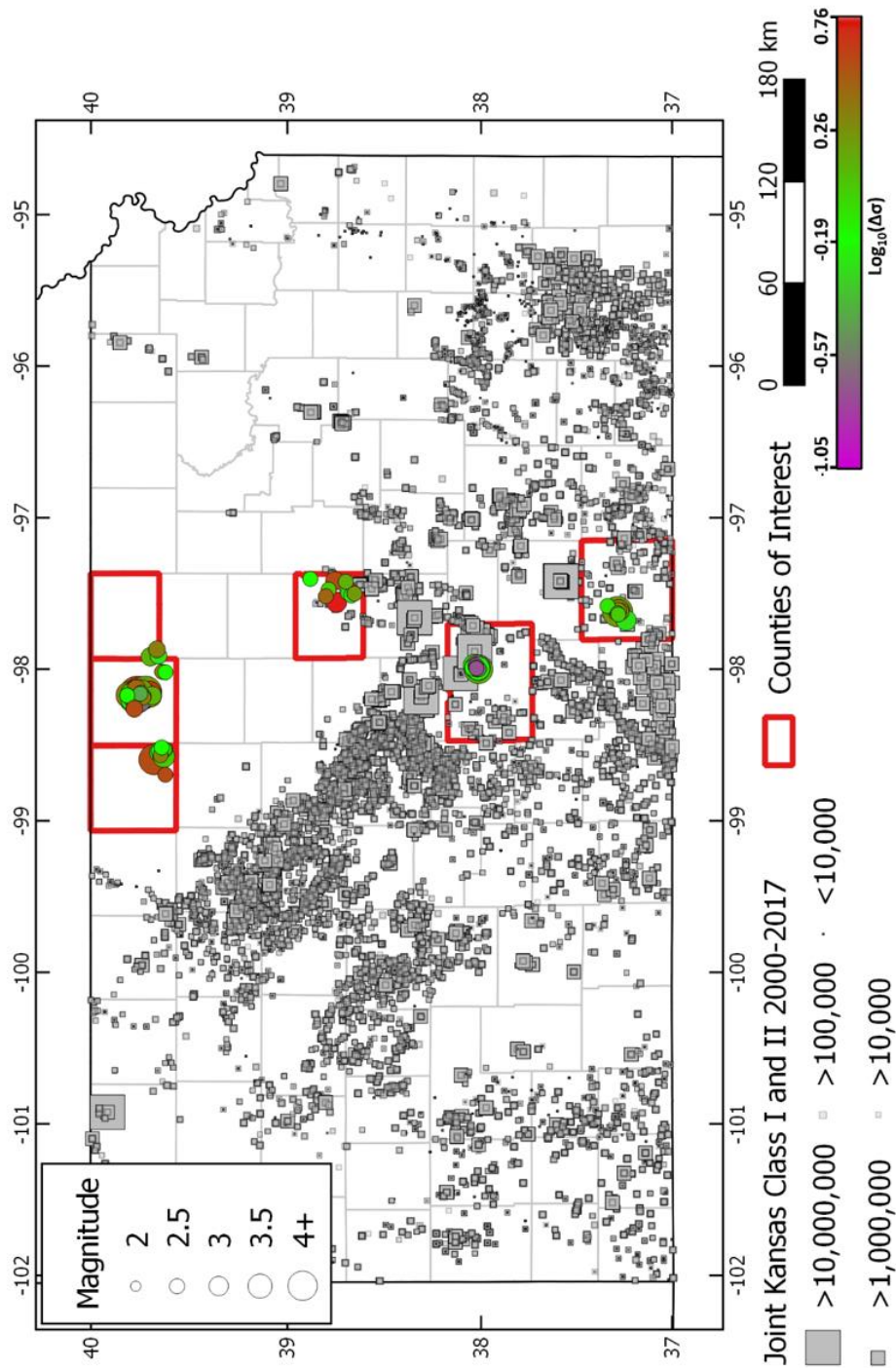


Figure 7-10 - Regional map of Kansas showing all four areas with stress drop in relation to local injection wells.

References

- Ake, J. (2005). Deep-Injection and Closely Monitored Induced Seismicity at Paradox Valley, Colorado. *Bulletin of the Seismological Society of America*, 95(2), 664–683. <https://doi.org/10.1785/0120040072>
- Aki, K., & Chouet, B. (1975). Origin of coda waves: source, attenuation, and scattering effects. *Journal of Geophysical Research*, 80(23), 3322–3342.
- Aki, K., & Richards, P. G. (2002). *Quantitative Seismology*.
- Alt, R. C., & Zoback, M. D. (2017). In Situ Stress and Active Faulting in Oklahoma. *Bulletin of the Seismological Society of America*, 107(1), 216–228. <https://doi.org/10.1785/0120160156>
- Amitrano, D. (2003). Brittle-ductile transition and associated seismicity: Experimental and numerical studies and relationship with the b value. *Journal of Geophysical Research: Solid Earth*, 108(B1). <https://doi.org/10.1029/2001JB000680>
- ANF (2019). Array Network Facility Monthly Deployment History. Retrieved from http://anf.ucsd.edu/stations/deployment_history.php, accessed February 1st, 2019.
- Angelier, J. (1979). Determination of the mean principal directions of stresses for a given fault population. *Tectonophysics*, 56(3–4), T17–T26. [https://doi.org/10.1016/0040-1951\(79\)90081-7](https://doi.org/10.1016/0040-1951(79)90081-7)
- Astiz, L., Eakins, J. A., Martynov, V. G., Cox, T. A., Tytell, J., Reyes, J. C., et al. (2014). The Array Network Facility Seismic Bulletin: Products and an Unbiased View of United States Seismicity. *Seismological Research Letters*, 85(3), 576–593. <https://doi.org/10.1785/0220130141>
- Atkinson, G. M., & Boore, D. M. (2006). Earthquake Ground-Motion Prediction Equations for Eastern North America. *Bulletin of the Seismological Society of America*, 96(6), 2181–2205. <https://doi.org/10.1785/0120050245>
- Baars, D. (1995). Basement tectonic configuration in Kansas. *Kansas Geological Survey Bulletin*, (237).
- Bachmann, C. E., Wiemer, S., Goertz-Allmann, B. P., & Woessner, J. (2012). Influence of pore-pressure on the event-size distribution of induced earthquakes: PORE PRESSURE AND EQ SIZE DISTRIBUTION. *Geophysical Research Letters*, 39(9), n/a-n/a. <https://doi.org/10.1029/2012GL051480>
- Barwick, J. S. (1928) The Salina basin of north-central Kansas: *Am. Assoc. Petroleum Geologists Bull.*, v. 12, p. 177-199, fig. 1-5.
- Boyd, O. S., McNamara, D. E., Hartzell, S., & Choy, G. (2017). Influence of Lithostatic Stress on Earthquake Stress Drops in North America. *Bulletin of the Seismological Society of America*, 107(2), 856–868. <https://doi.org/10.1785/0120160219>
- Brune, J. N. (1970). Tectonic stress and the spectra of seismic shear waves from earthquakes. *Journal of Geophysical Research*, 75(26), 4997–5009.
- Busby, R., Woodward, R., Hafner, K., Vernon, F., and Frassetto, A. (2018). The Design and Implementation of EarthScope’s USArray Transportable Array in the Conterminous United States and Southern Canada. Technical report, Earth Scope.
- Choy, G. L., Rubinstein, J. L., Yeck, W. L., McNamara, D. E., Mueller, C. S., & Boyd, O. S. (2016). A Rare Moderate-Sized (Mw 4.9) Earthquake in Kansas: Rupture Process of the Milan, Kansas, Earthquake of 12 November 2014 and Its Relationship to Fluid Injection. *Seismological Research Letters*, 87(6), 1433–1441. <https://doi.org/10.1785/0220160100>
- Clerc, F., Harrington, R. M., Liu, Y., & Gu, Y. J. (2016). Stress drop estimates and hypocenter relocations of induced seismicity near Crooked Lake, Alberta: Stress Drop of the CLS. *Geophysical Research Letters*, 43(13), 6942–6951. <https://doi.org/10.1002/2016GL069800>
- Cole, V. B., 1975, Subsurface Ordovician-Cambrian rocks in Kansas: Kansas Geological Survey, Subsurface Geology Series 2, 18 p.

- Dart, R. L. (1990). In situ stress analysis of wellbore breakouts from Oklahoma and the Texas Panhandle. Department of the Interior, US Geological Survey.
- Davis, S. D., Nyffenegger, P. A., & Frohlich, C. (1995). The 9 April 1993 earthquake in south-central Texas. *Bulletin of the Seismological Society of America*, 85(6), 1888–1895.
- Davis, Scott D., & Frohlich, C. (1993). Did (Or Will) Fluid Injection Cause Earthquakes? - Criteria for a Rational Assessment. *Seismological Research Letters*, 64(3–4), 207–224.
<https://doi.org/10.1785/gssrl.64.3-4.207>
- Dubois, S. M., & Wilson, F. W. (1978). A Revised and Augmented List of Earthquake Intensities for Kansas, 1867-1977. Kansas Geological Survey, Environmental Geology Series 2.
- Ellsworth, W. L. (2013). Injection-Induced Earthquakes. *Science*, 341, 1225942.
<https://doi.org/10.1126/science.1225942>
- Eshelby, J. D. (1957). The determination of the elastic field of an ellipsoidal inclusion, and related problems. *Proceedings of the Royal Society of London. Series A. Mathematical and Physical Sciences*, 241(1226), 376–396.
- Evans, D. M. (1966). The Denver area earthquakes and the Rocky Mountain Arsenal disposal well. *Mountain Geologist*, 1, 23–36.
- Franseen, E.K., Byrnes, A.P., Cansler, J.R., Steinhauft, D.M., and Carr, T.R., 2004, The geology of Kansas, Arbuckle Group: Kansas Geological Survey, Current Research in Earth Sciences, Bulletin, no. 250, pt. 2.
- Frohlich, C. (2012). Two-year survey comparing earthquake activity and injection-well locations in the Barnett Shale, Texas. *Proceedings of the National Academy of Sciences*, 109(35), 13934–13938.
<https://doi.org/10.1073/pnas.1207728109>
- Frohlich, Cliff. (2012). A survey of earthquakes and injection well locations in the Barnett Shale, Texas. *The Leading Edge*, 31(12), 1446–1451. <https://doi.org/10.1190/tle31121446.1>
- Gephart, J. W., & Forsyth, D. W. (1984). An improved method for determining the regional stress tensor using earthquake focal mechanism data: Application to the San Fernando Earthquake Sequence. *Journal of Geophysical Research*, 89(B11), 9305. <https://doi.org/10.1029/JB089iB11p09305>
- Gerhard, L.C., (2004). A New Look at an Old Petroleum Province. *Kansas Geological Survey Bulletin* 250.
- Goertz-Allmann, B. P., Goertz, A., & Wiemer, S. (2011). Stress drop variations of induced earthquakes at the Basel geothermal site: STRESS DROP OF INDUCED EARTHQUAKES IN BASEL. *Geophysical Research Letters*, 38(9), n/a-n/a. <https://doi.org/10.1029/2011GL047498>
- Gutenberg, B., & Richter, C. F. (1956). Earthquake magnitude, intensity, energy, and acceleration: (Second paper). *Bulletin of the Seismological Society of America*, 46(2), 105–145.
- Hanks, T. C., & Kanamori, H. (1979). A moment magnitude scale. *Journal of Geophysical Research*, 84(B5), 2348. <https://doi.org/10.1029/JB084iB05p02348>
- Hardebeck, J. L. & Shearer, P.M. (2002). A New Method for Determining First-Motion Focal Mechanisms. *Bulletin of the Seismological Society of America*, 92(6), 2264–2276.
<https://doi.org/10.1785/0120010200>
- Hardebeck, J. L. & Shearer, P.M. (2003). Using S/P Amplitude Ratios to Constrain the Focal Mechanisms of Small Earthquakes. *Bulletin of the Seismological Society of America*, 93(6), 2434–2444.
<https://doi.org/10.1785/0120020236>
- Havskov, J., & Ottemoller, L. (2010). *Routine Data Processing in Earthquake Seismology*. Dordrecht: Springer Netherlands. <https://doi.org/10.1007/978-90-481-8697-6>
- Havskov, J., Alguacil, G. (2016). *Instrumentation in Earthquake Seismology*. Springer.
- Healy, J. H., Rubey, W. W., Griggs, D. T., & Raleigh, C. B. (1968). The Denver Earthquakes. *Science*, 161, 1301. <https://doi.org/10.1126/science.161.3848.1301>

- Hildebrand, G. M., Steeples, D. W., Knapp, R. W., Miller, R. D., & Bennett, B. C. (1988). Microearthquakes in Kansas and Nebraska 1977–87. *Seismological Research Letters*, 59(4), 159–163. <https://doi.org/10.1785/gssrl.59.4.159>
- Horton, S. (2012). Disposal of Hydrofracking Waste Fluid by Injection into Subsurface Aquifers Triggers Earthquake Swarm in Central Arkansas with Potential for Damaging Earthquake. *Seismological Research Letters*, 83(2), 250–260. <https://doi.org/10.1785/gssrl.83.2.250>
- Hough, S. E. (1997). Empirical Green's function analysis: Taking the next step. *Journal of Geophysical Research: Solid Earth*, 102(B3), 5369–5384. <https://doi.org/10.1029/96JB03488>
- Hough, S. E. (2014). Shaking from Injection-Induced Earthquakes in the Central and Eastern United States. *Bulletin of the Seismological Society of America*, 104(5), 2619–2626. <https://doi.org/10.1785/0120140099>
- Hubbert, K. M., & Rubey, W. W. (1959). ROLE OF FLUID PRESSURE IN MECHANICS OF OVERTHRUST FAULTING. *Geological Society of America Bulletin*, 70(2), 115. [https://doi.org/10.1130/0016-7606\(1959\)70\[115:ROFPIM\]2.0.CO;2](https://doi.org/10.1130/0016-7606(1959)70[115:ROFPIM]2.0.CO;2)
- Jewett, J. M. (1951). *Geologic Structures in Kansas*, Bulletin 90, Part 6. Lawrence, Kansas: Kansas Geological Survey.
- IRIS-DMC (2019). Incorporated Research Institutions for Seismology Data Management Center. Retrieved from <http://ds.iris.edu/gmap/>, Accessed March 28th, 2019
- Kanamori, H., & Anderson, D. L. (1975). Theoretical basis of some empirical relations in seismology. *Bulletin of the Seismological Society of America*, 65(5), 1073–1095.
- Kanamori, H. (1977). The energy release in great earthquakes. *Journal of Geophysical Research*, 82(20), 2981–2987. <https://doi.org/10.1029/JB082i020p02981>
- Kaneko, Y., & Shearer, P. M. (2015). Variability of seismic source spectra, estimated stress drop, and radiated energy, derived from cohesive-zone models of symmetrical and asymmetrical circular and elliptical ruptures. *Journal of Geophysical Research: Solid Earth*, 120(2), 1053–1079. <https://doi.org/10.1002/2014JB011642>
- Kansas Geological Survey, 2018a, Oil and gas wells database: <http://www.kgs.ku.edu/Magellan/Qualified/index.html>
- Keranen, K. M., Weingarten, M., Abers, G. A., Bekins, B. A., & Ge, S. (2014). Sharp increase in central Oklahoma seismicity since 2008 induced by massive wastewater injection. *Science*, 345(6195), 448–451. <https://doi.org/10.1126/science.1255802>
- Keranen, Katie M., Savage, H. M., Abers, G. A., & Cochran, E. S. (2013). Potentially induced earthquakes in Oklahoma, USA: Links between wastewater injection and the 2011 Mw 5.7 earthquake sequence. *Geology*, 41(6), 699–702. <https://doi.org/10.1130/G34045.1>
- Kim, W.-Y. (2013). Induced seismicity associated with fluid injection into a deep well in Youngstown, Ohio: INDUCED SEISMICITY IN YOUNGSTOWN, OHIO. *Journal of Geophysical Research: Solid Earth*, 118(7), 3506–3518. <https://doi.org/10.1002/jgrb.50247>
- Kisslinger, C. (1980). Evaluation of S to P amplitude ratios for determining focal mechanisms from regional network observations. *Bulletin of the Seismological Society of America*, 70(4), 999–1014.
- Koester, E. A. (1935). *Geology of Central Kansas Uplift*. AAPG Bulletin 19, no. 10. <https://doi.org/10.1306/3D932D70-16B1-11D7-8645000102C1865D>
- Langenbruch, C., & Zoback, M. D. (2016). How will induced seismicity in Oklahoma respond to decreased saltwater injection rates? *Science Advances*, 2(11), e1601542–e1601542. <https://doi.org/10.1126/sciadv.1601542>
- Lee, W. (1956). *Stratigraphy and Structural Development of the Salina Basin Area*. Kansas Geological Survey Bulletin 121.
- Madariaga, R. (1976). Dynamic of an expanding circular fault. *Bull. Seismol. Soc. Am.*, 66, 163–182.

- McBee, W. (2003). Nemaha Strike-Slip Fault Zone. AAPG Mid-Continent Section Meeting, 13 October 2003.
- Merriam, D. F. (1956). History of earthquakes in Kansas. *Bulletin of the Seismological Society of America*, 46(2), 87–96.
- Merriam, D. F. (1963). *The geologic history of Kansas*. University of Kansas Publications.
- Merriam, D. F., and Smith, P., 1961, Preliminary regional structural contour map on top of Arbuckle rocks (Cambrian-Ordovician) in Kansas: Kansas Geological Survey, Oil and Gas Investigations 25.
- Michael, Andrew J. (1984). Determination of stress from slip data: Faults and folds. *Journal of Geophysical Research: Solid Earth*, 89(B13), 11517–11526.
<https://doi.org/10.1029/JB089iB13p11517>
- Michael, Andrew Jay. (1987). Use of focal mechanisms to determine stress: a control study. *Journal of Geophysical Research: Solid Earth*, 92(B1), 357–368.
- NEIC (2019). National Earthquake Information Center. Retrieved from <http://earthquake.usgs.gov/>, Accessed January 4th, 2019.
- Nelson, Ph. H., Gianoutsos, N. J., & Drake II, R. M. (2015). Underpressure in Mesozoic and Paleozoic rock units in the Midcontinent of the United States. *AAPG Bulletin*, 99(10), 1861–1892.
<https://doi.org/10.1306/04171514169>
- Nicholson, C., & Wesson, R. L. (1990). Earthquake hazard associated with deep well injection. A Report to the U.S. Environmental Protection Agency, Bulletin 1951.
- Nolte, K. A., Tsoflias, G. P., Bidgoli, T. S., & Watney, W. L. (2017). Shear-wave anisotropy reveals pore fluid pressure–induced seismicity in the U.S. midcontinent. *Science Advances*, 3(12), e1700443.
<https://doi.org/10.1126/sciadv.1700443>
- Ocola, L. C., & Meyer, R. P. (1973). Central North American Rift System: 1. Structure of the axial zone from seismic and gravimetric data. *Journal of Geophysical Research*, 78(23), 5173–5194.
<https://doi.org/10.1029/JB078i023p05173>
- Ottomoller, L., Voss, P., Havskov, J. (2016). *SeisAn Earthquake Analysis Software for Windows, Solaris, Linux, and MacOSX*.
- Peterie, S. L., Miller, R. D., Intfen, J. W., & Gonzales, J. B. (2018). Earthquakes in Kansas Induced by Extremely Far-Field Pressure Diffusion. *Geophysical Research Letters*, 45(3), 1395–1401.
<https://doi.org/10.1002/2017GL076334>
- Petersen, M. D., Mueller, C. S., Moschetti, M. P., Hoover, S. M., Rukstales, K. S., McNamara, D. E., et al. (2018). 2018 One-Year Seismic Hazard Forecast for the Central and Eastern United States from Induced and Natural Earthquakes. *Seismological Research Letters*, 89(3), 1049–1061.
<https://doi.org/10.1785/0220180005>
- Raleigh, C. B., Healy, J. H., & Bredehoeft, J. D. (1976). An Experiment in Earthquake Control at Rangely, Colorado. *Science*, 191, 1230–1237. <https://doi.org/10.1126/science.191.4233.1230>
- Ramaker, B.J., (2009). Influence of Mississippian Karst Topography on Deposition of the Cherokee Group: Ness County, Kansas. M.S. thesis, University of Kansas, Lawrence, Kansas.
- Reasenber, P. A., and D. Oppenheimer (1985), *Fpfit, fppplot, and fppage: Fortran computer programs for calculating and displaying earthquake fault-plane solutions*, U.S. Geol. Surv. Open File Rep., 85-739.
- Reiter, D., Leidig, M., Yoo, S.-H., & Mayeda, K. (2012). Source characteristics of seismicity associated with underground wastewater disposal: A case study from the 2008 Dallas-Fort Worth earthquake sequence. *The Leading Edge*, 31(12), 1454–1460. <https://doi.org/10.1190/tle31121454.1>
- Richter, C. F. (1935). An instrumental earthquake magnitude scale. *Bulletin of the Seismological Society of America*, 25(1), 1–32.

- Rubinstein, J. L., Ellsworth, W. L., McGarr, A., & Benz, H. M. (2014). The 2001-Present Induced Earthquake Sequence in the Raton Basin of Northern New Mexico and Southern Colorado. *Bulletin of the Seismological Society of America*, 104(5), 2162–2181. <https://doi.org/10.1785/0120140009>
- Rubinstein, Justin L., Ellsworth, W. L., & Dougherty, S. L. (2018). The 2013–2016 Induced Earthquakes in Harper and Sumner Counties, Southern Kansas. *Bulletin of the Seismological Society of America*, 108(2), 674–689. <https://doi.org/10.1785/0120170209>
- Scholz, C. H., Aviles, C., & Wesnousky, S. G. (1986). Scaling differences between large interplate and intraplate earthquakes. *Bulletin of the Seismological Society of America*, 76(1), 65–70.
- Scholz, C. (1968). The frequency-magnitude relation of microfracturing in rock and its relation to earthquakes. *Bulletin of the Seismological Society of America*, 58(1), 399–415.
- Scholz, C., Molnar, P., & Johnson, T. (1972). Detailed studies of frictional sliding of granite and implications for the earthquake mechanism. *Journal of Geophysical Research*, 77(32), 6392–6406.
- Schorlemmer, D., Wiemer, S., & Wyss, M. (2005). Variations in earthquake-size distribution across different stress regimes. *Nature*, 437(7058), 539–542. <https://doi.org/10.1038/nature04094>
- Schwab, D. R., Bidgoli, T. S., & Taylor, M. H. (2017). Characterizing the Potential for Injection-Induced Fault Reactivation Through Subsurface Structural Mapping and Stress Field Analysis, Wellington Field, Sumner County, Kansas: Injection-Induced Fault Slip, Kansas. *Journal of Geophysical Research: Solid Earth*, 122(12), 10,132–10,154. <https://doi.org/10.1002/2017JB014071>
- Snoke, J. (1984). A program for focal mechanism determination by combined use of polarity and SV-P amplitude ratio data. *Earthquake Notes*, 55, 15.
- Snoke, J. A. (2003). FOCMEC: Focal mechanism determinations. *International Handbook of Earthquake and Engineering Seismology*, 85, 1629–1630.
- Sonley, E., Abercrombie, R. E., & Abercrombie, R. (2006). Effects of methods of attenuation correction on source parameter determination. *Geophysical Monograph-American Geophysical Union*, 170, 91.
- Steeple, D. W., 1976, Preliminary crustal model for northwest Kansas (Abs.): *EOA, Trans. AGU*, v. 57, p. 961.
- Steeple, D. W., Hildebrand, G. M., Bennett, B. C., Miller, R. D., Chung, Y.-J., & Knapp, R. W. (1987). Kansas-Nebraska seismicity studies using the Kansas-Nebraska microearthquake network. *Kansas Geological Survey Open-File Report* 87–35.
- Steeple, D. W., Bennett, B. C., Park, C., Miller, R. D., & Knapp, R. W. (1990). Microearthquakes in Kansas and Nebraska, 1977–89. *Kansas Geological Survey Open-File Report* 90–10.
- Stein, S., & Wysession, M. (2003). An introduction to seismology. *Earthquakes, and Earth*.
- Steinhauff, D.M., Fransee, E.K., Brynes, A.P., Cansler, J.R. (1998). Arbuckle Reservoirs in Central Kansas: Relative Importance of Depositional Facies, Early Diagenesis and Unconformity Karst Processes on Reservoir Properties. *Kansas Geological Survey Open-File Report* 98-55.
- Stover, C. W., & Coffman, J. L. (1993). *Seismicity of the United States, 1568-1989 (revised)* (Report No. 1527). <https://doi.org/10.3133/pp1527>
- Suetsugu, D. (1998). Practice on source mechanism. IISEE Lecture note, Tsukuba, Japan.
- Sumy, D. F., Neighbors, C. J., Cochran, E. S., & Keranen, K. M. (2017). Low stress drops observed for aftershocks of the 2011 M_w 5.7 Prague, Oklahoma, earthquake: Low Stress Drops for Prague Aftershocks. *Journal of Geophysical Research: Solid Earth*, 122(5), 3813–3834. <https://doi.org/10.1002/2016JB013153>
- Sun, X., & Hartzell, S. (2014). Finite-fault slip model of the 2011 M_w 5.6 Prague, Oklahoma earthquake from regional waveforms. *Geophysical Research Letters*, 41(12), 4207–4213. <https://doi.org/10.1002/2014GL060410>
- Walsh, F. R., & Zoback, M. D. (2015). Oklahoma’s recent earthquakes and saltwater disposal. *Science Advances*, 1(5), e1500195–e1500195. <https://doi.org/10.1126/sciadv.1500195>

- Warren, D. H., 1975, Record sections for seismic refraction profile Agate-Concordia, eastern Colorado and western Kansas: U.S. Open-file report 75-380, p. 46.
- Wiemer, S., & Wyss, M. (2000). Minimum magnitude of completeness in earthquake catalogs: Examples from Alaska, the western United States, and Japan. *Bulletin of the Seismological Society of America*, 90(4), 859–869.
- Woessner, J., & Wiemer, S. (2005). Assessing the quality of earthquake catalogues: Estimating the magnitude of completeness and its uncertainty. *Bulletin of the Seismological Society of America*, 95(2), 684–698.
- Wu, Q., Chapman, M., & Chen, X. (2018). Stress-Drop Variations of Induced Earthquakes in Oklahoma. *Bulletin of the Seismological Society of America*, 108(3A), 1107–1123.
<https://doi.org/10.1785/0120170335>
- Wyss, M. (1973). Towards a Physical Understanding of the Earthquake Frequency Distribution. *Geophysical Journal International*, 31(4), 341–359. <https://doi.org/10.1111/j.1365-246X.1973.tb06506.x>
- Xia, J., Miller, R. D., Steeples, D. W., and Adkins-Heljeson, D. (1995a) M-41E Residual Bouguer Gravity Map of Kansas, the Second-order Regional Trend Removed, scale 1:1,000,000.
- Xia, J., Miller, R. D., Steeples, D. W., and Adkins-Heljeson, D. (1995b) M-41F Residual Aeromagnetic Map of Kansas, the Second-order Regional Trend Removed, by, scale 1:1,000,000.
- Yarger, H. L. 1983. Regional Interpretation of Kansas Aeromagnetic Data. Kansas Geological Survey, Geophysics Series 1.
- Zhang, H., Eaton, D. W., Li, G., Liu, Y., & Harrington, R. M. (2016). Discriminating induced seismicity from natural earthquakes using moment tensors and source spectra. *Journal of Geophysical Research: Solid Earth*, 121(2), 972–993. <https://doi.org/10.1002/2015JB012603>
- Zoback, M. L., & Zoback, M. (1980). State of stress in the conterminous United States. *Journal of Geophysical Research: Solid Earth*, 85(B11), 6113–6156. <https://doi.org/10.1029/JB085iB11p06113>
- Zoback, M. L., & Zoback, M. D. (1989). Tectonic stress field of the continental United States. *Geophysical Framework of the Continental United States: Geological Society of America Memoir*, 172, 523–539.

Appendix A: Catalog of Earthquakes - Earthscope Transportable Array Data

Origin Time (UTC)	Latitude	Longitude	M_c	M_l
7/9/2010 16:48	38.826	-98.899	1.8	1.8
7/12/2010 6:42	39.076	-99.336	2.0	1.4
7/16/2010 8:15	39.626	-98.838	1.9	-
8/16/2010 1:56	40.061	-99.271	2.5	2.2
9/10/2010 8:37	39.866	-100.02	2.8	2.5
9/19/2010 23:08	39.141	-99.207	2.5	-
9/22/2010 9:20	38.934	-99.193	1.3	-
11/18/2010 13:22	39.122	-99.61	2.5	1.8
11/20/2010 13:25	38.832	-98.667	2.2	-
12/23/2010 3:08	38.974	-99.336	2.5	2.2
12/31/2010 12:05	39.134	-99.607	2.6	2.3
1/2/2011 8:57	39.134	-99.736	2.4	-
1/2/2011 9:15	39.132	-99.718	2.1	-
1/5/2011 8:19	38.942	-99.364	2.5	2.3
1/5/2011 14:06	39.842	-99.461	2.3	2.1
1/14/2011 12:59	39.289	-96.402	2.5	2.2
1/28/2011 13:18	39.093	-98.465	2.3	1.9
2/16/2011 21:56	39.338	-99.321	1.5	-
2/26/2011 17:11	39.157	-99.731	2.1	1.9
3/11/2011 1:27	39.139	-99.718	2.2	-
3/18/2011 18:51	39.314	-99.458	1.5	-

Appendix B: Catalog of Earthquakes – Focal Mechanisms Data

Origin Time (UTC)	Latitude	Longitude	M_l	Strike	Dip	Rake	Method
9/15/2016 3:55	38.68841	-97.497	2.8	19.66	74.24	-37.25	FOCMEC
11/16/2016 17:58	39.68029	-98.597	3.9	2.78	73.73	53.31	FOCMEC
12/4/2016 8:54	39.65219	-98.5481	3.3	6.33	33.23	-24.15	FOCMEC
12/5/2016 10:22	39.62785	-98.5281	2.8	88.00	68.00	116.00	FPFIT
1/25/2017 4:39	38.03223	-98.0056	2.4	351.70	37.30	-169.10	PINV
1/25/2017 5:51	38.01862	-98.0184	2.4	238.92	62.97	-37.45	FOCMEC
1/26/2017 21:09	38.02743	-97.9741	2.5	247.66	72.61	42.19	FOCMEC
1/26/2017 23:49	38.02264	-98.0014	2.3	83.00	48.00	-42.00	FPFIT
1/27/2017 12:33	38.02893	-97.986	2.2	171.10	54.10	-175.80	PINV
1/29/2017 3:33	38.02687	-97.9852	2.4	72.00	48.00	-42.00	FPFIT
1/31/2017 11:08	38.01791	-97.989	3.0	28.90	59.80	-152.40	HASH
2/17/2017 6:16	38.84468	-97.3929	2.3	336.01	71.25	-23.86	FOCMEC
2/18/2017 8:19	38.64372	-97.5688	2.1	269.10	50.00	-32.50	HASH
3/7/2017 3:12	38.6716	-97.5141	2.7	14.40	32.60	-144.90	HASH
4/4/2017 17:54	39.7225	-98.1519	3.7	9.57	50.18	-4.18	FOCMEC
4/5/2017 10:36	39.8004	-98.2099	3.0	297.00	33.30	-173.50	HASH
4/6/2017 16:01	39.7518	-98.1633	3.3	2.21	31.12	-72.81	FOCMEC
4/7/2017 0:13	39.80494	-98.1718	3.1	90.00	78.00	-167.00	FPFIT
4/7/2017 20:08	39.76637	-98.1701	3.5	15.00	63.00	18.00	FPFIT
4/7/2017 20:16	39.7805	-98.262	2.5	216.70	74.90	-45.50	HASH
4/7/2017 22:03	39.81622	-98.1738	2.5	14.00	75.00	-104.00	FPFIT
4/8/2017 5:15	39.70083	-98.1524	3.3	3.88	85.47	64.92	FOCMEC
4/8/2017 15:49	39.76141	-98.1876	2.8	92.90	60.00	142.40	HASH
4/8/2017 18:49	39.7578	-98.1525	2.7	294.10	42.40	-121.30	HASH
5/21/2017 4:54	39.77372	-98.1832	3.4	4.87	46.92	14.51	FOCMEC
5/21/2017 7:04	39.78082	-98.2277	2.7	207.00	68.10	1.50	PINV
5/21/2017 7:45	39.77676	-98.19	2.5	276.30	78.90	171.40	HASH
5/22/2017 20:48	38.02411	-97.9955	2.4	12.00	48.00	-162.00	FPFIT
5/23/2017 16:17	39.76194	-98.1968	3.1	1.30	55.61	-77.85	FOCMEC
5/24/2017 7:19	39.77565	-98.148	3.0	19.00	88.00	18.00	FPFIT
5/24/2017 9:28	39.69468	-98.1823	3.1	4.42	61.98	-49.48	FOCMEC
5/24/2017 15:04	39.75666	-98.1654	2.8	8.87	51.13	42.55	FOCMEC

Origin Time (UTC)	Latitude	Longitude	Magnitude	Strike	Dip	Rake	Method
5/24/2017 15:57	39.80502	-98.1528	2.8	1.72	71.94	63.61	FOCMEC
5/28/2017 18:45	39.79057	-98.1789	2.8	1.09	67.48	-45.90	FOCMEC
5/29/2017 4:25	39.79641	-98.1907	2.9	48.00	58.00	-165.00	FPFIT
5/30/2017 6:24	39.73425	-98.1867	2.5	21.00	88.00	34.00	FPFIT
5/31/2017 19:04	39.81363	-98.1751	2.6	3.41	57.20	32.73	FOCMEC
6/3/2017 20:29	39.73636	-98.1606	3.3	83.00	45.00	158.00	FPFIT
6/4/2017 19:35	39.79479	-98.1563	2.9	277.00	73.20	-175.60	HASH
6/12/2017 11:18	39.74621	-98.1599	3.9	8.22	84.28	-34.59	FOCMEC
6/12/2017 11:32	39.74369	-98.1547	3.4	7.33	65.10	-84.49	FOCMEC
6/13/2017 9:40	39.7672	-98.1643	4.1	84.20	89.70	-145.60	PINV
6/13/2017 10:05	39.76622	-98.1583	2.9	50.00	58.00	-163.00	FPFIT
6/13/2017 10:24	39.76532	-98.2342	2.4	46.00	63.00	138.00	FPFIT
6/13/2017 17:07	39.7642	-98.1907	3.2	2.67	62.97	-30.68	FOCMEC
6/19/2017 7:02	39.75368	-98.1489	3.2	68.00	48.00	-162.00	FPFIT
6/20/2017 3:26	39.62234	-98.0206	2.5	185.00	85.00	-135.00	HASH
6/27/2017 2:20	38.0326	-97.9914	2.4	243.84	76.00	-43.22	FOCMEC
6/27/2017 2:36	38.03051	-97.9847	2.3	246.79	81.82	-54.59	FOCMEC
7/30/2017 0:16	38.01791	-97.98	2.9	87.00	68.00	-42.00	FPFIT
8/3/2017 13:16	39.62465	-98.499	2.4	143.00	38.00	-45.00	FPFIT
8/4/2017 14:13	39.66571	-97.8696	2.8	276.10	56.50	161.20	HASH
8/15/2017 1:29	39.66106	-98.5359	2.4	123.00	78.00	-180.00	FPFIT
8/15/2017 15:15	38.04222	-97.9916	2.6	191.20	36.60	-155.00	HASH
8/23/2017 7:34	38.00946	-98.003	2.3	78.98	40.26	-5.93	FOCMEC
8/31/2017 17:12	39.66622	-97.9262	2.4	209.10	70.00	-90.00	HASH
8/31/2017 17:21	39.69881	-97.9187	3.0	7.24	83.07	-43.56	FOCMEC
9/29/2017 23:28	39.74943	-98.1723	2.5	125.10	35.00	-157.50	HASH
9/30/2017 0:55	39.75033	-98.1805	2.6	2.12	60.13	84.23	FOCMEC
10/10/2017 10:21	38.66874	-97.4717	2.1	9.00	48.00	-127.00	FPFIT
10/10/2017 20:25	38.67369	-97.497	2.9	35.59	25.46	-78.30	FOCMEC
10/13/2017 12:04	38.65496	-97.5027	2.6	31.70	82.90	-154.70	HASH
10/13/2017 22:11	39.74302	-98.1425	3.0	12.00	77.00	-42.00	FPFIT
10/13/2017 22:19	39.74735	-98.1575	2.5	64.00	68.00	-162.00	FPFIT
10/14/2017 2:13	39.7286	-98.1474	3.0	113.30	68.20	-135.00	HASH
10/14/2017 4:33	39.76966	-98.1305	2.6	272.60	72.00	131.00	HASH
10/14/2017 5:01	39.73782	-98.1801	2.6	18.00	64.00	-102.00	FPFIT
10/16/2017 7:09	39.76355	-98.1496	2.3	8.48	47.85	-39.32	FOCMEC
10/28/2017 22:51	39.65764	-97.9124	2.8	8.00	54.07	-37.45	FOCMEC
12/27/2017 2:55	39.65601	-98.2203	2.3	3.42	35.31	7.10	FOCMEC
2/22/2018 23:43	38.66248	-97.5484	2.1	296.00	82.20	178.20	HASH
3/1/2018 20:27	38.01608	-97.9877	3.3	209.60	89.20	156.50	HASH
3/8/2018 10:48	38.01406	-97.9995	3.6	28.70	89.60	179.80	HASH
3/18/2018 2:17	38.01108	-97.9965	3.3	23.20	54.60	-137.30	HASH

Origin Time (UTC)	Latitude	Longitude	Magnitude	Strike	Dip	Rake	Method
3/29/2018 21:03	38.882	-97.4052	2.6	195.34	80.95	-64.66	FOCMEC
4/3/2018 19:26	38.01604	-97.9918	2.6	56.01	71.25	-23.86	FOCMEC
4/3/2018 21:56	38.02092	-98.0005	2.6	55.00	58.00	-82.00	FPFIT
4/8/2018 23:34	38.01904	-98.0036	2.7	31.70	65.00	-123.10	HASH
4/14/2018 2:46	38.01603	-97.9894	3.4	211.20	73.30	-90.00	FOCMEC
4/14/2018 2:59	38.02148	-97.9926	2.6	22.00	57.00	-102.00	FPFIT
4/17/2018 23:05	38.01285	-98.0058	3.2	17.00	68.00	-168.00	FPFIT
4/18/2018 9:14	38.01891	-97.9918	2.7	29.20	84.20	-162.40	HASH
5/15/2018 1:37	38.87186	-97.3807	2.1	16.00	38.00	47.00	FPFIT
5/23/2018 17:05	38.64669	-97.603	2.3	65.00	68.00	-2.00	FPFIT
5/24/2018 6:50	38.64846	-97.629	2.2	10.70	21.10	-169.50	PINV
6/2/2018 3:43	38.01574	-97.9953	2.9	86.00	85.00	-42.00	FPFIT
6/4/2018 11:17	38.80225	-97.5197	2.5	212.33	65.10	-84.49	FOCMEC
6/5/2018 4:15	38.78802	-97.4752	2.6	20.00	22.00	-122.00	FPFIT
6/17/2018 22:05	38.85138	-97.4873	2.4	2.00	28.00	57.00	FPFIT
7/18/2018 19:28	38.7832	-97.4939	2.4	197.33	65.10	-84.40	FOCMEC
8/4/2018 0:49	38.801	-97.508	2.7	80.00	1.00	146.00	FPFIT
10/21/2018 22:01	38.8	-97.512	2.6	0.00	39.00	-122.00	FPFIT
11/17/2018 21:34	38.747	-97.542	3.0	43.00	68.00	-176.00	FPFIT
11/19/2018 7:44	38.744	-97.548	2.9	49.60	28.90	-57.62	FOCMEC
11/19/2018 9:01	38.732	-97.541	2.8	323.10	33.23	-24.15	FOCMEC

Appendix C: Catalog of Earthquakes – Stress Drop Data

Origin Time (UTC)	Latitude	Longitude	MW	County	Moment	Stress Drop (Mpa)	Cornering Frequency (Hz)	Radius (km)
11/15/2015 16:48	39.6229	-98.6969	2.3	Smith	12.6	3.00	15.10	0.094
3/23/2016 4:35	38.7559	-97.4171	2.5	Saline	12.8	3.49	12.50	0.152
4/4/2016 12:34	38.7471	-97.5586	2.6	Saline	12.9	5.71	12.40	0.126
8/12/2016 13:56	37.2829	-97.6395	2.2	Sumner	12.4	1.04	12.90	0.125
8/12/2016 20:39	37.2863	-97.6323	2.2	Sumner	12.4	0.37	8.41	0.162
9/10/2016 10:08	38.6997	-97.4234	2.2	Saline	12.4	1.46	11.30	0.136
9/15/2016 3:55	38.6884	-97.4970	2.3	Saline	12.6	0.97	9.76	0.149
11/16/2016 17:58	39.6803	-98.5970	3.2	Smith	13.9	3.50	6.34	0.239
11/16/2016 21:45	39.6308	-98.5762	2.7	Smith	13.1	1.08	6.67	0.183
11/26/2016 2:57	37.2413	-97.6785	2.6	Sumner	12.9	0.55	6.41	0.224
12/4/2016 8:54	39.6522	-98.5481	2.6	Smith	12.9	0.55	6.47	0.194
12/5/2016 10:22	39.6279	-98.5281	2.3	Smith	12.5	0.81	0.63	0.148
12/6/2016 2:53	39.6237	-98.5305	2.3	Smith	12.5	0.90	13.20	0.128
12/8/2016 12:35	39.6576	-98.5416	2.3	Smith	12.5	0.59	9.20	0.148
1/25/2017 7:29	38.0263	-97.9896	2.2	Reno	12.4	0.24	7.80	0.200
1/26/2017 21:09	38.0274	-97.9741	2.1	Reno	12.3	0.18	7.13	0.205
1/31/2017 11:08	38.0179	-97.9890	2.9	Reno	13.4	0.23	3.66	0.588
3/7/2017 3:12	38.6716	-97.5141	2.3	Saline	12.5	0.62	9.26	0.156
4/4/2017 17:54	39.7225	-98.1519	3.3	Jewell	14	1.75	4.62	0.314
4/5/2017 10:36	39.8004	-98.2099	2.5	Jewell	12.8	0.80	7.72	0.166
4/6/2017 16:01	39.7518	-98.1633	2.8	Jewell	13.3	1.12	6.20	0.199
4/7/2017 0:13	39.8049	-98.1718	3.0	Jewell	13.6	2.15	5.98	0.207
4/7/2017 20:08	39.7664	-98.1701	3.1	Jewell	13.7	0.30	6.28	0.200
4/7/2017 20:16	39.7805	-98.2620	2.4	Jewell	12.7	3.67	14.40	0.117
4/7/2017 22:03	39.8162	-98.1738	2.3	Jewell	12.6	0.73	9.46	0.176
4/8/2017 5:15	39.7008	-98.1524	2.7	Jewell	13.2	3.99	9.63	0.140
4/8/2017 15:49	39.7614	-98.1876	2.3	Jewell	12.6	0.96	0.92	0.171
4/8/2017 18:49	39.7578	-98.1525	2.4	Jewell	12.7	2.18	12.40	0.121
4/20/2017 0:17	39.7503	-98.1629	2.1	Jewell	12.3	0.40	9.61	0.134
5/21/2017 4:54	39.7737	-98.1832	3.4	Jewell	14.1	1.04	3.55	0.462
5/21/2017 7:04	39.7808	-98.2277	2.3	Jewell	12.6	0.40	7.84	0.174
5/21/2017 7:45	39.7768	-98.1900	2.3	Jewell	12.5	0.92	10.60	0.132
5/23/2017 16:17	39.7619	-98.1968	3.0	Jewell	13.6	0.24	3.00	0.500
5/24/2017 7:19	39.7757	-98.1480	2.7	Jewell	13.2	0.70	5.70	0.267
5/24/2017 9:28	39.6947	-98.1823	2.6	Jewell	13.1	1.74	8.44	0.153
5/24/2017 15:04	39.7567	-98.1654	2.4	Jewell	12.6	1.09	9.90	0.131
5/24/2017 15:57	39.8050	-98.1528	2.4	Jewell	12.7	1.50	9.73	0.146

Origin Time (UTC)	Latitude	Longitude	MW	County	Moment	Stress Drop (Mpa)	Cornering Frequency (Hz)	Radius (km)
5/28/2017 18:45	39.7906	-98.1789	2.5	Jewell	12.9	0.69	7.96	0.187
5/29/2017 4:25	39.7964	-98.1907	2.4	Jewell	12.7	0.96	9.39	0.147
5/31/2017 19:04	39.8136	-98.1751	2.3	Jewell	12.6	2.23	13.80	0.105
6/3/2017 20:29	39.7364	-98.1606	2.8	Jewell	13.3	2.20	7.70	0.177
6/4/2017 19:35	39.7948	-98.1563	2.6	Jewell	13	1.91	9.58	0.166
6/12/2017 11:18	39.7462	-98.1599	3.4	Jewell	14.2	3.14	4.85	0.327
6/12/2017 11:37	39.6892	-98.1750	2.5	Jewell	12.9	1.24	8.76	0.161
6/13/2017 9:40	39.7672	-98.1643	3.5	Jewell	14.3	3.31	4.99	0.359
6/13/2017 10:05	39.7662	-98.1583	2.5	Jewell	12.8	3.77	13.60	0.116
6/13/2017 17:07	39.7642	-98.1907	2.7	Jewell	13.2	2.31	8.20	0.156
6/19/2017 7:02	39.7537	-98.1489	2.7	Jewell	13.1	1.87	7.82	0.182
6/20/2017 3:26	39.6223	-98.0206	2.3	Jewell	12.5	0.72	9.14	0.168
7/30/2017 0:13	38.0349	-97.9743	2.7	Reno	13.2	0.89	6.29	0.210
8/4/2017 14:13	39.6657	-97.8696	2.4	Republic	12.6	2.12	13.00	0.119
8/5/2017 15:52	37.2837	-97.6174	2.4	Sumner	12.6	1.74	11.20	0.147
8/5/2017 20:13	37.2873	-97.6209	3.2	Sumner	13.9	1.82	4.57	0.341
8/6/2017 2:38	37.2809	-97.6137	2.7	Sumner	13.2	2.23	7.95	0.184
8/15/2017 15:15	38.0422	-97.9916	2.4	Reno	12.6	0.76	8.63	0.228
8/20/2017 23:07	37.2697	-97.6212	2.4	Sumner	12.7	2.33	11.30	0.361
8/31/2017 17:21	39.6988	-97.9187	2.5	Republic	12.9	1.49	9.54	0.144
9/16/2017 12:42	37.3395	-97.5831	2.3	Sumner	12.5	0.97	9.93	0.160
9/29/2017 23:28	39.7494	-98.1723	2.3	Jewell	12.4	0.58	9.11	0.152
9/30/2017 0:55	39.7503	-98.1805	2.4	Jewell	12.7	0.68	8.87	0.171
10/10/2017 20:25	38.6737	-97.4970	2.5	Saline	12.8	4.38	11.70	0.185
10/13/2017 12:04	38.6550	-97.5027	2.3	Saline	12.6	1.84	10.40	0.166
10/13/2017 22:11	39.7430	-98.1425	2.7	Jewell	13.1	1.54	8.24	0.176
10/13/2017 22:19	39.7474	-98.1575	2.3	Jewell	12.5	1.04	10.30	0.153
10/14/2017 2:13	39.7286	-98.1474	2.5	Jewell	12.9	0.67	7.09	0.188
10/14/2017 4:33	39.7697	-98.1305	2.5	Jewell	12.8	2.62	12.30	0.335
10/14/2017 5:01	39.7378	-98.1801	2.4	Jewell	12.7	1.70	11.30	0.119
10/28/2017 22:51	39.6576	-97.9124	2.4	Republic	12.7	0.56	7.63	0.171
11/8/2017 3:18	37.2715	-97.6222	2.4	Sumner	12.6	1.73	11.40	0.125
2/16/2018 6:23	39.6469	-98.5683	2.2	Smith	12.4	2.33	14.20	0.099
3/1/2018 20:27	38.0161	-97.9877	2.8	Reno	13.3	0.94	5.78	0.231
3/1/2018 20:30	38.0238	-97.9950	2.2	Reno	12.3	0.21	7.88	0.190
3/2/2018 7:29	38.0181	-97.9963	2.3	Reno	12.5	0.09	9.92	0.158
3/8/2018 10:48	38.0130	-98.0015	3.1	Reno	13.7	1.27	4.60	0.285
3/18/2018 2:17	38.0110	-97.9965	2.7	Reno	13.2	0.83	6.06	0.247
3/27/2018 20:44	39.6392	-98.0182	2.3	Jewell	12.5	2.04	14.10	0.101
3/29/2018 21:03	38.8820	-97.4052	2.3	Saline	12.6	0.74	8.71	0.162

Origin Time (UTC)	Latitude	Longitude	MW	County	Moment	Stress Drop (Mpa)	Cornering Frequency (Hz)	Radius (km)
4/3/2018 19:26	38.0163	-97.9917	2.3	Reno	12.5	1.02	9.33	0.164
4/3/2018 21:56	38.0209	-98.0002	2.1	Reno	12.2	1.55	14.10	0.104
4/14/2018 2:46	38.0162	-97.9889	2.8	Reno	13.3	1.47	6.65	0.221
4/14/2018 2:59	38.0213	-97.9940	2.1	Reno	12.3	0.30	9.04	0.195
4/17/2018 23:05	38.0136	-98.0036	2.7	Reno	13.1	1.32	7.08	0.210
4/18/2018 9:14	38.0189	-97.9918	2.1	Reno	12.3	1.17	12.10	0.126
6/2/2018 3:43	38.0158	-97.9959	2.8	Reno	13.2	0.73	6.63	2.615
6/4/2018 11:17	38.8023	-97.5197	2.1	Saline	12.2	2.53	16.10	0.100
6/5/2018 4:15	38.7880	-97.4752	2.2	Saline	12.4	1.12	10.80	0.139
7/24/2018 12:15	39.6413	-98.5172	2.2	Smith	12.4	0.79	11.00	0.308
7/25/2018 18:16	38.0104	-98.0003	2.1	Reno	12.3	0.24	7.81	0.171

Appendix D: Earthquake S-files

A file containing all phase readings with source parameters (i.e. location, magnitude, etc.) used in this thesis can be found at the following location:

<http://www.kgs.ku.edu/Geophysics/Reports/Intfen/AppendixD.pdf>